Charge-density-waves in quasi-one and quasi-two-dimensional metallic crystal systems

Liam A. Gannon

A thesis submitted in partial fulfilment of the requirements for the degree of *Doctor of Philosophy*

Keble College
University of Oxford

Trinity 2015

Charge-density-waves in quasi-one and quasi-two-dimensional metallic crystal systems

Liam A. Gannon

A thesis submitted in partial fulfilment of the requirements for the degree of *Doctor of Philosophy*

Keble College, University of Oxford, Trinity 2015

Abstract

In this thesis I present experimental measurements on a number of different quasi-one and quasi-two-dimensional metallic crystal systems susceptible to density-wave formation.

I outline the discovery of a density-wave superstructure found via X-ray diffraction measurements in the quasi-two-dimensional $Na_2Ti_2As_2O$ and $Na_2Ti_2Sb_2O$ compounds. $Na_2Ti_2Sb_2O$ and $Na_2Ti_2As_2O$ are members of the Ti-based oxy-pnictides a group of compounds which exhibit complex phase diagrams and share structural similarities with the high temperature superconductors. Temperature-dependent X-ray diffraction measurements confirmed the superstructure in both materials to be concomitant with transitions seen in resistivity and magnetic data. The observation of the superstructure combined with results from other experimental techniques demonstrated the transition to be a charge-density-wave.

I also present results on a series of intercalated charge-density-wave compounds Ni_xZrTe_3 . $Ni_xZrTe_3$was measured using X-ray diffraction and ARPES to investigate the effects of chemical pressure on charge-density-wave formation. The transition temperature for density-wave formation in this series of compounds had been previously shown to vary as a result of Ni-content. X-ray diffraction measurements on the series revealed no changes in the wavevector of the associated superstructure modulation across the series. However ARPES measurements on Ni_xZrTe_3 showed subtle changes in the binding energy of the one-dimensional band associated with the charge-density-wave thought to be a result of the Ni-intercalation. Through a combination of XPS, EDX and ARPES measurements the Ni-content in these crystals was deduced to be much lower than growth parameters suggested.

Finally I describe the construction and testing of a straining device designed specifically for use with X-ray synchrotron type measurements. The straining device was successfully tested at the I16 beamline at the Diamond Light Source and shown to induce dynamic strain in a test sample of $M_2Mo_6Se_6$. Further testing at the ID28 beamline at the ESRF revealed that the strain induced in a $M_2Mo_6Se_6$ was significant and resulted in a change in the lattice dynamics of the material.

Acknowledgements

I would first and foremost like to thank my two supervisors Andrew Boothroyd and Moritz Hoesch for their help and support over the past four years, without their knowledge and expertise this thesis would not have been possible. I would particularly like to thank Moritz for his help with the ARPES and IXS measurements presented in this thesis and Andrew for his help interpreting the X-ray diffraction data.

Thank you also to all the people who have helped me with experiments. Prabhakaran, Roger and Andy for their help with X-ray diffraction measurements and the beamline scientists at I16, I19, ID28 and I05 for their help with getting to grips with the various synchrotron techniques. I would also like to thank Alexander Petrovic for his help and input in the design of the straining device and his help with estimating the stiffness of the device.

Thanks to everyone in the Clarendon lab for making the DPhil experience so enjoyable; the office crew Jordan, Matt, Sam, Danielle and Natasha, everyone on the corridor and the tea gang.

I would like to thank my housemates Dan, Ellie, Dave, Sam and Rebecca who have put up with me for so long and made my time in Oxford a lot of fun and finally I would like to thank my parents and siblings who have no idea what I do or why I do it but are supportive of my endeavors none-the-less.

Contents

Chapter 1

Density-wave theory and observation.

1.1 Introduction

The ability to grow a wide range of crystalline materials has enabled the research of fundamental physical principles in well-defined well-controlled environments. One intriguing avenue of research has been into the effects of reduced dimensionality on an electron gas experiencing an external periodic potential. These effects have been explored through investigations into quasi-one and quasi-two-dimensional metallic crystalline materials.

Over the past 50 years research into quasi-one and quasi-two-dimensional crystals has been advanced by a number of important theoretical predications, progress in crystal growth and advances in experimental techniques.

Amongst the most important theoretical advances in this field were the predictions made by Peierls, Frohlich [1] and Kohn [2]. Peierls asserted that a metallic one-dimensional atomic chain would be susceptible to a periodic-lattice-distortion creating a modulation in the electron-density along the chain known as a Density-Wave (DW). Around the same time work performed by Frohlich established the idea of the density-wave being a coherent superposition of electron-hole pairs, as well as outlining the changes in a crysta'ls band-structure due to the formation of a density-wave. Whilst Kohn contributed to the field by outlining the effects a density-wave would have on the lattice dynamics of a one-dimensional system. Importantly this work highlighted the susceptibility of metallic crystals with large electronic anisotropies to a phase where either the charge or spin density is modulated along the crystal lattice.

Experimentally the breakthrough came with the synthesis of inorganic quasi-one and quasi-two-dimensional materials which allowed for well controlled investigations into the physics of electrons in quasi-one and two-dimensional environments.

Experimental research into these materials has revealed much, perhaps most famously with the discovery of high temperature superconductivity in the cuprates [3]. It has also led to the confirmation of theoretically predicted phases such as the spin-density-wave and charge-density-wave states. Much of the current work in this field has focused on the relationship between the density-wave states and the superconductivity observed in these materials [4–6].

The aim of this chapter is to provide a basic theoretical background for the formation of density-waves in metallic crystals and to outline the motivation behind the study of such materials. As such the chapter focuses mainly on introducing the effect of reduced dimensionality on the electrons near the Fermi-surface in crystalline metals, the concept of charge-density-wave formation and the effects of DW formation on the crystal lattice and bandstructure. The chapter also gives an overview of some of the experimental techniques used to observe DW phases, and gives relevant examples of materials in which density-waves have been found.

The behavior of electrons in metallic crystals can be approximated to that of an electron gas interacting with a periodic potential provided by the lattice ions. It is therefore important when beginning to discuss the properties of quasi-one-dimensional metallic crystals to become familiar with the effect of an external potential on a one-dimensional electron gas. An overview of the physics of a one-dimensional electron gas and the effects an arbitrary external potential has on the density of the electron gas is provided at the beginning of this chapter. Results from one-dimensional electron gas theory are then put into the context of a periodic potential such as that seen in crystalline materials and followed with an overview of the typical crystal structures in which density-waves have been observed. A brief discussion of the experimentally observable

features of density-waves phases is also included.

For a full and comprehensive review on charge-density wave formation, the review articles in Refs. [7] and Refs. [8] are recommended.

1.2 The electron gas in one dimension

An electron gas with density $\rho(r)$, when subjected to an external potential $\psi(r)$, will experience a redistribution of its electrons creating a change in the electron density. The distribution of the electrons,

$$\rho(r) = \psi(r)\chi(r), \tag{1.1}$$

is dependent on the external potential and the coupling of this potential to the electron gas, χ(r) [7].

χ(r) is the Lindhard response function and takes the general form,

$$\chi(\mathbf{q}) = \int \frac{d\mathbf{k}}{(2\pi)^d} \frac{f_k - f_{k+q}}{\epsilon_k - \epsilon_{k+q}}, \tag{1.2}$$

where d is the number of dimensions, f_k is the Fermi-Dirac distribution and ϵ is the dispersion relation for the electron gas. Both $\mathbf{k}$ and $\mathbf{q}$ are wave-vectors. This function diverges when the condition

$$\epsilon_k - \mu = \epsilon_{k+q} - \mu, \tag{1.3}$$

is satisfied, where μ is the chemical potential [7].

Due to differences in the dispersion relations of three-dimensional and one-dimensional gases the Lindhard response is drastically different for the one and three-dimensional cases. The changes in the Lindhard function are made clear when it is displayed graphically in Fig.(1.1) at T=0. In the one-dimensional

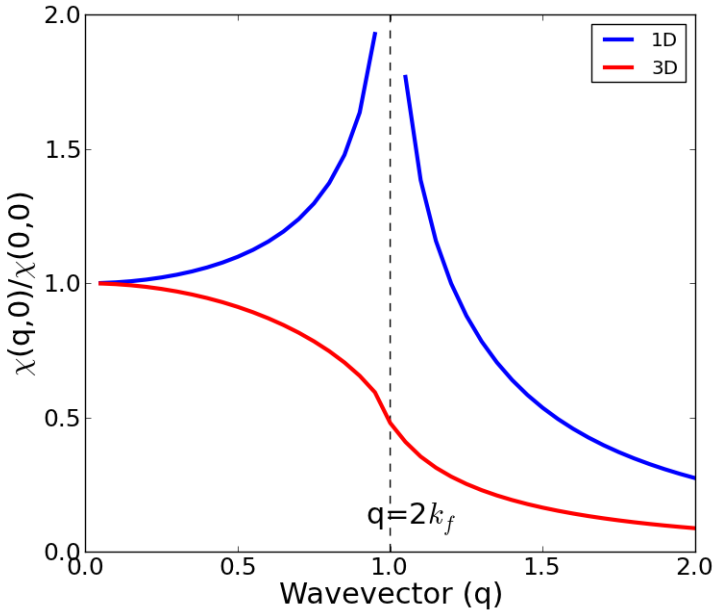

Figure 1.1: The Lindhard response function. The response of a) a one-dimensional electron gas and b) a three-dimensional electron gas .

case it can be seen that the Lindhard function diverges at a wave-vector q=2$\mathbf{k}_f$. For the three-dimensional case the Lindhard response function does not diverge. This can be explained by considering the topology of the respective Fermi-surfaces of the electron gas in one and two-dimensions Fig.(1.2). For a one-dimensional electron gas the Fermi-surface consists of two parallel Fermi-sheets at -$\mathbf{k}_f$ and +$\mathbf{k}_f$. The divergence at q=2$\mathbf{k}_f$ is due to the perfect nesting available to a large number of electron-hole pairs between these Fermi-sheets separated by $\mathbf{q}$, allowing the condition in eq.(1.3) to be satisfied. In higher dimensions fewer states meet this criteria reducing the magnitude of the response.

A divergence in the Lindhard function results in a sinusoidally modulated solution to eq.(1.1) of the type,

$$\rho(r) = \rho_0(1 + \rho_1 cos(2\mathbf{k}_f\mathbf{r} + \alpha)), \tag{1.4}$$

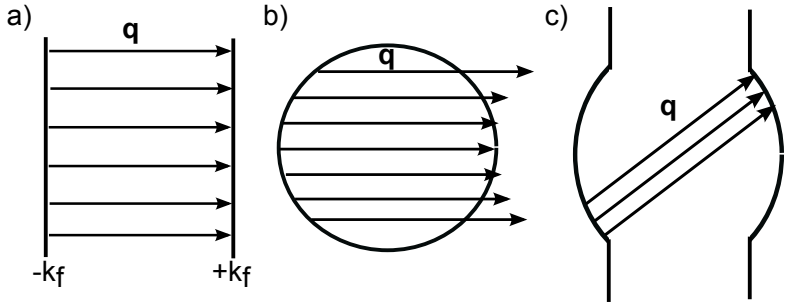

Figure 1.2: Fermi-surface nesting. Nesting with wave-vector **q** for a) a perfect one-dimensional Fermi-surface b) a two-dimensional Fermi-surface and c) a quasi-one-dimensional Fermi-surface. Figure was adapted from [7].

where ρ_0 is the electron density above T_{CDW}, ρ_1 is the magnitude of the density-wave, $2\mathbf{k_f}$ is the wave-vector of the modulation and α describes the phase of the modulation [9].

The periodic modulation of the charge-density of the electron gas is often referred to as a charge-density-wave (CDW). An alternative solution to eq.(1.4) is a modulation of the electron spin rather than the density resulting in the formation of a spin-density-wave (SDW). For the purposes of this discussion I will focus solely on the CDW solution.

In addition to being dependent on **q** the Lindhard response function is, due to the presence of the Fermi function in eq.(1.2), also dependent on temperature. When the nesting condition is satisfied i.e $\mathbf{q}$=$2\mathbf{k}_f$ the temperature dependence takes the form,

$$\chi(2\mathbf{k}_f, T) \propto \ln \frac{1.14\epsilon_0}{k_B T}, \tag{1.5}$$

where ϵ_0 can be approximated to the Fermi-energy and k_B is the Boltzmann constant [7]. This introduces the concept of a transition temperature T_{CDW} for which the value of $\chi(q, T)$ becomes large enough to result in a periodic solution to eq.(1.4).

A one-dimensional electron gas is therefore, in the presence of an external

potential, susceptible to the formation of charge-density-wave as T→0 whereas in higher dimensions the electron-gas is not susceptible to such a modulation due to the shape of the Fermi-surface. In reality, there are no strictly one-dimensional situations, materials are quasi-one-dimensional or quasi-two-dimensional. Quasi-one-dimensional and quasi-two-dimensional are still susceptible to density-wave formation provided that portions of the Fermi-surface have suitable nesting vectors.

1.3 Density-wave formation in a crystal lattice

Using the knowledge of the response of an electron gas to an external periodic potential it is possible to construct a model for the behavior of the conduction electrons in a metallic one-dimensional crystal. The focus in this section is mainly on the consequences of charge-density-wave formation on a perfect one-dimensional crystal lattice, for a full derivation of the model the reader is again pointed to Ref. [7] and Ref. [8].

In a crystal lattice the ionic cores give rise to a periodic potential. The electron wave-functions in this potential take the form of Bloch functions. An important difference between the case described above and a crystal system is the presence of collective lattice vibrations known as phonon modes . These phonon modes lead to a coupled electron-lattice system.

Neglecting el-el interations the electron-lattice system can be described by the Frohlich Hamiltonian, $\mathscr{H}$,

$$\mathscr{H} = \mathscr{H}_{el} + \mathscr{H}_{ph} + \mathscr{H}_{el-ph}, \tag{1.6}$$

where $\mathscr{H}_{el}$ is the Hamiltonian used to describe the electron system, $\mathscr{H}_{ph}$ is the Hamiltonian describing the lattice vibrations and $\mathscr{H}_{el-ph}$ describes the

interaction between the electron and phonon system. The Hamiltonian describing the electron system is given by,

$$\mathscr{H}_{el} = \sum_{\mathbf{k}} \epsilon_{\mathbf{k}} a^{\dagger} a, \tag{1.7}$$

where $\epsilon_{\mathbf{k}}$ is the electron dispersion relation and $a^{\dagger}$ and a are the creation and annhilation operators for the electronic state $\mathbf{k}$ [9]. Similarly $\mathscr{H}_{ph}$ is described by,

$$\mathscr{H}_{ph} = \sum_{\mathbf{q}} \hbar\omega_{\mathbf{q}} b^{\dagger} b, \tag{1.8}$$

a sum over the phonon modes $\mathbf{q}$ described by frequency ω, $b^{\dagger}$ and b are the creation and annihilation operators for the phonon mode with wavevector $\mathbf{q}$ [9]. The final term, $\mathscr{H}_{el-ph}$, describing the coupling between the electron gas and the collective motions of the lattice ions is given by

$$\mathscr{H}_{el-ph} = \sum_{\mathbf{q},\mathbf{k}} g_{\mathbf{q}} a^{\dagger}_{\mathbf{k}+\mathbf{q}} a_{\mathbf{q}} (b^{\dagger}_{-\mathbf{q}} + b_{\mathbf{q}}), \tag{1.9}$$

where $g_{\mathbf{q}}$ is the electron-phonon coupling constant [9].

A displacement of the lattice ions from their equilibrium positions creates a potential, $v_{\mathbf{q}}$, which is experienced by both the lattice and the electron system. In the case of the lattice the displacement, $u_{\mathbf{q}}$ leads to a change in its elastic energy given by,

$$\Delta E_{lattice} = M\omega^2_{\mathbf{q}} u^2_{\mathbf{q}}, \tag{1.10}$$

where M is the mass of the displaced ion [9]. The potential due to the displacement of the lattice ion from its equilibrium position also results in a change in the total energy of the electron system,

$$\Delta E_{el} = -v_{\mathbf{q}}^2 \chi_q. \tag{1.11}$$

The lattice distortion and the associated redistribution of electron density is energetically favourable provided that $\Delta E_{el} + \Delta E_{lattice} < 0$. This expression in addition to a term for the potential, $v_{\mathbf{q}}^2 \propto g_{\mathbf{q^2}}$, leads to the inequality,

$$\frac{4g_{\mathbf{q}}^2}{\hbar\omega_{\mathbf{q}}} > \frac{1}{\chi_{\mathbf{q}}}. \tag{1.12}$$

for the formation of charge-density wave state [9]. If a large proportion of the electronic states satisfy the perfect nesting condition Fig.(1.2) $\chi_{\mathbf{q}}$ will be large and the electron gas will re-order at a transition temperature, T_{CDW} and charge will become modulated along the crystal lattice. In addition a large electron-phonon coupling will also help in satisfying the inequality in eq.(1.12).

1.3.1 Lattice dynamics and Bandstructure

Changes in the electron density due to the formation of a CDW directly affect the vibrational modes of the lattice ions via electron-phonon coupling. The redistribution of charge causes the phonon mode with wave-vector q=$2\mathbf{k}_f$ to become macroscopically occupied. The frequency dependence of this phonon mode, ω_q, is given by

$$\tilde{\omega}_q = \omega_q^2(1 - \frac{4g_q^2}{\hbar\omega_q}\chi(\mathbf{q}, T)) \tag{1.13}$$

where $\tilde{\omega}_q$ is the renormalised frequency of the phonon mode and g_q is the electron-phonon coupling constant [7]. On passing through T_{CDW} the frequency of the phonon mode is reduced to zero at q=$2\mathbf{k}_f$. In higher dimensions, the quasi-one and quasi-two dimensional cases, this effect is reduced. Macro-

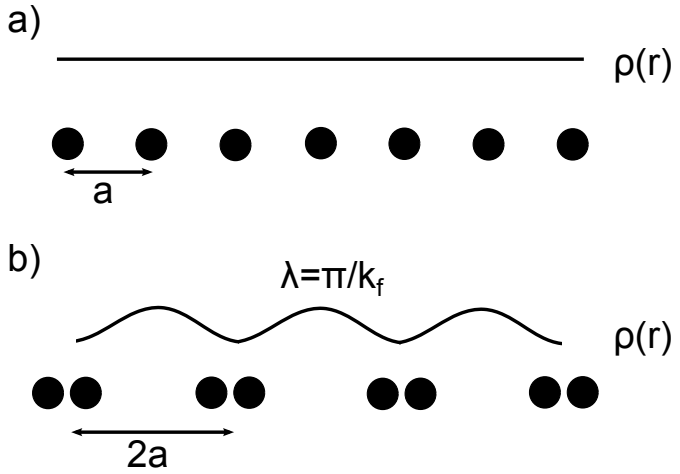

Figure 1.3: The periodic-lattice-distortion. A one-dimensional crystal lattice with lattice constant a and electron density $\rho(r)$ above a) and b) below a charge-density-wave transition. Figure was adapted from [7].

scopic occupation of the phonon mode results in the permanent distortion, a modulation with a period of $\lambda=\frac{2\pi}{2\mathbf{k_f}}$, of the crystal lattice Fig.(1.3) .

An opening of a band-gap at the Fermi energy at $\mathbf{k}_f$ Fig.(1.4), which lowers the electronic energy of the crystal, accompanies the lattice distortion. This is due to the creation of a new Brillouin zone which is formed in response to the new crystal structure described by the lattice distortion. In the case of a perfect one-dimensional metallic crystal this results in a completely gapped Fermi-surface and a metal-to-insulator transition.

Given the two competing energy scales for CDW formation, namely the elastic strain energy of the underlying crystal lattice and the electronic energy of the electron system, it is possible to think of a CDW in terms of two components; the charge ordering and the displacement of the lattice ions from their equilibrium positions. In physical terms the charge modulation can be thought of as redistribution of the electrons in the system across the lattice ions i.e a charge ordering, whilst the displacement of the lattice ions can be described as a strain wave or a locked-in phonon mode.

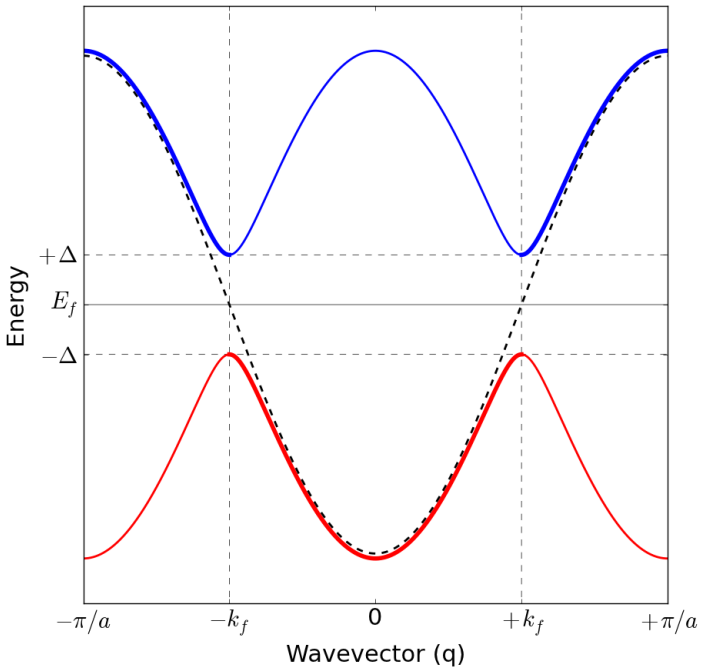

Figure 1.4: The electronic energy-gap. Bandstructue of a half-filled band for a one-dimensional lattice with a lattice constant, a. The dashed line indicates the bandstructure above T_{CDW} whilst the solid red and blue lines show respectively the conduction and valence bands that form below T_{CDW}. The thickness of the conduction and valence band lines indicate the spectral weight of the bands.

1.4 Charge-Density-Wave signatures

The formation of charge-density-waves within crystals leads to a number of experimentally observable effects. Materials with structures which are suspected of being susceptible to CDW formation can be measured using several techniques to confirm the presence of a density-wave. These techniques will be briefly discussed here to provide the reader with a general overview of the experimental field, specific details on the techniques used in this thesis are provided in Chapter.2.

Temperature-dependent resistivity measurements often give the first indication that a material is susceptible to CDW formation. Such measurements are a relatively straightforward method with which to observe the metal-insulator phase transition associated with CDW formation. Similarly the phase transition can also be confirmed by measuring the magnetic susceptibility or heat capacity through the CDW-transition. These measurements are extremely useful in providing accurate values for T_{CDW}, however they do not confirm the transition is due to CDW formation and also cannot distinguish between charge and spin-density waves. Confirming the presence of a DW requires the observation of the periodic-lattice-distortion, observation of the energy-gap associated with the creation of a new Brillouin-zone or direct observation of the charge modulation.

Diffraction techniques using a variety of probes (neutrons, electrons and X-rays) can be used to directly observe the CDW superstructure by coupling directly to the CDW or to the associated lattice-distortion. Through analysis of the diffraction patterns below T_{CDW} these probes allow the determination of the nesting vector q=$2\mathbf{k}_f$ of the density-wave. Since these techniques allow large regions of reciprocal space to be quickly mapped out they are useful

in initially determining $\mathbf{k}_f$. However the CDW superstructure can in many cases be difficult to observe as it is often very weak compared to the main lattice points often requiring the use of high-intensity sources. Resonant X-ray scattering techniques enable direct observation of the charge modulation by directly coupling to the CDW.

Similarly scanning-tunneling-microscopy (STM) can be used to reveal CDW transitions and also the nesting vector. STM has the additional advantage of simultaneously measuring the energy-gap associated with CDW formation.

Angle resolved photoemission spectroscopy (ARPES) and optical spectroscopy have also been used to measure the the CDW energy gap. Observation of the energy gap via ARPES enables several other characteristics of the DW to be determined. In addition to the determination and temperature dependence of the energy gap, ARPES can identify the specific bands involved in the Fermi-surface nesting and link these to atomic bonds in the crystal structure. Band-backfolding below T_{CDW} at the newly formed Brillouin zone boundaries can also be observed in APRES measurements.

Other techniques such as Raman scattering and Inelastic X-ray Scattering (IXS) can provide useful information on the lattice dynamics involved in the CDW formation. IXS has been used to measure the temperature-dependent phonon mode at q=$2\mathbf{k}_f$ eq.(1.13) responsible for the static lattice distortion. This technique does however require prior knowledge of the nesting wave-vector.

Raman scattering has been used to measure changes in the phonon spectrum due to the formation of CDW. Raman scattering is limited to probing modes about the Γ-point and is therefore restricted in its ability to observe the static lattice distortion. Raman scattering can still provide evidence for CDW formation due to the backfolding of additional phonon modes on to the

Γ-point.

1.5 Crystal structures and CDW formation

Charge-density-waves have been observed in crystals with highly anisotropic electronic behaviors. These anisotropies are a result of the material's crystal structure. This section gives a brief example of some of the materials which have been found to exhibit charge-density-waves, highlighting the crystal structures importance to the CDW phase and offering a brief overview of some of the key experiments used to characterise the density-wave. In addition the materials are broadly categorized into two groups, those with quasi-one-dimensional crystal structures and those with quasi-two-dimensional crystal structures.

1.5.1 Quasi-one-dimensional crystals

The atomic bonds along metallic chain-like structures often offer the closest approximation to a one-dimensional electron gas. However, inter-chain coupling always prevents this from being a truly one-dimensional situation, with the resulting crystal structure being quasi-one-dimensional.

A prime example of quasi-one dimensional materials are the tri-chalcogenides MX_3 where M is (Ti,Zr,Hf,Nb,Ta) and X is (S,Se,Te). These materials all exhibit a layered chain-like structure Fig.(1.5). Common to these materials are the MX_3 metallic prismatic chains extending along their b-axis Fig.(1.5b). These chains pack together to form layers which are weakly bonded to one another via the van der Waals force. This crystal structure produces anisotropies in the resistivity of the tri-chalcogenides. For example in $ZrTe_3$ resistivity ratios of $\rho_a : \rho_b, \rho_c$ (1:1:10) have been reported [10] and in $NbSe_3$ the in-plane conductivity has a ratio of $\frac{\sigma_{ab}}{\sigma_c} = 10$ [11] with the out-of-plane conductivity.

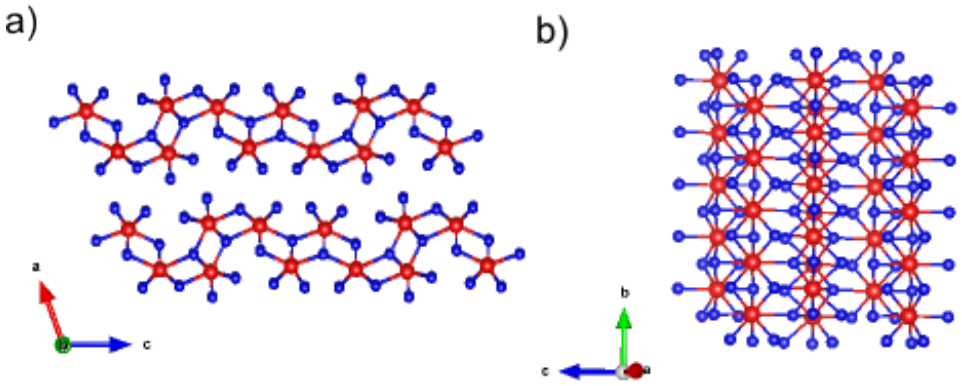

Figure 1.5: Crystal structure of $NbSe_3$. Viewed along a) the chain direction with the prismatic chains of Nb(blue) and Se(red) extending into the page and b) highlighting the prismatic chains. [12]

Diffraction experiments, both electron and X-ray, have been used to reveal the CDW superstructure reflections and the nesting wave-vector in many of the tri-chalogenides [12–14]. $NbSe_3$ demonstrates two DW transitions which are associated with the different chain-types present in the crystal structures [15].

Photoemission has also played an important role in characterizing the tri-chalcogenides. Emission spectra from $NbSe_3$ have revealed band-backfolding associated with CDW formation [16]. One-dimensional Fermi-surface features have been observed in $ZrTe_3$ [17] between which Fermi-surface nesting has been proposed.

Another important and well studied example of quasi-one-dimensional crystals are the molybedenum blue-bronzes, $A_{0.3}MoO_3$ where A=(K or Rb) . These materials have a chain-like structure Fig.(1.6a). Chains of MoO_6 extend along the b-axis and these chains are tessellated in the ac-plane connected along the d-direction by the vector $2\mathbf{d} = (\mathbf{a}+\mathbf{2c})$ Fig.(1.6b) [18]. This structure leads to a highly anisotropic electronic response. Resistivity is smallest along the chain-direction whilst along the d-direction it is an order of magnitude larger. Resistivity is greatest in the direction perpendicular to both the chain

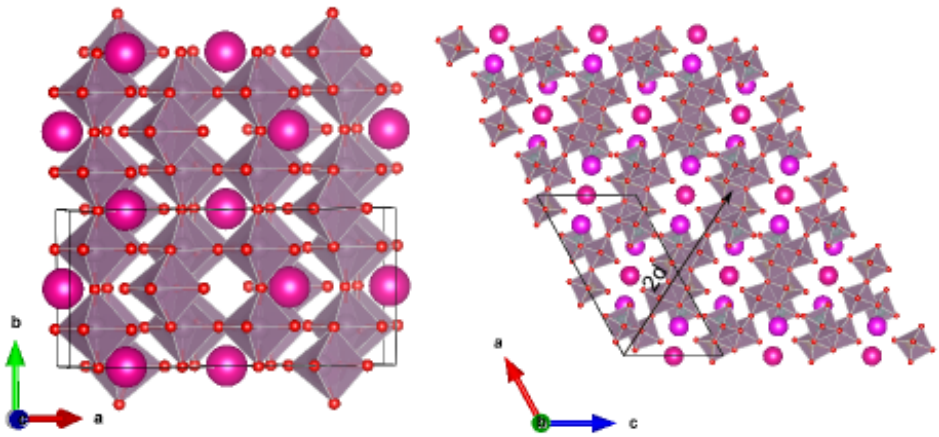

Figure 1.6: Crystal structure of $Rb_{0.3}MoO_3$. a) Viewed perpendicular to the chain direction with the chains composed of MoO_6 octehedra with O(red) surrounding Mo(green) atoms and extending along the b-axis [19] and b) in the ac-plane with the 2**d** vector connecting the chains highlighted and the Rb(pink) atoms separating the chains clearly visible. Figure adapted from [20]

and the **d**-direction, in this direction resistivity is two orders of magnitude greater than along the chains [18].

Resistivity measurements have indicated that the molybdenum bronzes enter a CDW phase below 180K for $K_{0.3}MoO_3$ and 178K for $Rb_{0.3}MoO_3$ [21].

Diffraction type measurements on these materials have revealed that a DW superstructure appear below T_{CDW} with a wave-vector of q_{CDW}=(0, 0.72, 0.5) for $K_{0.3}MoO_3$ and similarly for $Rb_{0.3}MoO_3$ [22]. ARPES studies on $K_{0.3}MoO_3$ have provided evidence for the involvement of quasi-one-dimensional Fermi-surface features in the charge-density-wave transition [20].

These quasi-one dimensional crystals offer a well-defined environment in which to explore the density-wave phase and also its interaction with other phases such as superconductivity. In general the one-dimensional density-wave theory agrees well with experimental observations. Qualitative features of the CDW phase such as the periodic-lattice-distortion, the electronic band-gap, band-backfolding, metal-to-insulator transition and anomalies in heat-capacity

measurements have all been documented in quasi-one-dimensional crystals.

1.5.2 Quasi-two-dimensional crystal structures

The presence of CDWs in layered materials without the additional chain-like structure seen in the metal-trichalcogenides is less common. Layered compounds are quasi-two-dimensional and are thus further removed from the theoretical one-dimensional model. Nesting is often imperfect and the Fermi-surface is only partially gapped in the CDW phase. Density-wave transitions in these materials are in general less likely than in the quasi-one-dimensional case, requiring a strong-electron phonon coupling to overcome the reduction in $\chi(q,T)$ caused by imperfect nesting at the Fermi-surface.

The transition-metal di-chalcogenides are often used as an example of two-dimensional charge-density wave materials. These materials consist of chalcogen-metal-chalcogen layers Fig.(1.7) bound together by weak van der Waals forces.

One extensively studied and interesting example of the di-chacogenides is 1T-TaS_2 . 1T-TaS_2 has a rich phase-diagram, undergoing several charge-density wave transitions Fig.(1.7). In addition to several CDW phases which are driven by electron-phonon interactions 1T-TaS_2 enters a Mott-insulator state which is governed by electron-electron interactions. Under pressure the emergence of superconductivity at 7GPa [5] adds to this complex phase diagram. 1T-TaS_2 offers the opportunity to investigate the competition or cooperation between a number of unique electronic phases. In a wider context 1T-TaS_2 highlights that electronically anisotropic materials which are susceptible to electronic stabilities can be used to study fundamental physical interactions.

Universal to all these materials is the presence of quasi-one-dimensional Fermi sheets at the Fermi-surface, allowing for the nesting condition to be

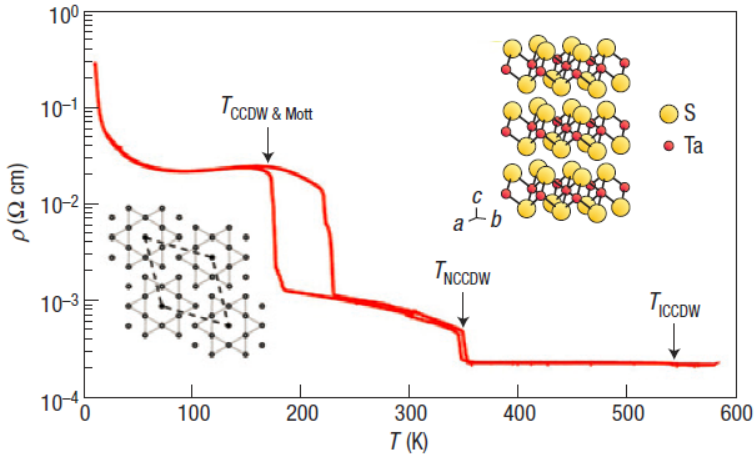

Figure 1.7: Phase diagram of 1T-TaS_2. The high-temperature incommensurate-CDW phase (ICCDW), the nearly-commensurate-CDW phase (NCCDW) and the commensurate-CDW phase are labeled. Above the ICCDW phase 1T-TaS_2 is a metal and with the onset of the CCDW state it behaves as a Mott-insulator. The inset in the upper right shows the layered crystal structure whilst the lower left inset shows the Ta distortions which accompany the CCDW phase transition. Reprinted by permission from Macmillan Publishers Ltd: Nature Materials Ref. [5], copyright 2008 http://www.nature.com/doifinder/10.1038/nmat2318l

satisfied, and also the presence of electron-phonon coupling, which leads to the periodic-lattice-distortion. However these criteria are not always sufficient to lead to the formation of CDW especially in the case of two and quasi-two-dimensional materials. For the formation of a density-wave the primary criteria that must be fulfilled in all dimensions is that it is energetically favorable for the crystal to do so. Whilst in the perfect one-dimensional case the change in energy going from the metallic to charge-density wave can be calculated, quantitative predictions in higher dimensions are less reliable [9].

1.6 Competition and co-existence of CDW and superconductivity

Density-waves and conventional superconductivity have been found to both be present in a number of materials [23–26]. Given that both CDW formation and superconductivity are Fermi-surface driven transitions which rely on electron-phonon coupling this is perhaps unsurprising. Developing an understanding of the interaction between the two phases has been the focus of much research [23, 24]. Superconductivity and CDW have been shown to co-exist in some materials [25]. In a large number of CDW materials suppression of the density-wave state has led to the emergence or enhancement of superconductivity [5, 27]. Suppression of the CDW wave state prevents the gapping of regions of the Fermi-surface and allows these regions to more readily participate in the formation of a superconducting phase.

Methods which can be used to suppress CDW formation can in some cases be used to promote superconductivity such as in the "1/8-doped" cuprate $La_{2-x}Ba_xCuO_4$ (x = 1/8) [28]. Such methods often focus on perturbing the nesting condition of the quasi-one or quasi-two-dimensional electron gas at the

Fermi-surface by changing the shape of the Fermi-surface features i.e increasing their dimensionality.

1.7 Pressure effects on CDW formation

Pressure allows the manipulation of the chemical-bonds in a material by either increasing or decreasing the distance between atoms in the crystal structure. Such changes can have a large influence on the Fermi-surface. Changing the shape of features such as the one-dimensional bands required for Fermi-surface nesting can reduce the number of nested states and suppress the formation of a CDW allowing these regions to play a role in superconductivity.

Hydrostatic pressure has been used on several materials to suppress CDW formation and promote superconductivity [5]. Suppression of the CDW is usually observed in resistivity measurements where T_{CDW} is seen to decrease and T_{SC} increase. X-ray diffraction measurements have demonstrated the effects of pressure directly on the CDW superstructure by observing a change in the nesting vector of the CDW [29].

A popular alternative to hydrostatic pressure is chemical pressure through the intercalation or substitution of chemical species into CDW materials. Chemical pressure has been successful in suppressing the CDW phase in many materials either through the intercalation of atoms between layers or chains or through substitution into the layers or chains of the compound. This is highlighted in Fig.(1.8) which shows the effects of pressure on a quasi-one dimensional material and doping in a quasi-two-dimensional material.

Establishing techniques to apply pressure to CDW crystals is therefore an effective way of investigating the relationship between the density-wave state and the superconducting phase. Observing the changes to the electronic and

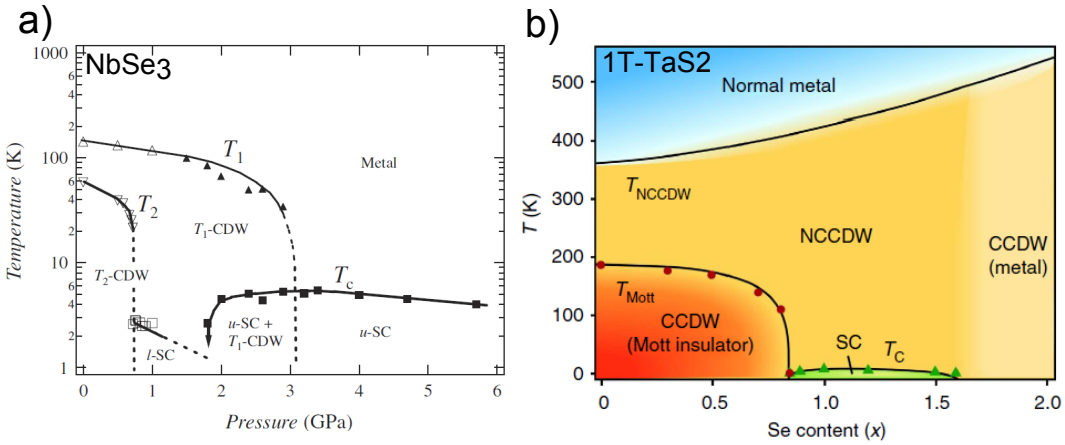

Figure 1.8: Pressure effects in quasi-one-dimensional materials. Phase diagrams of a) $NbSe_3$ (figure reproduced from Ref. [25]. Copyright JPS (2005) The Physical Society of Japan. `http://dx.doi.org/10.1143/JPSJ.74.1782`) and b) doped 1T-$TaS_{1-x}Se_x$. Figure reprinted by permission from Macmillan Publishers Ltd: Nat. Commun Ref. [6], copyright (2015) `http://www.nature.com/doifinder/10.1038/ncomms7091l`

structural properties as pressure is applied provides a way of determining the features important to both the superconducting and CDW states.

1.8 Thesis Overview

This thesis investigates several CDW materials with quasi-one-dimensional or quasi-two-dimensional crystal structures.

Chapter.2 provides a background to the measurement techniques used in later chapters and expands on the key experimentally observable signatures of CDW formation briefly covered in this chapter.

Chapter.3 presents X-ray diffraction and ARPES data from two quasi-two dimensional crystals $Na_2Ti_2As_2O$ and $Na_2Ti_2Sb_2O$. The layered oxy-pnictide family to which $Na_2Ti_2As_2O$ and $Na_2Ti_2Sb_2O$ belong have rich phase diagrams in which different phases compete for dominance. Establishing the type of DW seen in $Na_2Ti_2As_2O$ and $Na_2Ti_2Sb_2O$ forms the focus Chapter 3.

I also present two possible methods for the suppression of the CDW in crystalline materials. Chapter.4 investigates the effect of chemical pressure through Ni-intercalation on the bandstructure and the superstructure modulation vector of the quasi-one-dimensional CDW material $ZrTe_3$. Previous resistivity measurements have indicated that such Ni-intercalation suppresses the CDW in these materials but a detailed bandstructure analysis has yet to be performed.

In Chapter 5 I present the construction and testing of a novel device for the application of uni-axial strain to single crystals for use in X-ray synchrotron experiments. This device whilst widely applicable to many systems is ideal in its design for inducing strain in quasi-one and quasi-two dimensional-systems especially those with interesting electronic anisotropies. In terms of density-wave materials it can be seen as a method for CDW suppression analogous in many ways to hydrostatic pressurization and chemical substitution. However the straining device offers several key advantages over these existing methods most notably in its compatibility with a wide range of experimental techniques.

Finally in Chapter 6 I summarize my findings and make suggestions on future experiments which can lead on from this work.

Chapter 2

Experimental techniques and theory.

2.1 Introduction

For the past 100 years X-rays have been one of the most widely used probes of crystalline materials in condensed matter physics. Discovered in 1895 by Wilhelm Rontgen [30] X-rays are now used in many different techniques to investigate the properties of matter. Such techniques were made possible by a number of crucial pieces of works performed in the first half of the 20^{th} century. First amongst these breakthroughs was the work by Innes [31] using X-rays to investigate the photoelectric effect in various metals, leading to photoemission spectroscopy (PES) in 1957 [32] and later to angle resolved photoemission spectroscopy (ARPES) [33]. It was an observation by Bragg [34] in 1912, that enabled X-ray diffraction to be used to determine the atomic structures of crystalline materials, generating considerable interest in the use of X-rays amongst condensed matter physicists. This breakthrough created the field of X-ray diffraction but also paved the way for many other techniques such as inelastic X-ray scattering and resonant X-ray scattering.

As a result of the wide range of possible techniques that utilise X-ray radiation, the 20^{th} century has seen the rapid development of many different types of X-ray sources. Most notable amongst these X-ray sources are synchrotrons, which produce X-ray radiation through the acceleration of electrons traveling at ultra-relativistic speeds. This type of radiation was first predicted by Iwanenko and I.Pomeranchuk [35] in 1944 and discovered by F.R.Elder [36] in 1947 with the construction of the world's first synchrotron.

The most recent iteration of synchrotrons, the so called 3^{rd} generation synchrotrons, such as the ESRF and the Diamond Light Source operate by confining electrons traveling at close to the speed of light to a specific orbit inside a storage ring. As the electrons travel around the storage ring they encounter

insertion devices designed to oscillate them in such a manner as to produce high brilliance, intense, coherent X-rays that are emitted tangentially to their orbit along specially designed beamlines. These insertion devices known as undulators or wigglers, consist of two banks of magnets separated by a gap through which the orbiting electrons travel. By varying the characteristics of the insertion device, either through shifting the banks of magnets relative to each other or by changing the size of the gap between them, it is possible to change the characteristics of the emitted light.

One of the key concepts in 3^{rd} generation synchrotons is that the insertion devices ensure that the properties of an electron exiting the insertion device are identical to to when it entered. This allows multiple beamlines to operate concurrently off of the same storage ring without being affected by changes made to insertion devices in the other parts on the synchrotron.

Continuing investment into 3^{rd} generation synchrotrons means that these facilities are increasingly accessible to experimentalists. Allowing a huge range of experiments across many scientific disciplines to be performed, including those integral to condensed matter physics. This increase in accessibility means that X-ray based synchrotron techniques play an ever increasing role in our understanding of condensed matter physics.

In the upcoming chapters a number of different X-ray based experimental techniques will be used to measure the physical properties of various crystalline materials. This chapter focuses on the key scientific concepts behind these techniques, the instrumentation used to perform them and also gives an outline of the fundamental physics behind the properties being probed.

2.2 Crystal Lattice Theory

To explain the details of the experimental techniques used in this thesis it is first necessary to define the general structure of crystalline materials under investigation.

A perfect crystal is mathematically constructed by taking a lattice, which is an infinite set of identical points completely described by the lattice vector **R** eq.(2.1), and convolving it with a basis, which in this case is an atom or group of atoms [37]. The lattice vector **R**

$$\mathbf{R} = n_1\mathbf{a} + n_2\mathbf{b} + n_3\mathbf{c} \tag{2.1}$$

is the linear combination of three primitive lattice vectors **a**,**b** and **c** which are a set vectors such that **R** can map any lattice point to any other point on the lattice with n_1,n_2 and n_3 as integers [37].

It is useful when describing crystal structures to define a volume that, when infinitely tessellated, can be used to reconstruct the entire lattice. This volume may be chosen arbitrarily but, a unit cell of the smallest possible volume and containing only one lattice point is known as the primitive unit-cell and a unit cell which includes more than one lattice point is known as a conventional unit-cell [37]. Although these unit cells can be chosen freely the description of a crystal can be greatly simplified by taking into consideration any inherent symmetry of the lattice.

In three-dimensions when a symmetric basis is used there are 14 unique lattices 7 primitive and 7 conventional known as the Bravais lattices. Increasing the complexity of the basis to reflect point, group,screw and glide symmetries one can arrive at the 230 crystallographic space groups. Space groups describe a crystals structure based on the Bravais lattice and the symmetry of its basis

[37]. These definitions of crystal structures enable many problems, such as X-ray diffraction patterns, encountered in crystallography to be reduced in complexity through the knowledge of the appropriate symmetry operations.

2.2.1 Reciprocal space

The periodicity of the crystal lattice in real space, gives rise via Fourier transformation, to another lattice known as the reciprocal lattice in momentum space. This reciprocal lattice with corresponding lattice vector $\mathbf{G}$ and primitive lattice vectors $\mathbf{a}^*$,$\mathbf{b}^*$ and $\mathbf{c}^*$,

$$\mathbf{G} = h\mathbf{a}^* + k\mathbf{b}^* + l\mathbf{c}^* \quad where\, h,k,l = \text{Integer}, \tag{2.2}$$

is useful when describing the wave-like behavior of the properties of the crystal such as atomic vibrations and electron density as well as its interaction with external probes such as neutrons, electrons and X-rays that can be described with a wavevector [38] .

The real space primitive lattice vector and the reciprocal space vectors are related by

$$\mathbf{a}^* = \mathbf{2}\pi\frac{\mathbf{b}\times\mathbf{c}}{\mathbf{a}\cdot(\mathbf{b}\times\mathbf{c})},\ \mathbf{b}^* = \mathbf{2}\pi\frac{\mathbf{a}\times\mathbf{c}}{\mathbf{b}\cdot(\mathbf{a}\times\mathbf{c})},\ \mathbf{c}^* = \mathbf{2}\pi\frac{\mathbf{a}\times\mathbf{b}}{\mathbf{c}\cdot(\mathbf{a}\times\mathbf{b})}. \tag{2.3}$$

A similar concept to that of the real space primitive unit cell known as the Brillouin zone exists for the reciprocal lattice. The 1^{st} Briullioun Zone is defined geometrically as the volume contained within the reciprocal lattice points that can be reached from the origin, known as the Γ-point, without crossing a lattice plane. The concept of the Brillouin zone becomes useful when describing the wave-like properties of a crystal such as lattice vibrations

and electronic bandstructure and will be used later.

2.3 X-ray diffraction

Since its discovery by von Laue, X-ray diffraction has been used in many different scientific disciplines and been responsible for a large number of Nobel Prizes. In the field of condensed matter physics it is one of the principal methods used to determine the structure of crystalline materials.

2.3.1 X-ray Diffraction Theory

X-ray diffraction utilizes the interaction between light and the electron density associated with the atomic basis of a crystal lattice. A lattice by definition is periodic and, in the case of a crystal, this periodicity extends to the properties of its basis. The electron density associated with the atomic basis therefore gives rise to a periodic electron density which extends throughout the crystal lattice.

The scattering rate of light, Γ, with an initial wavevector $\mathbf{k}$ and final waveform $\mathbf{k}'$ from a periodic potential V(r) arising from an electron density $\rho(r)$, is given by Fermi's Golden Rule [39]

$$\Gamma(\mathbf{k}', \mathbf{k}) = \frac{2\pi}{\hbar} \langle \mathbf{k}'|V(r)|\mathbf{k}\rangle^2 \, \delta(E_{k'} - E_k), \tag{2.4}$$

where the delta function provides the condition of elastic scattering $E_{k'} = E_k$ i.e the energy of the incident $E_{\mathbf{k}}$ and scattered $E'_{\mathbf{k}}$ radiation are equal.The matrix element term in Fermi's Golden Rule is given by

$$\langle \mathbf{k}'|V|\mathbf{k}\rangle = \frac{1}{\sqrt{L^3}} \int dr e^{-i((\mathbf{k}'-\mathbf{k})\cdot\mathbf{r})} V(r), \tag{2.5}$$

where the constant L normalizes the wavefunction to the system. The periodic potential $V(r)$ produced by the electron density imposes the condition $\mathbf{k}' - \mathbf{k} = \mathbf{G}$ for constructive interference known as the Laue condition which conserves the crystal momentum during the scattering process. The Laue condition states that for diffraction to occur the difference between the wavevectors of the scattered and incident radiation must be equal to a reciprocal lattice vector [38].

Combining the Laue condition and the geometry of a scattering experiment it is possible to obtain Braggs law for X-ray diffraction

$$2d_{hkl} \sin\theta = n\lambda. \tag{2.6}$$

Bragg's law defines the relationship between the wavelength of the incident light λ, the real space distance d_{hkl} between lattice planes, and the angle between the incident and scattered radiation 2θ.

Bragg's law introduces the important concept of lattice planes which are key to forming an understanding of X-ray crystallography. Lattice planes are defined as planes which extend to infinity through the crystal lattice intersecting at least three non-colinear lattice points. A family of lattice planes is defined as a set of parallel planes containing all of the lattice points separated by a reciprocal lattice vector $\mathbf{G} = 2\pi/d$ or in real space by distance d_{hkl} [38]. Using Bragg's law it is possible to relate the intensities observed in diffraction patterns to specific lattice planes and reconstruct aspects of the geometry of the crystal lattice. However to obtain a full description of the diffraction pattern including the intensity of the scattered light the basis of the lattice must also be taken into consideration.

Returning to Fermi's Golden rule the matrix element eq.(2.5) may be split

into two components a constant contribution arising if the Laue condition is satisfied and the structure factor $S_{\mathbf{G}}$

$$S_{(\mathbf{G})} \propto \sum_j f_j e^{i(\mathbf{G}\cdot\mathbf{x_j})}, \tag{2.7}$$

where f_j is the atomic form factor of the atom j in the unit cell and x_j is the position of the atom in the unit cell [38]. The structure factor describes the contribution to the scattering from each atom within the unit cell. For X-ray scattering, the atomic form factor is proportional to the the electronic charge distribution of the atom j within the unit cell [38]

$$f_j(\mathbf{G}) \propto \int d\mathbf{r}\rho_j(r)e^{i(\mathbf{G}\cdot\mathbf{r})}. \tag{2.8}$$

Simple analysis of the lattice structure factor leads to extinction conditions where the intensity of the diffracted light from a specific set of lattice planes goes to zero. Identification of the allowed and forbidden reflections enables diffraction patterns to be interpreted and the space group of the crystalline materials to be resolved.

The intensity I_{hkl} of the light scattered from a crystal plane is proportional to the square of the structure factor [38]. It is possible to use the structure factor to perform refinements on the diffraction patterns of crystalline materials to determine both the space group and the atomic basis of a given crystal.

2.3.2 Experimental Method and Apparatus

For the experiments presented in subsequent chapters three different instruments were used to perform similar X-ray diffraction experiments. I will briefly describe the basics of performing an X-ray diffraction experiment here and go into details of the specific instrumentation in later chapters.

A typical X-ray diffraction experiment is shown in Fig.(2.1). A single crystal is positioned in the path of an incident X-ray beam and the scattered radiation measured using a detector. Samples are typically suspended in a micro-loop using a suitable grease or oil, the micro-loop is then mounted onto a goniometer attached to a diffractometer that provides several circles of rotation for the sample. The sample is positioned into the centre of rotation with respect to the diffractometer and an incident X-ray beam of fixed energy. Lab-based diffraction is usually performed using a Mo or Cu k-alpha source and for synchrotron experiments the energy of the X-ray beam is controlled by an insertion device. Either a large area ccd detector or a point detector is then used to measure the intensity of the diffracted X-rays. Rotating the sample and/or the detector about the centre of rotation provides complete coverage of the diffracted intensities for the lattice planes accessible at the X-ray wavelength being used.

Alternatively an incident X-ray beam with a range of wavelengths can be used and the crystal remains stationary, this technique is generally used to determine the orientation of crystals rather than their structure. The structure of a crystal can also be measured using a powder sample illuminated by a monochromatic X-ray source averaging over all possible crystal orientations.

2.3.3 Diffraction and Charge-Density-Waves

As discussed in Chapter 1 the formation of a charge-density-wave results in a periodic redistribution of charge across the crystal lattice. X-ray diffraction is sensitive to periodicities in charge therefore the formation of a DW gives rise to a new set of reflections in the diffraction pattern referred to as the superlattice reflections or a superstructure [21, 40, 41].

Temperature-dependent diffraction studies of materials with, or suspected

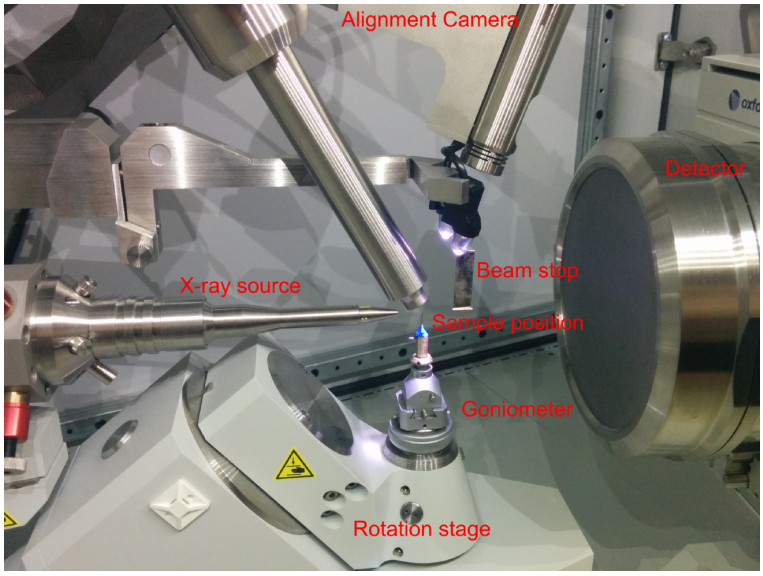

Figure 2.1: Agilent Supernova X-ray diffractometer system. The main features are labeled to highlight the essential components of single crystal X-ray diffraction studies

of undergoing, a charge-density-wave transition are a relatively simple method of extracting both the order parameter for the transition and the Q_{CDW}. However due to the weak intensity of the superlattice reflections it is sometimes necessary to overexpose the main lattice points on the diffracted image to enable the superstructure reflections to become visible.

The higher intensities of incident X-rays available at synchrontrons allow weak superstructures to be easily observed, however as will be demonstrated in later chapters, it is also possible to perform such experiments using laboratory based X-ray sources.

2.4 Electronic bandstructure of crystals

The behavior of electrons within crystalline materials is dictated by the periodic potential they experience from the lattice of ionic cores. The motion of the electrons through the crystal lattice is given by solving the Schrodinger

equation for a particle in a periodic potential; the solution of which results in Bloch's theorem

$$\Psi_{n\mathbf{k}}(r) = e^{i(\mathbf{k}\cdot\mathbf{r})}u_{n\mathbf{k}}(r), \tag{2.9}$$

which states that the eigenstates $\Psi_{n\mathbf{k}}(r)$ of an electron, n, in a periodic potential can be expressed as the product of a plane wave and a function with the periodicity of the crystal lattice $u_{n\mathbf{k}}(r)$ [42]. This expression gives rise to the concept of an electronic bandstructure within crystalline materials where the electrons occupy specific $\mathbf{k}$-states and follow a dispersion curve $E = E(\mathbf{k})$ given by their wavefunction.

Due to the degeneracy of certain bands, specifically at high symmetry points of the crystal, the superposition of the electron wavefunctions results in the creation of energy gaps in the bandstructure. The entire bandstructure of a material can be represented using the reduced-zone scheme where by the bandstructure in higher order Brillioun zones is mapped into the 1^{st} Brilloun zone [43].

Band-filling is dictated by the number electrons in each primitive unit-cell of the crystal lattice and the number of states available. For crystals in which the primitive unit-cell contains an odd number of electrons the highest energy band is half-filled and the Fermi energy in this case is defined as the energy of the highest occupied state. In the case of an even number of electrons in the unit-cell bands are either completely filled or completely empty. This case results in a band gap between filled bands and the first available empty energy state with the Fermi energy lying in-between these two bands. [43].

Electrons within a few meV of the Fermi energy are, in metallic crystals, able to easily access empty momentum-states and are the most influential in

the electronic behavior of crystals. It is therefore highly instructive to be able to map out a surface about the energy, E_f, in momentum space known as the Fermi surface.

Experimental measurement of the bandstructure is possible through a number of different techniques such as quantum oscillations [44],Compton scattering [45] and Angle Resolved Photoemission Spectroscopy (ARPES). These techniques can be used to explore and quantify many electronic phenomena such as superconductivity [46], Dirac points [47] and charge-density-waves [48]. This work is often supported by theoretical predictions on the bandstructure of material made using Density Functional Theory (DFT).

The experimental work presented in later chapters focuses exclusively on ARPES as a means of measuring the bandstructure and Fermi-surfaces of various metals which are known to undergo a charge-density-wave transition. Comprehensive reviews of the technique can be found in [49–51].

2.4.1 Angle Resolved Photoemission Spectroscopy

ARPES is a photon-in electron-out process, which utilises the photoelectric effect eq.(2.10) to measure the binding energy and momentum of electrons within metallic crystals.

A photon of energy, $\hbar\omega$, excites a bound electron with energy, E_b, to a vacuum state with energy, E_{kin}, overcoming the work function, W, of the material

$$E_b = \hbar\omega - E_{kin} - W \tag{2.10}$$

The basic geometry of an ARPES experiment is shown in Fig.(2.2), a sample of known orientation is illuminated by a photon source of known energy

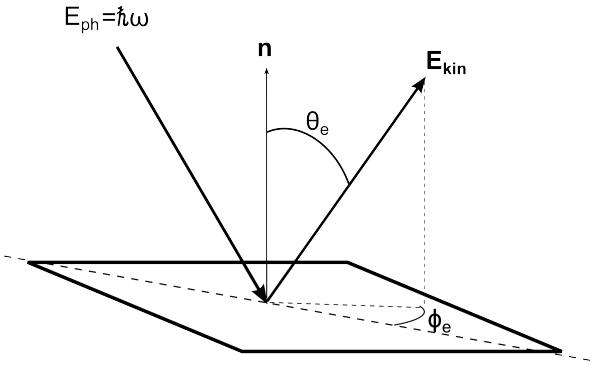

Figure 2.2: Scattering geometry for a typical ARPES experiment

and the angles of emission (Φ_e,Θ_e) and energy of the emitted photoelectron, E_{kin}, are measured.

By measuring the kinetic energy of the emitted electrons E_{kin} and knowing the angle relative to the sample surface normal, θ, of the emitted electrons it is possible through the conservation of energy eq.(2.10) and momentum

$$\mathbf{k}_{kin} - \mathbf{k_b} = \mathbf{k}_{\hbar\omega}, \tag{2.11}$$

to arrive at the binding energy E_b and the parallel momentum

$$\mathbf{k}_{\parallel} = (\frac{2mE_{kin}}{\hbar^2})^{\frac{1}{2}} \sin\theta, \tag{2.12}$$

of the electron in its initial state [49].

However, whilst $\mathbf{k}_{\parallel}$ of the emitted electron is conserved during the emission process $\mathbf{k}_{\perp}$ is not

$$\mathbf{k}_{\perp} = (\frac{2mE_{kin}\cos^2\theta + V_0}{\hbar^2})^{\frac{1}{2}}. \tag{2.13}$$

This is due to the the large change in potential that is experienced by $\mathbf{k}_{\perp}$ electrons going from the sample surface to the vacuum state, which is an analogous to Snell's law for light traveling through a boundary between two

different refractive indices [49].

To account for this, an additional term ,V_0, which is the energy difference between the lowest occupied band and the Fermi-surface must be known. V_0 can be estimated by observing periodicities in the $\mathbf{k}_\perp$ spectra and iteratively adjusting a test value of V_0 such that the period matches known lattice spacings.

In the work presented here only the in-plane momentum of the bound electrons is considered so the derivation of $\mathbf{k}_\perp$ will not be discussed further.

By varying either the angle of the sample with respect to the detector or the energy of the incident photons, and knowing the angle ϕ_e relative to the crystal orientation of the emitted electrons it is possible to map out the electronic bandstructure from which the Fermi surface can be reconstructed.

The photoelectric effect can be described in more detail by breaking it down into a three-step process [49].

A photon interacts with an electron of mass, m, with wavefunction, $\Psi_{initial}$, exciting the electron into a state, Ψ_{Final}, leaving behind a system with (N-1) electrons. Under the approximation that on excitation there is no interaction between the excited electron and the (N-1) electron system, the probability w of transition can be described using Fermi's golden rule.

$$w = \frac{2\pi}{\hbar} |\langle \Psi_f | H_{int} | \Psi_i \rangle|^2 \delta(E_{kin} - E_b - hf), \tag{2.14}$$

where the interaction Hamiltonian H_{int} is given by

$$H_{int} = \frac{e}{mc} \mathbf{A} \cdot \mathbf{p}, \tag{2.15}$$

with $\mathbf{p}$ being the electronic momentum operator and $\mathbf{A}$ the electromagnetic vector potential [49].

The second part of the three-step process calculates the probability of the electron traveling freely through the solid without undergoing a scattering process i.e the electron's mean free path. For electrons with the kinetic energies which are typical in an ARPES experiment (20-120eV) the mean free path is short typically 1-10nm but this is of course material dependent [49]. ARPES is therefore primarily a probe of a sample's surface states and does not probe the bulk of the sample.

If the photoelectron reaches the surface of the material unimpeded, it then has a finite probability to escape to the vacuum states provided its kinetic energy parallel to the surface is greater than the work function of the material.

Combining the probabilities of each these steps gives the overall probability of a bound electron being emitted from a sample due to the interaction with a photon [49].

2.4.2 ARPES Experimental method

ARPES can be performed either using a laboratory based set-up where a helium lamp is used as the light source or using the X-ray light produced by a synchrotron. The data presented in later chapters was taken at the recently commissioned I05 ARPES beamline at the Diamond Light Source. This state-of-the-art beamline provides photons of energies between 18eV and 240eV with an energy resolution of 10meV and angular resolution 0.1^o. The I05 ARPES instrument is shown in Fig.(2.3a).

A typical ARPES experiment to measure the Fermi-surface of a material is described by the following procedure. Prepared samples are inserted into the load-lock which are then transfered to the upper-chamber of the instrument using the transfer arm. Once in the upper chamber the sample is loaded into the sample manipulator where, depending on the sample preparation method,

a fresh surface can be exposed.

Since ARPES is a surface sensitive technique samples require special preparation to ensure that a clean surface can be measured from. There are three popular sample preparation methods: (i) vacuum transfer of epitaxial film, (ii) de-capping of a capped film and (iii) in-situ cleaving of a sample using a top-post. For the ARPES data presented here the top-post method of sample preparation was used Fig.(2.3c). This requires a ceramic top-post to be embedded in a layer of epoxy glue which covers a significant amount of the sample surface. It is is important that the sample is properly grounded to avoid charging from the incident X-ray beam due to the loss of the emitted photoelectrons. Charging is prevented by securing the sample to a conductive sample mount using a silver loaded epoxy allowing the photoemitted current to be replenished.

Once in the upper chamber a wobble stick is used to knock the top-post off the sample, taking with it the epoxy glue and the top layers of the sample exposing a clean surface. Layered materials are often easiest to cleave in this manner and are likely to reveal a surface of known orientation. In the case of materials which exhibit no obvious cleavage plane the orientation of the freshly exposed surface may be more difficult to ascertain.

Sample size is restricted by the top-post technique to a lateral size $1-3$mm and a thickness $0.1-1$mm with smaller samples proving difficult to prepare. Alternative top-post designs such as gluing a wire to needle shaped samples can be used when sample geometries make the routine top-post method awkward. If on removal the top post fails to expose a clean measurement surface the sample is brought back into the load-lock and a new sample selected. The uncertainty of a successful cleave makes it necessary to prepare several samples in the hope that one will provide a suitable surface to measure from.

Both the upper and lower chambers are kept under ultra high vacuum(UHV) (10^{-10}mbar) to prevent the rapid deterioration of the cleaved sample surface due to adsorption and, in the case of the lower chamber where the ARPES measurement takes place, to allow a free path for the photo-emitted electrons from the sample to the detector. Even under UHV condition the sample surface still has a limited lifetime typically less than 24 hours.

From the upper chamber the sample is lowered into the lower chamber where it is aligned such that the soft X-ray beam is incident upon its surface. A Scienta hemispherical analyzer is used to measure the kinetic energy of the emitted electrons. This analyzer consists of two hemispherical electrodes which cause the incident electrons to experience a tunable retardation potential. Allowing the electrons with a specific kinetic energy to be selected out of the photocurrent at angle Θ and enabling the $\mathbf{k}_{\|}$ and E_b of the electrons initial state to be calculated.

The sample stage Fig.(2.3b) offers three translational degrees of freedom x,y and z, the x,y movements are primarily used to find and align a suitable surface and the z movement is used to focus the emitted photoelectrons onto the detector. There are also three rotational degrees of freedom, these are known as the tilt, azimuth and polar angles. Tilt and azimuth both allow for small offsets in sample mounting to be corrected whilst polar changes the θ angle of the electrons detected by the analyzer.

Varying the retardation potential on the analyser and rotating through θ enables the bandstructure and Fermi-surface in the $\mathbf{k}_{\|}$ plane to be mapped out eq.(2.12).

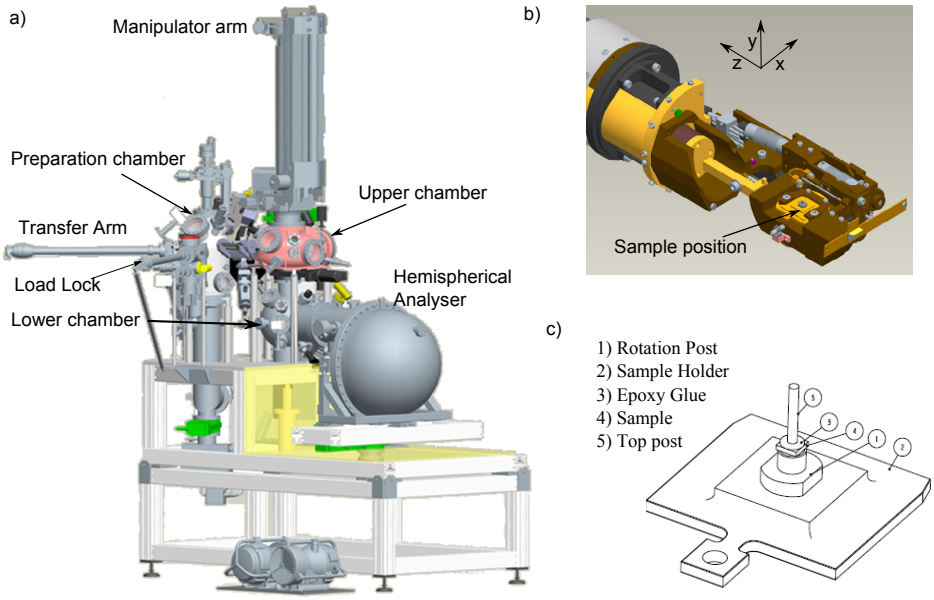

Figure 2.3: ARPES experimental instrumentation. a) The I05 beamline ARPES instrument and b) its manipulator arm showing the degrees of translational motion available with rotation about these three axis also possible. c) A diagram of the sample preparation for a top post cleaving in a typical ARPES experiment. Figure adapted from images provided by M.Hoesch.

2.4.3 ARPES and Charge Density Waves

Materials with parallel one-dimensional Fermi-surface features are often susceptible to electronic instabilities such as density-waves. ARPES measurements enable the identification and characterization of features at the Fermi-surface. Observation of one-dimensional Fermi-surfaces using ARPES can often allow the nesting-vector of a CDW to be deduced.

With the onset of a charge-density-wave the lattice distortion and associated reduction of the Brillioun zone leads to the creation of a gap at the Fermi-surface at $\pm Q_{CDW}$ [48]. Temperature-dependent ARPES measurements can detect the opening of these energy gaps at the Fermi-surface and identify the band associated with density-wave formation.

In addition the band-backfolding due the creation of a new Brillioun zone

can also be imaged using ARPES and provide compelling evidence for the formation of a DW.

2.5 Crystal Lattice Dynamics

X-ray diffraction is used to investigate the average position of the atoms within a crystal lattice, however the deviations of atoms from their equilibrium positions also plays an important role in many areas of condensed matter physics.

Due to inter-atomic forces, these deviations result in collective excitations known as normal modes, whose angular frequency, ω, is related to their wave-vector, $\mathbf{k}$, via a dispersion relation. These modes are traveling waves through the crystal lattice and can be quantized into discrete quanta known as phonons. Phonons are bosonic quasi-particles and as such many can occupy the same quantum state, the number of phonons occupying a particular state is dictated by Bose-Einstein statistics. The number of modes, at each discrete value of $\mathbf{k}$, supported by a 3D lattice with a polyatomic basis is given by $3n$ where n is the number of atoms in the primitive unit-cell [52].

Along high symmetry directions (an idealized case) of the reciprocal lattice, modes can be can be categorized into two different types, longitudinal modes, where the displacement of the atoms is along the direction of mode propagation, and transverse modes where the vibrations are perpendicular to the direction of travel. For crystals with a polyatomic basis the phonon modes split into two distinct branches resulting from the solution of the equation of motion, the acoustic branch and the optical branch. The acoustic branch at low $\mathbf{k}$ values ω is proportional to $\mathbf{k}$ and the atoms in the unit-cell displace coherently. On the other hand the optical branch has a non-zero frequency at $\mathbf{k}$=0 and the atoms in the unit-cell displace out of phase with one-another [52].

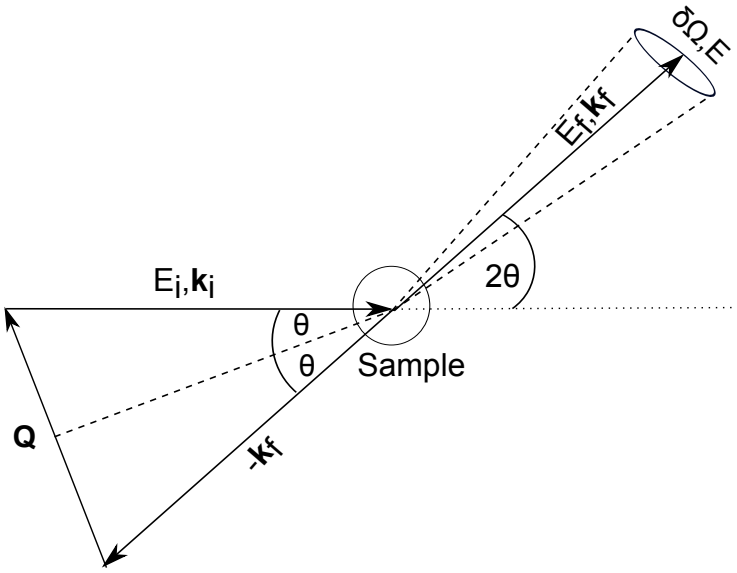

Figure 2.4: Scattering geometry of a typical IXS experiment.

As well as understanding and measuring the phonon spectra of certain materials the work presented here also concerns itself with how the phonons couple to electrons in metallic crystals particularly in certain charge ordered systems, specifically the role they play in the formation of charge density waves. In a later chapter I use inelastic X-ray scattering the details of which are explained below, to measure the phonon modes of a quasi-one dimensional material under uni-axial strain. Comprehensive reviews of the technique can be found within Refs. [53–55].

2.5.1 Inelastic Scattering Theory

The basic principle behind inelastic scattering is illustrated in Fig.(2.4). An incident particle of known energy, E_i, and wavevector, $\mathbf{k}_i$, scatters inelastically from a sample into a final state with wavevector, $\mathbf{k}_f$, and energy, E_f, and in the process of doing so either creates or annihilates a phonon with energy, E_{ph}, and wavevector, $\mathbf{q}_{ph}$. Through conservation of energy and momentum

$$E_{ph} = E_i - E_f \tag{2.16}$$

$$\mathbf{Q} = \mathbf{k_i} - \mathbf{k_f} = \mathbf{G} + \mathbf{q_{ph}} \tag{2.17}$$

it is possible to derive, from the energy and wavevector of the inelastically scattered probe, information about both the wavevector, $\mathbf{q_{ph}}$, and energy, E_{ph}, of the phonon involved in the process [55].

The two probes used for inelastic scattering experiments are neutrons (INS) and X-rays (IXS). The scattering interaction between the two techniques is different. Neutrons interact with the atomic nuclei via the strong force, whilst X-rays interact with the core electrons within a material via their electric fields. In the case of X-rays the electron density is considered to be an accurate approximation of the positions of the atomic nuclei.

Inelastic neutron scattering (INS) is the more established technique with inelastic X-ray scattering only recently being made possible [56]. The difficulty with IXS experiments arises from the high energy resolution required to observe the meV changes associated with phonon creation or annihilation in photons with energies on the keV scale. Recent advances in synchrotron technology mean that X-ray beamlines can now achieve the resolutions required for IXS. This narrow energy resolution is achieved by taking advantage of the relationship between E and k for photons. By minimizing δk it is possible to reduce the uncertainty in E. The uncertainty in δk is minimized by elastically backscattering the X-ray beam from the synchrotron source using a Si monochromator crystal before it is incident on the sample [54].

Neutrons and X-rays each bring their own advantages and disadvantages to inelastic scattering. The main advantages of using X-rays over neutrons is

the smaller sample size requirement. For neutron experiments samples need be of the order of mm^3 due to the limited flux provided by a neutron source, in comparison the high photon fluxes of synchrotron sources enables IXS measurements on samples on the order of μm^3.

Another advantage of using X-rays instead of neutrons, is that for X-rays, the energy of the scattered radiation,

$$E_{\hbar\omega} = hc\mathbf{k}, \tag{2.18}$$

is decoupled from the wavevector, $\mathbf{k}$, making it possible to express the scattering vector, $\mathbf{Q}$, as function of the incident wave-vector and the scattering angle,

$$\mathbf{Q} = 2\hbar\mathbf{k_i}\sin\Theta. \tag{2.19}$$

This relationship is highlighted in the scattering diagram Fig.(2.4), the incident and scattered wavevector in this case of photon scattering are approximately equal. Under this assumption the expression for $\mathbf{Q}$ reduces to eq.(2.19). In contrast to this, for neutrons, energy and wavevector are coupled restricting the possible energy transfers and wavevectors accessible for a given $\mathbf{Q}$. For neutrons the incident and scattered wave-vectors differ significantly, since the energy of the excitation is a significant proportion of the energy of the probe, leading to an expression in neutron scattering

$$E_n = \frac{\hbar^2}{2m}(|\mathbf{k}_{in}|^2 - |\mathbf{k}_{fn}|^2) \tag{2.20}$$

where the change in energy, ΔE_n, of the scattered neutron with mass, m_n, is linked to its initial, $\mathbf{k}_{in}$, and final wavevector, $\mathbf{k}_{fn}$ [37].

A drawback of IXS is the insensitivity of photons to magnetic excitations,

where as INS experiments, due the neutrons weak magnetic moment, are able to probe excitations such as magnons and spin-density-waves. Resonant Inelastic X-ray scattering does allow magnetic excitations to be measured but the achievable resolutions are dependent on the sample composition(>10mev) and are in all cases inferior to the resolutions INS experiments can produce ($\approx$ 1meV).

IXS experiments have only recently been able to achieve energy resolutions on the order of 1.5meV which when compared to INS, where sub meV resolutions are possible, highlights another considerable limitation of IXS.

Despite these fundamental differences, INS and IXS are complementary techniques in that they both probe a property known as the dynamical structure factor S($\mathbf{Q}$,E) and can produce similar phonon spectra for a range of $\mathbf{Q}$ values and phonon energies with IXS providing access to the full dispersion, including at low Q. IXS is therefore a vital probe in the cases where sample size makes INS impossible and where momentum resolution at larger $\mathbf{Q}$ becomes important.

To describe the non-resonant non-magnetic inelastic X-ray scattering process the double differential scattering cross-section, $\frac{\partial^2\sigma}{\partial\Omega\partial E}$, is used

$$\frac{\partial^2\sigma}{\partial\Omega\partial E} = (\frac{\partial\sigma}{\partial\Omega})_{th} S(\mathbf{Q}, E), \tag{2.21}$$

this expression describes the number of particles scattered within an energy ΔE into a solid angle $\Delta\Omega$ [55].

The scattering cross-section is split into two separate components, the contribution due to Thomson scattering [55]

$$(\frac{\partial\sigma}{\partial\Omega})_{th} = r_0^2(\epsilon_i \cdot \epsilon_f)^2 \frac{\mathbf{k}_i}{\mathbf{k}_f}, \tag{2.22}$$

and the dynamical structure factor $S(\mathbf{Q}, E)$ [55]

$$S(\mathbf{Q}, E) = \sum_{F_n, I_n} |\langle F_n| \sum_j e^{i\mathbf{Q}\mathbf{R}_j} |I_n\rangle|^2 \delta(E - E_f - E_i). \tag{2.23}$$

The Thomson scattering eq.(2.22) cross-section defines the interaction between the electromagnetic fields of the incident photons and the electron system being probed, where r_0 is the classical electron radius and ϵ_i and ϵ_f are the polarizations of the incident and scattered light respectively.

S($\mathbf{Q}$,E) in its general form eq.(2.23) describes the properties of an unperturbed many bodied system at position, $\mathbf{R}_j$, in initial state, I_n, and the probability of excitation into a final state, F_n, where the delta function ensures the conservation of energy.

In the more specific case of IXS, where the many bodied system consists of a number of atoms, n, each at position, $\mathbf{R}_n$, the double differential scattering cross-section becomes [55]

$$\frac{\partial^2 \sigma}{\partial \Omega \partial E} = (\frac{\partial \sigma}{\partial \Omega})_{th} |f(Q)|^2 S(\mathbf{Q}, E), \tag{2.24}$$

where $f(Q)$ is the atomic form factor.

Constructive interference occurs between the scattered radiation provided that, the wave-vector difference between the initial and final state, $\hbar\mathbf{Q}$, is much less than the inverse of the coherence length (i.e the inter-atomic distances) [54]. This imposes the condition of using X-rays that have wavelengths of the order of 0.1nm ($\approx 12keV$). Due to the summing and squaring of matrix elements in eq.(2.23) collective excitations within the system can constructively interfere. These collective excitations correspond to phonon modes within the crystalline system.

For a one-phonon scattering event from a single crystal S($\mathbf{Q}$,E) simplifies

to

$$S(\mathbf{Q}, E) = \sum_j (n(E) + \frac{1}{2} \pm \frac{1}{2})(E_j(\mathbf{q}))^{-1} F_{in}(\mathbf{Q}) \delta(E \pm E_j(\mathbf{q})), \tag{2.25}$$

where the population of the phonon states is described by the Bose factor with the $\pm$ term corresponding to the creation or annihilation of a phonon with energy, E_j, and wavevector, $\mathbf{q}$. F_{in} is the inelastic atomic form factor and n(E) is the number of expected excitations or phonons in the system at temperature T. S($\mathbf{Q}$,E) sums over all the possible phonon modes [54].

The temperature dependence of the phonon population implicit in n(E) has important experimental consequences, as the temperature of a sample decreases the population of the phonon mode will decrease. This decrease in population makes it less likely that an inelastic scattering event will destroy a phonon and relatively more likely that the interaction will create a phonon mode. These two different types of interaction where the incident photon either loses energy to the system or gains energy from the system are known respectively as Stokes and Anti-Stokes scattering. Both the Stokes and Anti-Stokes scattered photons are analysed in an IXS spectrum and their relative populations can be used to calibrate the energy spectrum to the central elastic peak.

The inelastic atomic form factor

$$F_{in}(\mathbf{Q}) = |\sum_n (M_n)^{\frac{1}{2}} f_n(Q)[{e_n}^j \cdot \mathbf{Q}] e^{(i\mathbf{Q}\cdot\mathbf{r})} e^{(-w_k)}|^2 \tag{2.26}$$

describes how the individual atoms within the sample scatter the incident light [54]. It includes the atomic form factor and takes into account the possibility of atomic motion in the form of the allowed phonon eigenvectors, e_n^j,

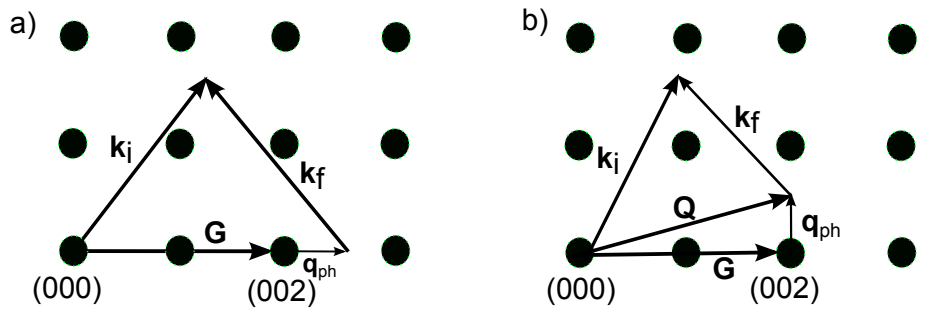

Figure 2.5: IXS reciprocal lattice scattering geometry for the measurement of a) longitudinal phonons and b) for transverse phonon modes. Adapted from Ref. [54]

for each atom with mass, M, in the unit-cell. The Debye-Waller factor, w_k, accounts for the attenuation in the scattered light due to the thermal motion of the atoms.

To access specific phonon modes the initial wavevector and scattering angle must be selected such that the $[e_n^j \cdot \mathbf{Q}]$ term in eq.(2.26) is finite and ideally maximized [53]. In practice it is helpful to talk in terms $\mathbf{q}_{ph}$ and $\mathbf{G}$, where $\mathbf{q}_{ph}$ is the vector to the nearest Bragg point from $\mathbf{Q}$ Fig.(2.5) and $\mathbf{G}$ is the reciprocal wavevector associated with the crystal lattice eq.(2.17).

For longitudinal phonon modes this may mean working in a longitudinal geometry where $\mathbf{Q}$ and $\mathbf{q}_{ph}$ are parallel Fig.(2.5a) and for transverse phonon modes in transverse geometry where $\mathbf{G}$ is perpendicular to $\mathbf{q_{ph}}$ Fig.(2.5b)

2.5.2 IXS Experimental method

The Inelastic X-ray Scattering experiments presented here were performed on the ID28 beamline at the European Synchrotron Radiation Facility (ESRF). ID28 utilises a three axis (the monochromoter, the sample and the analyser) spectrometer the basic layout of which is shown in Fig.(2.6).

Photons arriving from the insertion device are monochromated by a thermally controlled monochromator composed of a Si crystal operating in a backscat-

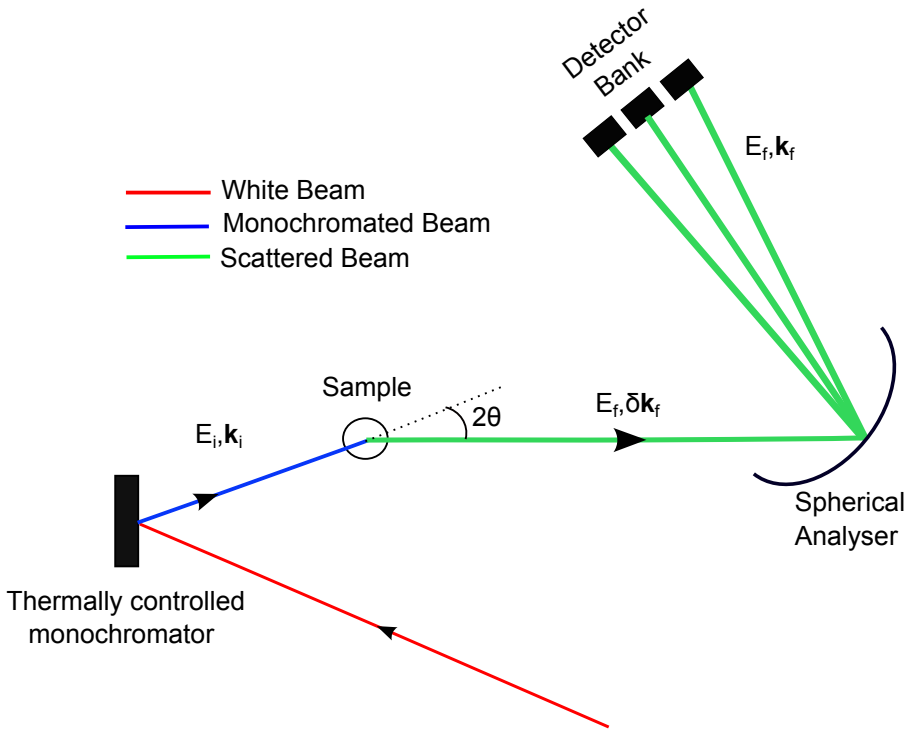

Figure 2.6: IXS back-scattering experimental arrangement. A similar layout is used on the ID28 beamline at the ESRF.

tering geometry. The scattering angle is close to 90^o maximising both the energy and momentum resolutions of the scattered light. Post-monochromator the X-rays are then scattered both elastically and inelastically from the sample. After the scattering event the angular position of a thermally stablised analyzer crystal (Si) defines the momentum transfer, $\mathbf{Q}$, to be measured. High order reflections from the analyser crystal, such as the Si(9 9 9) reflection, are used to maxmise the resolving power of the analyser crystal. The filtered phonons with momentum, $\mathbf{Q}$, and energy , E_f, are detected using a solid state detector or in the case of ID28 a bank of detectors which allow for the simultaneous measurement of several $\mathbf{Q}$ vectors.

An energy scan is performed by fixing a value of $\mathbf{Q}$ and varying E_i via thermal control of the monochromator crystal, altering its diffraction condition through the expansion of its lattice parameters. Changing the lattice parame-

ters whilst keeping θ_M fixed provides a method for varying E_i via Bragg's law. In this manner it is possible to scan across the energy spectrum of the incident photons whilst maintaining a constant $\mathbf{Q}$. When specific phonon modes, with energy, E, and wavevector, $\mathbf{q_{ph}}$, are accessed inelastic scattering will occur and a signal will be registered on the detector. Repeating this process for a number of $\mathbf{Q}$ values allows a phonon spectrum to be obtained.

Samples are aligned using principle lattice reflections, knowledge of these positions allows a UB matrix to be formulated that provides the angular positions required to probe the desired regions of momentum space making it possible to map out phonon dispersions.

2.6 Phonon spectroscopy and CDW

In Chapter 1 the lattice distortion that drives the CDW state was discussed. This distortion can be thought of as a frozen in or static phonon mode known as a Kohn anomaly. As a material approaches the charge-density-wave state the associated ions are fixed into a static distortion which is reflected in the phonon spectrum by a decrease in intensity or softening of the phonon mode at Q_{CDW} which can be directly observed using IXS [57]. Measurements of this type heavily rely on prior knowledge of Q_{CDW} but give direct evidence for strong electron-phonon driven CDW formation.

Chapter 3

Density-wave formation in the layered Ti-based oxy-pnictides.

3.1 Introduction

Since the discovery over two decades ago of high temperature superconductvity (HTS) in the cuprates [3, 58] these materials have been the subject of intensive research. Central to the cuprates are their quasi two-dimensional planer CuO_2 layers Fig.(3.1b) which are thought to be responsible for the unconventional high-temperature superconductivity seen in these layered compounds [59, 60].

Doping of the CuO_2 layer leads to a rich phase diagram [61] covering a number of different phases (antiferromagnetism, density-waves and superconductivity) and has led to much speculation about the origin of the HTS seen in the cuprates. The doping is typically controlled either by changing the number of oxygen vacancies in the CuO chains connecting the CuO_2 layers i.e in $YBa_2Cu_3O_{6+x}$ [41] or, by altering the ratio of the atoms between the CuO_2 layers as is the case in $Nd_{1+x}Ba_{2-x}Cu_3O_7$ or $La_{2-x}Sr_xCu_3O_4$ [28].

The debate over the nature of the superconductivity [62], the pairing mechanism involved [63], the antiferromagnetic nature of the parent compound and the importance in doped cuprates of the proximity of the superconductivity to a charge-ordered state [64–66] has led to great interest in these materials and others like them.

Similarly, the recently discovered iron-based superconductors [67] have also garnered much interest because of their high superconducting temperatures and also the proximity of the superconducting state to a magnetically ordered phase [68].

Like the cuprates the iron-based superconductors form layered structures with a central plane responsible for the superconductivity. In the iron-based superconductors, this layer consists of planar Fe atoms on a square lattice

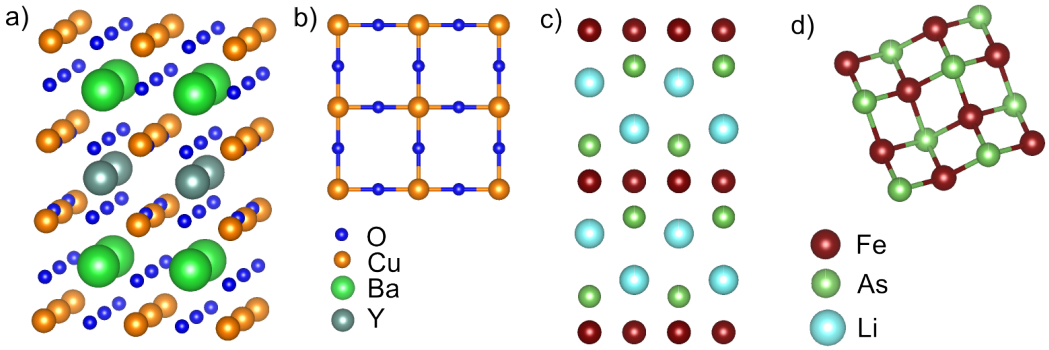

Figure 3.1: Crystal structures of layered high temperature superconductors. Doping via the creation of oxygen vacancies results in the HTS a) $YBa_2Cu_3O_{7-x}$ [70], central to which is b) the Cu-O_2 layer. c) Crystal structure of LiFeAs [71] a member of the recently discovered iron-based superconductors, d) highlights the Fe planer layer common to this family of HTS.

tetrahedrally coordinated with a Pnictide or chalcogoen atoms sitting in the middle of the Fe squares and alternating to be above or below the planer Fe layer Fig.(3.1d).

Chemical substitution into the Fe layer results in either the doping of a the Fe layer or chemical pressure within the parent compound and creates a very similar phase diagram as to that seen in the cuprates [69].

In the pursuit of understanding the rich interesting phase diagrams of both the cuprates and iron-based superconductors structurally analogous materials have been grown.

One recently synthesized group of materials which share structural similarities with both the iron-based superconductors and the cuprates are the Ti-based layered oxy-pnictides $A\mathrm{Ti}_2Pn_2\mathrm{O}$ where A=(Na_2, Ba or $(SrF)_2$) and Pn=(As,Sb or Bi).

The recent discovery of superconductivity in $\mathrm{Ba}_{1-x}\mathrm{Na}_x\mathrm{Ti}_2\mathrm{Sb}_2\mathrm{O}$ and $\mathrm{BaTi}_2\mathrm{Sb}_2\mathrm{O}$ [72, 73], near what is a thought to be a commensurate charge-density-wave transition, has stimulated interest in this family of compounds further.

In this chapter I present results on two compounds, $Na_2Ti_2Sb_2O$ and $Na_2Ti_2As_2O$, which are closely related to $Ba_{1-x}Na_xTi_2Sb_2O$ and have DW transitions at 320K and 115K respectively. The nature of the density-wave in $Na_2Ti_2As_2O$ and $Na_2Ti_2Sb_2O$ has been the source of much debate and, because of the structural similarities with $Ba_{1-x}Na_xTi_2Sb_2O$ and $BaTi_2Sb_2O$ may shed light on the mechanism of the superconductivity in these compounds and have wider implications on the nature of the competition seen between DW states and superconductivity in layered materials.

By performing temperature-dependent X-ray diffraction experiments and combining this data with ARPES and μSR measurements it has been possible to unambiguously show the DW transition in $Na_2Ti_2As_2O$ and $Na_2Ti_2Sb_2O$ to be a charge-density-wave and deduce the associated wave-vectors.

3.2 Ti-Based Layered Pnictide Oxides

The Ti-based layered pnictide oxides are a large family of compounds that exhibit an array of interesting physical properties. This section introduces the ATi_2Pn_2O compounds with a general overview of the properties of these materials and how these can be influenced through doping via a number of different chemical substitutions.

I focus mainly on the two compounds experimentally studied, $Na_2Ti_2As_2O$ and $Na_2Ti_2Sb_2O$, but also discuss the superconducting $BaTi_2Sb_2O$ and $Ba_{1-x}Na_xTi_2Sb_2O$ as a means of highlighting the potential of these materials as a place to study superconductivity in layered materials.

For a more in-depth and comprehensive review of these materials it is recommended that the reader refer to the recently published review article of Ref. [74].

3.2.1 General Crystal Structure

Common to all the Ti-based layered pnictide oxides, $A\mathrm{Ti_2}Pn_2\mathrm{O}$, are square planer Ti-O layers, with Pn (Pn=As, Sb or Bi) anions positioned above and below the centres of the Ti-O squares. This patterning results in Ti octahedra, where Ti ions are each bonded with four adjacent oxygen anions and two pnictide anions. The Pn-Ti-O-Pn type structure is separated by a doping layer made up of A atoms where A =($\mathrm{Na_2}$, Ba or $(SrF)_2$) Fig.(3.2a).

Of particular interest in these materials is the planar Ti-O layer which is the exact anti-structure of the superconducting Cu-$\mathrm{O_2}$ layer Figure.(3.1b) found in the cuprates. The co-ordination of the Ti atoms with neighboring pnictogen ions also draws comparisons to the superconducting layers Fig.(3.1d) found in the iron-based superconductors [74]. It is this Pn-Ti-O-Pn layer which is thought to be responsible for the interesting electronic phases seen in the $A\mathrm{Ti_2}Pn_2\mathrm{O}$ materials [75].

The valence states of the constituent ions in $\mathrm{Na_2Ti_2As_2O}$ and $\mathrm{Na_2Ti_2Sb_2O}$ are oxygen(2^-), pnictogen (3^-), $\mathrm{Na_2}$(2^+) and Ti (3^+) [74]. It is worth drawing attention to the valence state of the titanium which is $3d^1$ and is directly comparable to the $3d^9$ states seen in the $\mathrm{CuO_2}$ planes of the cuprates.

In terms of the structural impact of the choice of A ion, $\mathrm{Na_2Ti_2As_2O}$ and $\mathrm{Na_2Ti_2Sb_2O}$ both contain double layers of Na atoms Fig.(3.2) whereas $\mathrm{BaTi_2Sb_2O}$ and $\mathrm{Ba_{1-x}Na_xTi_2Sb_2O}$ contain a single layer of Ba atoms. This is reflected in the c-axis length of the materials, in $\mathrm{Na_2Ti_2Sb_2O}$ and $\mathrm{Na_2Ti_2As_2O}$ the c-axis is almost double that of $\mathrm{BaTi_2Sb_2O}$ and $\mathrm{Ba_{1-x}Na_xTi_2Sb_2O}$. This double layer results in a different symmetry between the two compounds with P4/mmm for the Ba based materials and I4/mmm for those including Na [74].

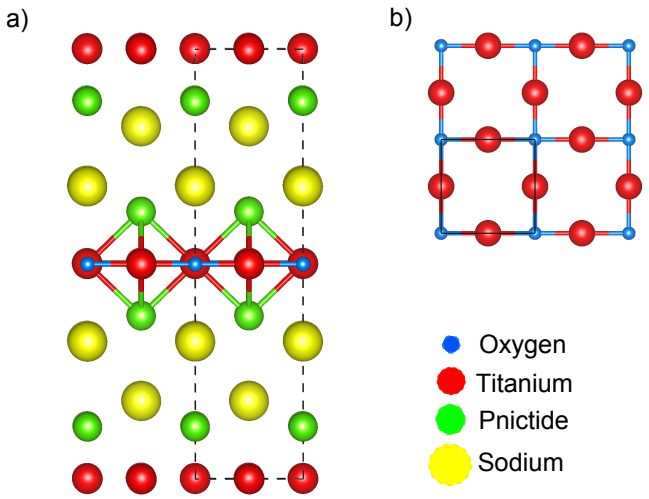

Figure 3.2: Typical crystal structure of $A\mathbf{Ti_2}Pn_2\mathbf{O}$. a) $A\mathrm{Ti_2}Pn_2\mathrm{O}$ is shown viewed along the b-axis where it can be seen that the Ti atoms form octehedra with the Pn and O ions and that the Pn-Ti-O-Pn layers b) are separated by layers of A atoms.

Changing the pnictogen atom only produces a small difference in the c-axis parameter as would be expected, it does however have important consequences for the electronic properties of the material which are discussed below [74].

Lattice parameters for the two Na based compounds are very similar a=b=4.079 Å c=15.262 Å [76] for $Na_2Ti_2As_2O$ and a=b=4.155Å c=16.582 Å [77] for $Na_2Ti_2Sb_2O$. The lattice parameters for $BaTi_2Sb_2O$ are a=b=4.1196 Å c=8.0951 Å [73] .

3.3 Growth method and appearance

Crystal growth of the $Na_2Ti_2As_2O$ and $Na_2Ti_2Sb_2O$ single crystals used in the experiments presented here was performed by collaborators, Xia Wang and Youguo Shi at the Beijing National Laboratory for Condensed Matter Physics and Institute of Physics using a flux growth method described in Ref. [78].

Visually the two materials $Na_2Ti_2Sb_2O$ and $Na_2Ti_2As_2O$ are very similar

in appearance. These compounds both form plate-like single crystals, a consequence of their crystal layered structure, with the largest of these approximately 5mm x 5mm x 2mm. The single crystals are opaque, brittle, black and shiny. Contact with air or moisture causes them to decompose. Decomposition alters the crystals appearance causing the surface to tarnish and regions of soft gray material to form on the crystals surface. To prevent decomposition crystals were stored in an Argon atmosphere and appropriately protected from the atmosphere when performing measurements.

3.4 Electronic and magnetic properties

Focusing attention firstly on $Na_2Ti_2Sb_2O$ and $Na_2Ti_2As_2O$, the magnetic and electrical properties of these materials have previously been fully characterized. Both $Na_2Ti_2Sb_2O$ and $Na_2Ti_2As_2O$ demonstrate anomalies in their magnetic susceptibility indicative of the formation of an ordered DW state Fig.(3.3a) and Fig.(3.3c), these occur at T_{DW}=115K [79] and T_{DW}=320K [78] respectively. The $Na_2Ti_2As_2O$ transition in the susceptibility is broader than the transition observed in $Na_2Ti_2Sb_2O$ sample.

The transitions seen in the magnetic susceptibility are consistent with resistivity data from $Na_2Ti_2Sb_2O$ and $Na_2Ti_2As_2O$ Fig.(3.3b) and Fig.(3.3d) which show metal-to-insulator transitions (MIT) for $Na_2Ti_2Sb_2O$ at 115K [79] and 320K [78] for $Na_2Ti_2As_2O$. The MIT observed in $Na_2Ti_2Sb_2O$ is sharp and as temperature decreases past T_{DW} the material immediately undergoes an insulator-to-metal transition and retains a metallic state. In contrast to this, the resistivity anomaly in $Na_2Ti_2As_2O$ is broad and the insulating state persists after the transition.

For both $Na_2Ti_2Sb_2O$ and $Na_2Ti_2As_2O$ the resistivity data shows strong

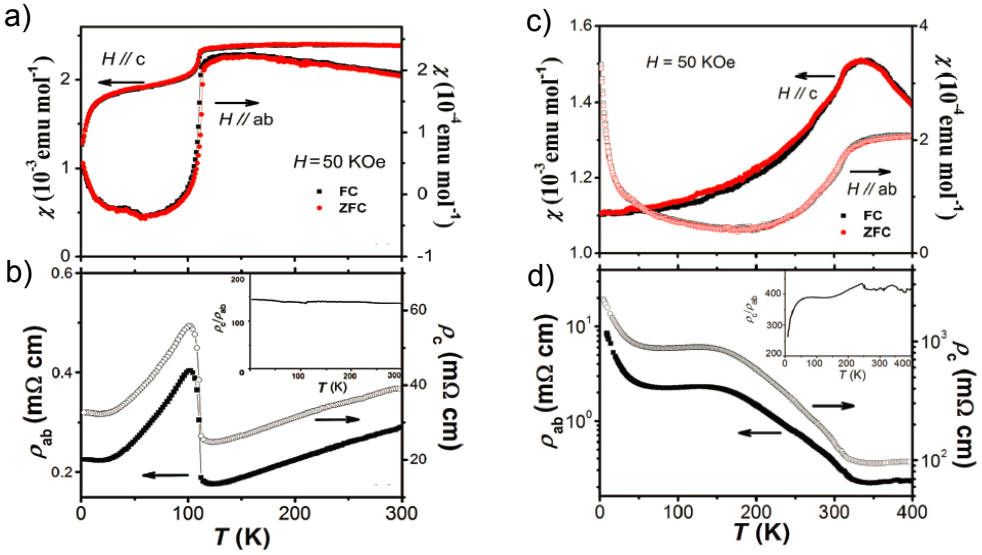

Figure 3.3: Electronic and magnetic properties of $Na_2Ti_2Sb_2O$ and $Na_2Ti_2As_2O$. a) Magnetic susceptibility and b) resistivity data from single crystal $Na_2Ti_2Sb_2O$ with the DW transitions clearly visible at 115K. Magnetic susceptibility and resistivity data for single crystal $Na_2Ti_2As_2O$ are shown in c) and d). Graphs reproduced from the Ref. [78].Reprinted figure with permission from Ref. [78]. Copyright 2013 by the American Physical Society. `http://dx.doi.org/10.1103/PhysRevB.88.144513`

anisotropic behavior. In both materials the in-plane conduction along the ab crystal axis was found to be an order of magnitude greater than the c-axis conduction [78].

A transition similar to that seen in $Na_2Ti_2Sb_2O$ appears in the magnetic susceptibility and resistivity data taken on $BaTi_2Sb_2O$ and $Ba_{1-x}Na_xTi_2Sb_2O$ [73]. However in $BaTi_2Sb_2O$ the transition temperature is lower T_{DW}=54K and can be lowered further to 30K by increasing Na content to x=0.25. Like $Na_2Ti_2Sb_2O$ these compounds remain metallic after the DW transition.

In both $Na_2Ti_2Pn_2O$ and $BaTi_2Pn_2O$ the T_{DW} is dependent on the choice of the pnictogen ion. Increasing the size of the pnictogen ion has been shown to suppress the density-wave i.e decreasing T_{DW} [80]. Suppression of the density wave in this manner is thought to be brought about by changes in the hybridization of the Ti 3d and Pn p orbitals [81, 82] caused by the larger pnictogen ion.

For $Na_2Ti_2Pn_2O$ the DW transition temperatures for the various stable pnictogen atoms are As=320K, Sb=115K [76] and in $BaTi_2Pn_2O$ T_{DW}=200K for As and 54K for Sb [80].

3.4.1 Superconductivity

In the case of $BaTi_2Pn_2O$ in addition to suppressing the T_{DW} the change in the pnictogen from As to Sb has been shown to lead to a superconducting phase with T_{SC}=1.2K [72]. Whilst complete suppression of the density-wave state was achieved in $BaTi_2Bi_2O$ which becomes superconducting at $\approx 4K$.

Hole doping into the Pn-Ti-O-Pn layer via substitution of an appropriate atom into the A layer has resulted in the suppression of the DW state in $Ba_{1-x}Na_xTi_2Sb_2O$. Suppression of the DW state results in an increase in the superconducting transition temperature T_{SC} up to a maximum of 5.4K at

doping levels of x=0.25 [73].

Experimental and theoretical evidence based mainly on the lack of a detectable magnetic signature in the DW state suggests that the superconductivity in these compounds is conventional (electron-phonon coupling) s-wave superconductivity [83, 84]. Although until the DW phase has been fully characterized other mechanisms for the superconductivity can not be ruled out.

3.4.2 Evidence for CDW or SDW

The metal-insulator transitions seen in the $A\mathrm{Ti}_2Pn_2\mathrm{O}$ compounds are thought to be density-wave transitions. The density-wave theory is well supported by bandstructure calculations and in the case of $Na_2Ti_2Sb_2O$ ARPES measurements as well.

Bandstructure calculations of $Na_2Ti_2As_2O$ [85] Fig.(3.4) reveal a relatively simple Fermi-surface consisting of four electron like Fermi sheets which form a square about the X-points, four hole like pockets in a square shape surrounding the M-points and electron like sheets at the Fermi-surface that form a box about the Γ-point. The Fermi-surface in general is dominated by Ti 3d-orbitals and As 4p-orbitals [85].

A similar Fermi-surface for $Na_2Ti_2Sb_2O$ has been predicted and observed using ARPES, with electron-like bands forming a square about the Γ and M-points and hole-like bands forming a box around the X-points [85, 86]. The Fermi-surface is once again dominated by the Ti 3d orbitals but with a more significant contribution to the density-of-states coming from the Sb 4p electrons [85]. ARPES measurements made on $Na_2Ti_2Sb_2O$ agree well with the theoretically predicted bandstructure and also show the opening of an energy gap at the X-point at 113K just below the T_{DW} of 115K [86]. As temperature decreases the size of the gap increases to 65meV at 7K [86].

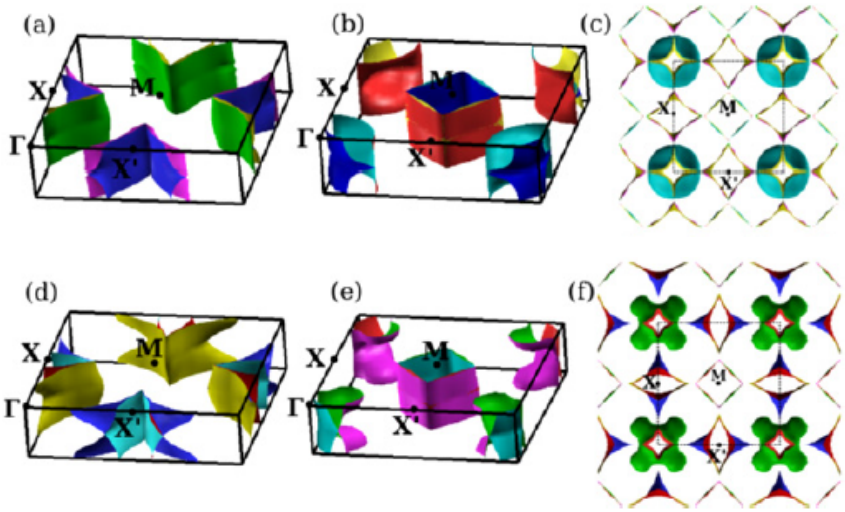

Figure 3.4: $Na_2Ti_2As_2O$ and $Na_2Ti_2Sb_2O$ bandstructure calculations. Theoretical bandstructure predictions for non-magnetic $Na_2Ti_2As_2O$ showing a) the hole-like and b) electron-like bands at the Fermi-surface and c) the complete Fermi surface. Also shown are non-magnetic bandstructure predictions for $Na_2Ti_2Sb_2O$for d)the hole-like and e) the electron-like bands at the Fermi surface and f) the complete Fermi surface. This figure was reproduced from Ref. [85].Copyright IOP Publishing. Reproduced with permission. All rights reserved. `http://iopscience.iop.org/article/10.1088/0953-8984/25/36/365501`

Key to the formation of density-waves are appropriate nesting-vectors between features at the Fermi-surface. A possible nesting-vector has been proposed in $Na_2Ti_2As_2O$ and $Na_2Ti_2Sb_2O$ between the two dimensional sheets surrounding the Γ-point constructed from electron-like-bands and the parallel sheets observed at the X-point due to hole-like-bands [86].

In both cases the Fermi-surface is predicted to demonstrate very little dispersion in the k_z direction for the X and M-point structures, as would be expected in quasi-two-dimenional layered structures, lending itself to the possibility of a significant number of nesting vectors across the Fermi-surface [85].

The nature of the DW in ATi_2Pn_2O has been the centre of much interest, not least because an understanding of the phase may lead to an insight into the mechanism of the superconductivity observed in $Ba_{1-x}Na_xTi_2Sb_2O$ and inform

on the superconductivity observed in the structurally similar iron-pnictides and cuprates.

Whilst the APRES, resistivity and bandstructure calculations provided compelling evidence for a DW in both $Na_2Ti_2As_2O$ and $Na_2Ti_2Sb_2O$ these measurements are unable to conclusively determine between a SDW or CDW. There are conflicting opinions over which is more likely. Bandstructure calculations on $Na_2Ti_2Sb_2O$ taking into account magnetism favour the SDW scenario. However, the lack of a magnetic moment in muon and neutron experiments on these materials hints at a CDW scenario, but does not confirm it as the magnetic moment could be smaller than that detectable resolution achievable by these means. Also the agreement of the ARPES data on $Na_2Ti_2Sb_2O$ with non-magnetic band structure calculations provides evidence for the non-magnetically ordered CDW scenario rather than a SDW.

Electron diffraction and powder X-ray diffraction experiments on $BaTi_2As_2O$ and $BaTi_2Sb_2O$ [87, 88] have failed to reveal the superstructure associated with the formation of a CDW and in general across the whole series of ATi_2Pn_2O compounds no such superstructure has been reported. In the superconducting $Ba_{1-x}Na_xTi_2Sb_2O$ the mechanism behind the anomalies observed in resistivity, magnetic suspectibility and heat capacity is debated.

One argument suggests that the transition is most likely to be a CDW which is supported by NMR [89] and μSR [84] measurements, however it has also been suggested that the transition can be explained by intra-unit-cell charge nematic electronic symmetry breaking [87] which is supported by observation of a lowering of the symmetry from P4/mmm to Pmmm on going through the phase transition.

3.5 X-ray Diffraction Measurements

3.5.1 X-ray Synchrotron Diffraction

To establish the nature of the DW transition seen in $Na_2Ti_2Sb_2O$ and $Na_2Ti_2As_2O$ an exploratory temperature-dependent X-ray diffraction experiment was performed at the I19 beamline at the Diamond Light Source. The aim of the experiment was to observe or conclusively rule-out superstructure modulations associated with CDW formation.

Diffraction using a synchrotron source and specifically the I19 beamline has considerable advantages over other scattering techniques such as resonant X-ray scattering or lab-based X-ray diffraction. Firstly, the large area detector at the I19 beamline provided the ability to quickly take images over large sections of reciprocal space building up a full sphere of collection in around 30 minutes. The ability to cover large areas of reciprocal space quickly is particular advantageous when $\mathbf{q}_{CDW}$ is unknown. Other diffraction techniques such as resonant X-ray scattering experiments where only small sections of reciprocal space are probed at any given time are much more suitable for DW studies when $\mathbf{q}_{CDW}$ is known. Secondly, the intensity of the light generated by synchrotrons acts to reduce counting times allowing a number of samples to be tested quickly and also allows for weak features such as DW superstructure to be observed by overexposing main lattice peaks. In comparison lab-based diffraction sources have much weaker intensities requiring longer counting times increasing the chances weak superstructures may be missed.

Measurement procedure

The I19 beamline is very similar in its method of operation to the Supernova instrument shown and described in Chapter 2. The I19 beamline experimen-

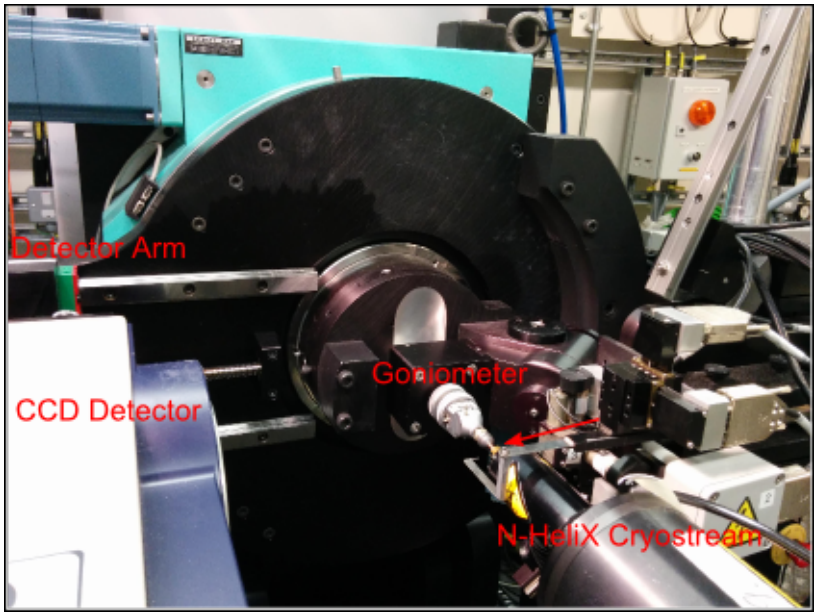

Figure 3.5: The Diamond Light Source I19 small molecule single crystal diffraction beamline. EH1 at the I19 beamline with a sample mounted on the goniometer ready to be measured, the red arrow indicates the direction of the incident X-ray beam.

tal hutch 1 (EH1) was used for the measurements presented here Fig.(3.5). A sample is mounted onto a microloop using grease or oil and secured to a goniometer and is then fixed to a four circle diffractometer. The sample is positioned into the centre of a tunable incident X-ray beam with a spot size at sample position of 175μm by 85μm. For the data presented here an incident beam with wavelength of 0.6889Å (18keV energy) and high photon flux [90] was used. The 18keV energy is used as standard on the I19 beamline and was suitable for our purposes as it did not correspond to any of the elemental absorption resonances found in $Na_2Ti_2Sb_2O$.

During operation the sample and the Rigaku Saturn 724 CCD area detector are moved through their rotational degrees of freedom such that complete maps of reciprocal space can be obtained. Temperatures lower than the T_{DW} of $Na_2Ti_2Sb_2O$ (115K) were achieved using an OxfordCryosystems N-HeliX Heluim gas open flow cryostat to cool the sample. Data collection and

analysis was performed using CryAlis Pro which also allowed for automation of the measurement procedure. In some cases, to prevent overexposure of the diffraction image, it was necessary to attenuate the flux incident on the sample by placing Al sheets of varying thickness in the path of the X-ray beam. To prevent decomposition of the air-sensitive samples they were stored in an argon atmosphere and were coated in Fomblin vaccum oil prior to mounting them on the beamline.

Several different crystals of $Na_2Ti_2Sb_2O$ were pre-screened by taking a small number of diffraction images using the I19 beamline and assessing their crystalline quality. These samples varied in size from being much larger than the incident beam to samples much smaller than the beam spot. In general the crystal quality of these samples was poor. The poor quality of the crystals is suspected to be due to the layered crystal structure. In larger samples mismatches between the orientation of the crystal layers were observed. These mismatches are thought to be the main cause of streaks of intensity which were observed to be propagating along the c-axis direction in the diffraction patterns obtained from $Na_2Ti_2Sb_2O$. An alternative explanation for these streaks of intensity is poor mosaicity within the crystal which at the [2,k,0] direction would manifest as vertical streaks. Whilst smaller samples limited this effect and in general were found to be of a superior crystalline quality, diffraction from the main lattice peaks was weak, limiting the ability to observe the weak superstructure reflections associated with CDW formation.

Given this, a compromise on crystal quality was made, resulting in larger samples being measured to maximize the possibility of observing superstructure reflections.

It is important to highlight the far from ideal shape of the crystals. Both $Na_2Ti_2Sb_2O$ and $Na_2Ti_2As_2O$ crystallize into large flat plates. Whilst the

grown crystals were cut down into more cuboid like shapes anisotropies in their dimensions remained. In general spherically shaped samples are best suited to diffraction experiments as they prevent sample shape anisotropies in the intensities of the Bragg peaks in the diffracted image.

Unfortunately both crystal quality and the sample dependent anisotropies limited the data analysis and prevented a full refinement to a crystal structure.

Data analysis and results

Diffraction data from a single crystal sample of $Na_2Ti_2Sb_2O$ was indexed above the density-wave transition at room temperature to lattice parameters of a=b=4.16(8)Å and c=16.578(6)Å in I4/mmm which is in close agreement with previously published values of a=b=4.155Å c=16.582Å [77]. The slight difference between c-axis values is likely due to c-axis disorder as a result of stacking faults. This c-axis disorder is most visible in the streaks of intensity seen in the (-2,k,l) plane Fig.(3.6a) for example between the (-2,1,-1) and the (-2,1,1) reflections. These streaks of intensity appear in the (h,k,n) planes as additional intensities at forbidden Bragg positions Fig.(3.6c) which break the h+k+l=2n reflection condition. These additional intensities are due to leak-through from lattice planes above and below the plane.

Superstructure reflections of the type $\mathbf{q}_{Sb1}$=(0.5,0,0) and $\mathbf{q}_{Sb2}$=(0,0.5,0) were observed in $Na_2Ti_2Sb_2O$ Fig.(3.6). These can easily be seen below T_{DW} in the (-2,k,l) and (h,k,0) lattice planes Fig.(3.6a) and Fig.(3.6c). Above T_{DW} the superstructure is not visible in the diffraction images Fig.(3.6a) and Fig.(3.6c).

Additionally the superstructure was found to have a periodic intensity modulation along the crystal c-axis with a repeat distance of 8 r.l.u Fig.(3.6d). The additional peaks seen in Fig.(3.6d) are thought to be due to poor crystal mosaicity as a result of different crystallites within the sample.

Whilst the superstructure intensities were shown to be temperature-dependent they appeared at 70K, well below the transition temperature of T_{DW}=115K expected from the heat capacity and resistivity measurements on $Na_2Ti_2Sb_2O$. This was due to a poorly calibrated thermometer at the sample position, whilst such a large difference in temperature is uncommon we were unable to find the source of the difference during the experimental time. Further measurements on the samples, which are presented in the next section, using a well calibrated lab based thermometer consistently showed the transitions of $Na_2Ti_2As_2O$and $Na_2Ti_2Sb_2O$to be concomitant with the anomalies seen in the transport properties. Therefore the temperature measurements taken during the I19 beamtime were deemed to be incorrect.

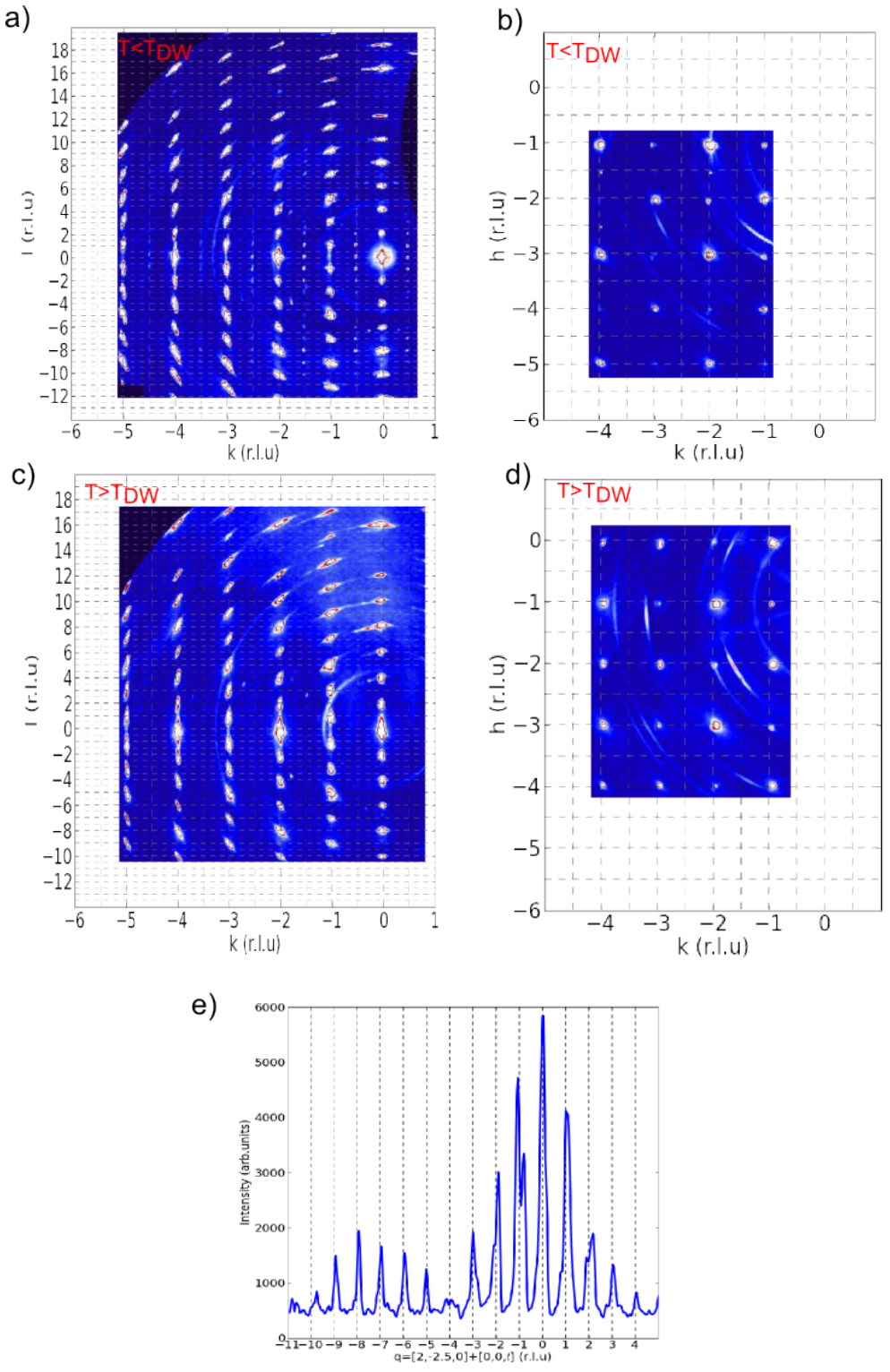

Figure 3.6: I19 diffraction data from $Na_2Ti_2Sb_2O$. a) $Na_2Ti_2Sb_2O$ [-2,k,l] plane below T_{DW} with the (0,0.5,0) superstructure clearly visible, the modulation of in the intensity of superstructure along the c-axis is plotted in e). b) $Na_2Ti_2Sb_2O$ (h,k,0) plane below T_{DW} with the superstructure visible at $\mathbf{q}_{Sb1}$=(0.5,0,0) and $\mathbf{q}_{Sb2}$=(0,0.5,0) type positions. Above T_{DW} in both the c) (-2,k,l) and d) n(h,k,0) plane the superstructure is not visible.

3.5.2 Lab-based X-ray Diffraction

To reconcile the discrepancy observed between the transition seen in the resistivity data at 115K and that observed in the I19 diffraction data at 70K further lab-based diffraction experiments using the Agilent Supernova X-ray diffractometer system described in Chapter 2 were performed. The lab-based diffraction experiment also provided the opportunity to explore the closely related $Na_2Ti_2As_2O$ compound.

Measurement procedure

Despite the error in the temperature measurement, the I19 experiment provided valuable insight into where to look for a superstructure and also which sample shapes were most likely to produce visible reflections, making a lab-based diffraction experiment possible.

A calibrated nitrogen cryostream was used to control the temperature of the sample providing a temperature range of 80K-400K. At low temperatures some icing occurred around the sample Fig.(3.7e) but did not impede the diffraction measurements and was kept to a minimum by positing the sample directly in the centre of the cryostream. All measurements were performed using the Molybdenum source with a wavelength of $0.70930\mathring{A}$. However during discussions with colleagues it was suggested that the Cu source may be more suited to these measurements.

Freshly grown batches of $Na_2Ti_2As_2O$ and $Na_2Ti_2Sb_2O$ were measured using this instrument and due to fewer constraints on instrument time were measured over a wider range of temperatures. Improvements in crystal quality were seen over older batches however these were not significant enough to enable a full data refinement and the leak-through of intensity observed in the I19 data was still present.

$Na_2Ti_2Sb_2O$

The supernova data from the $Na_2Ti_2Sb_2O$ revealed an identical superstructure to the one observed at the I19 beamline, with $\mathbf{q}_{Sb1}$=(0.5,0,0) and $\mathbf{q}_{Sb2}$=(0,0.5,0). Due to the small size of the crystal used in these experiments Fig.(3.7e) and the comparatively weak intensities produced by lab based X-ray sources the density-wave superstructure is very weak.

Line-cuts through main lattice reflections along the h and k lattice directions highlight the symmetric superstructure reflections at $\mathbf{q}_{Sb1}$=(0.5,0,0) and $\mathbf{q}_{Sb2}$=(0,0.5,0) Fig.(3.7d).

In the (2,k,l) lattice plane superstructure reflections were observed along [2,0.5,l] type directions. This superstructure is highlighted in Fig.(3.7d) for several different cuts along the [-2,k,l] direction. These reflections index to $\mathbf{q}_{Sb1}$=(0.5,0,0) and $\mathbf{q}_{Sb2}$=(0,0.5,0). Cuts along the [2,k,l] direction indicate that in

$Na_2Ti_2Sb_2O$ the density-wave forms in the ab-plane of the crystal and contains no c-axis component. Due to the low-intensity of the superstructure reflections the modulation in the c-axis direction observed in the I19 experiment was not able to be extracted from the lab-based X-ray data.

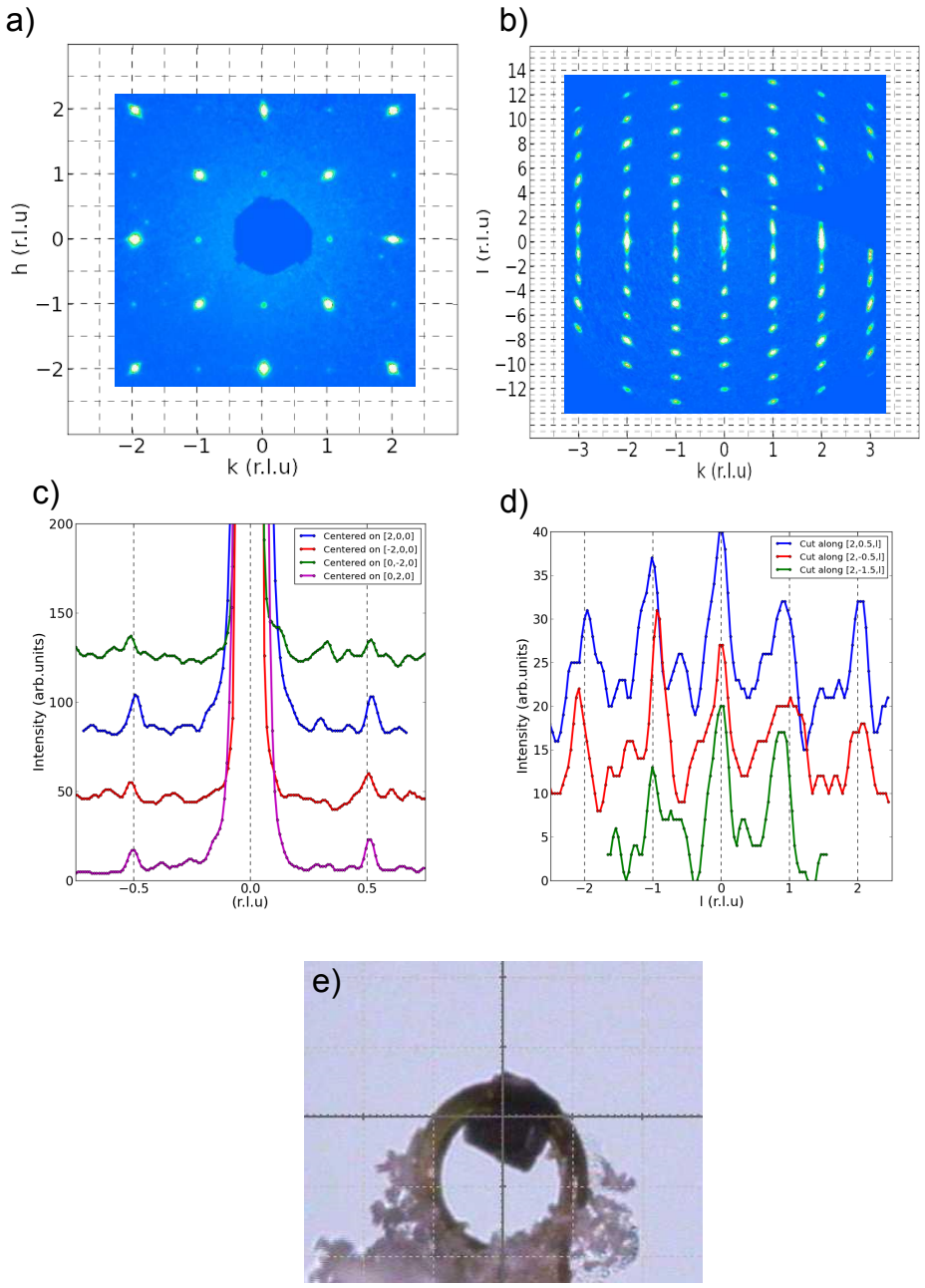

Figure 3.7: Single crystal XRD patterns of $Na_2Ti_2Sb_2O$ taken below T_{DW} at 95K. The (h,k,0) and (2,k,l) diffraction planes are shown in a) and b) respectively with the dotted lines acting as a guide for the eye highlighting the superstructure observed at q=(0.5,0,0) and (0,0.5,0). Superstructure reflections can be seen in c) line-cuts in the (h,k,0) plane through the main-lattice reflections at q=(0.5,0,0) and (0,0.5,0) type positions. This structure is also shown in d) with line-cuts along cut along the [2,m±0.5,l] directions in the (2,k,l) plane. The $Na_2Ti_2Sb_2O$ crystal used for these measurements is shown in d) attached to a 200μm loop and measures approximately 100μm by 100μm. Some ice crystals are present but did not obstruct the diffraction image

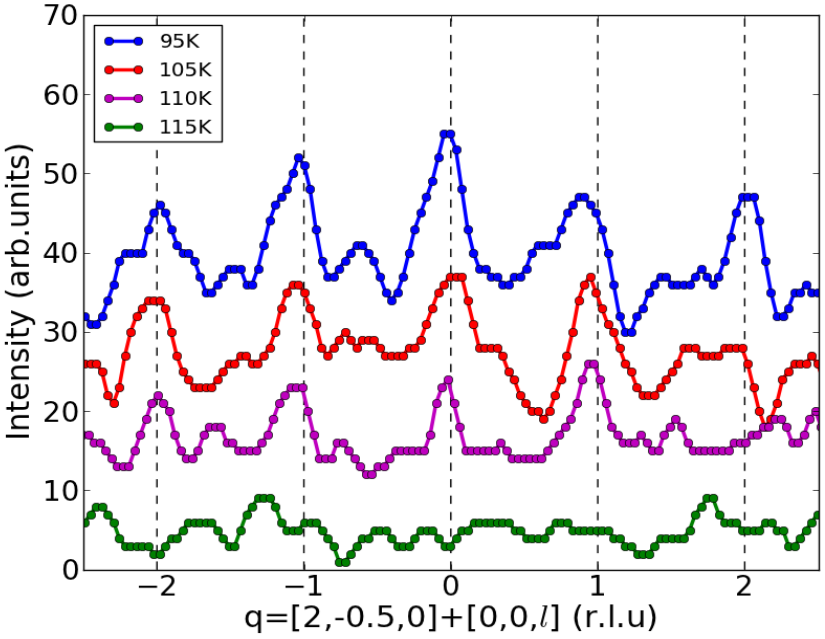

Figure 3.8: $Na_2Ti_2Sb_2O$ superstructure temperature-dependence. Line-cuts were taken along the [2,-0.5,l] direction over a temperature range of 95K to 115K where $T_{DW} \approx 115K$

Temperature-dependent diffraction data was taken at 5K steps through the T_{DW} and down to 95K Fig.(3.8). By extracting the intensity at superlattice positions, via a cut along the [-2,0.5,l] direction, it was possible to observe the appearance and increase in intensity of a set of superstructure reflections as the temperature was decreased below T_{DW}.

Below T_{DW} at T=110K weak superstructure peaks appear Fig.(3.8). The superstructure increases slightly in intensity as temperature is lowered further to 105K and 95K. The wave-vector of the superstructure between 110K and 95K is unchanged indicating that the density-wave is locked in and the transition between the metallic and the DW phase is sharp. Above T_{DW} at 115K there are no superstructure reflections. The abrupt appearance of superstructure peaks at a temperature between 110K and 115K is in agreement with the resistivity and heat capacity data on this material.

$Na_2Ti_2As_2O$

Several samples of single crystal $Na_2Ti_2As_2O$ were also measured using the supernova lab-based X-ray diffractometer. In general the $Na_2Ti_2As_2O$ crystals were of slightly higher quality than the $Na_2Ti_2Sb_2O$ crystals. This allowed larger single crystals to be measured without the diffraction pattern being dominated by twining. For the measurements presented here a large crystal with approximate dimensions of 2mm x 0.5-1mm and 1mm wide was used. Similar issues to those seen in $Na_2Ti_2Sb_2O$ samples were encountered in $Na_2Ti_2As_2O$ diffraction patterns. Most notably the forbidden reflections in the (h,k,0) plane due to a spread of intensity in the crystal c-axis direction was present. This dispersive intensity can be observed readily between the (-2,-1,1) and (-2,1,1) Bragg peaks in Fig.(3.9b). Given that the T_{DW} for $Na_2Ti_2As_2O$ is $\approx$320K diffraction measurements were taken over a temperature range of 200K-350K. Due to their air sensitivity the $Na_2Ti_2As_2O$ samples were coated in oil before being mounted onto the diffractometer.

Diffraction data taken from a $Na_2Ti_2As_2O$ sample revealed superstructure peaks associated with a charge-density-wave transition. At 230K superstructure reflections are clearly visible and locked into $\mathbf{q}_{As1}$= (0.5,0,0.5) and $\mathbf{q}_{As2}$=(0,0.5,0.5) type positions Fig.(3.9a) and Fig.(3.9c). In comparison no superstructure is visible in the diffraction images taken above T_{DW} Fig.(3.9b) at T=330K. Below T_{DW} symmetrical superstructure reflections were observed adjacent to the main lattice peaks in the (h,k,n$\pm$0.5) planes. This is highlighted in Fig.(3.9d) where line-cuts in the (h,k,0.5) plane along the [h,0,0] and [0,0,k] type directions show superstructure peaks adjacent to the main lattice reflections at T=230K.

Line-cuts through the diffracted intensity in the (-2,k,l) plane along the [0.5,l] direction show a superstructure at (0.5,0,0.5) type positions Fig.(3.9e).

The additional c-axis component in $Na_2Ti_2As_2O$ means that the wave-vectors of the CDW formation in $Na_2Ti_2As_2O$ and $Na_2Ti_2Sb_2O$ are not identical despite the similarities in their crystal structures.

A periodic modulation in the intensity of the $Na_2Ti_2As_2O$ superstructure along the c-axis identical to that seen in the $Na_2Ti_2Sb_2O$ was observed. As was the case in $Na_2Ti_2Sb_2O$ structure this modulation was found to have a period of 8 r.l.u Fig.(3.9e).

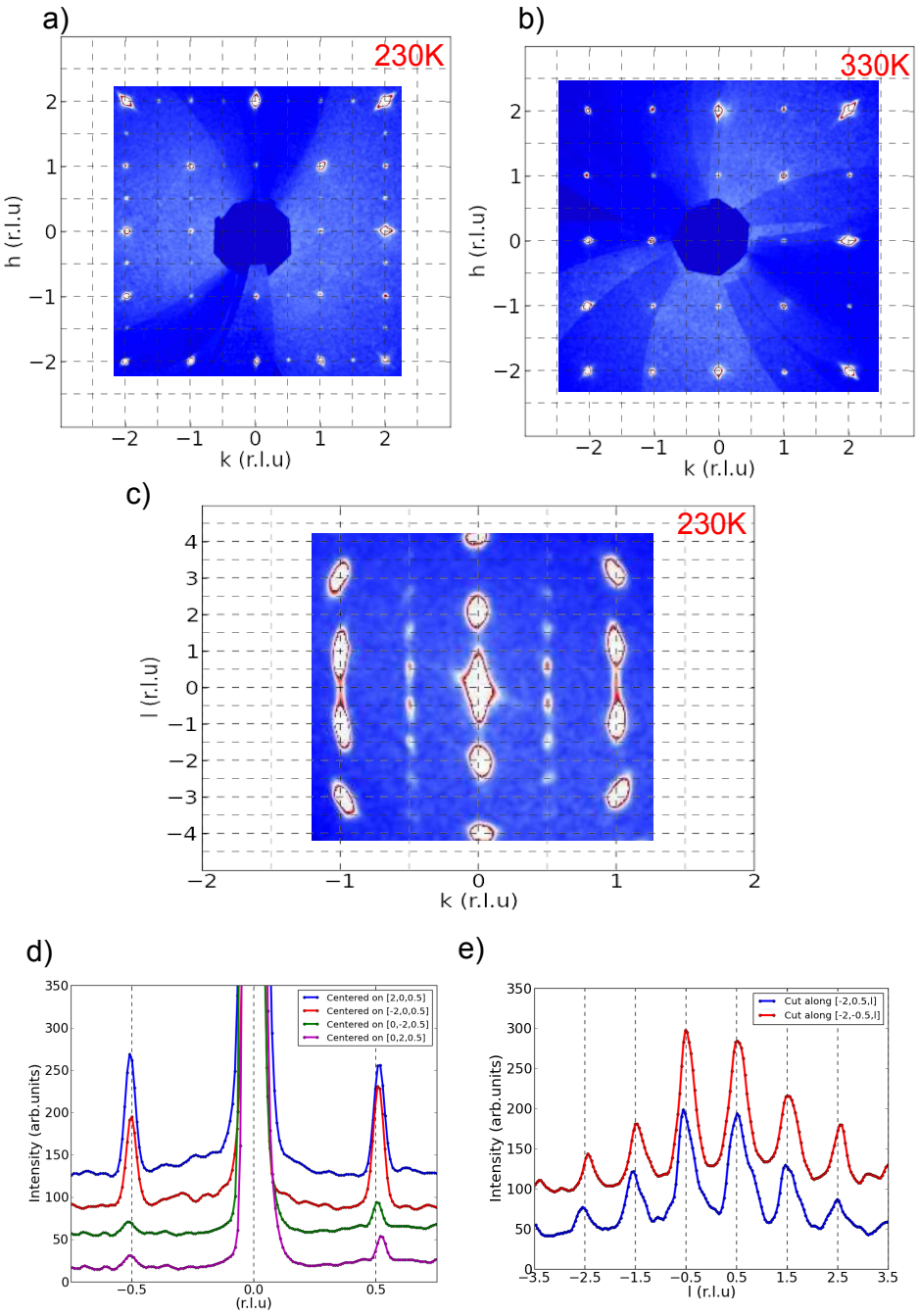

Figure 3.9: Diffraction data from single crystal $Na_2Ti_2As_2O$. Data below T_{DW} at 230K in the a) (h,k,0.5) and c) (-2,k,l) planes and for comparison above T_{DW} at 330K b) in the (h,k,0.5) plane. The (h,k,0.5) and (-2,k,l) planes below T_{DW} in a) and c) show superstructure reflections at $\mathbf{q}_{As1}$=(0.5,0,0.5) and $\mathbf{q}_{As2}$=(0,0.5,0.5) positions but are absent above T_{DW} in b). The superstructure peak intensities observed in the (h,k,0.5) plane are further highlighted in cuts through the main lattice peaks along the h and k directions in d). e)Taking a cut along the [-2,0.5,l]direction it can be seen that the superstructure shows a modulation in intensity similar to that observed in $Na_2Ti_2Sb_2O$.

In addition to the measurements above and below T_{DW} a full temperature-dependent study of the superstructure formation in $Na_2Ti_2As_2O$ was performed. Superstructure reflections were found to form between 330K and 300K in agreement with previous resistivity measurements on these materials. Once formed the h and k components of CDW remained fixed at $\mathbf{q}_{As1}$=(0.5,0,c) and $\mathbf{q}_{As2}$=(0,0.5,c). In contrast to this the superstructure intensity along the c-axis was found to be dispersive between 300K and 250K Fig(3.10) only locking into the 0.5c position at 250K.

Line-cuts along the [-2,0.5,l] direction demonstrate that at 330K no superstructure is present Fig.(3.11). At 300K broad but very weak features appear above the background, these become slightly more well defined at 280K and appear to have q_c component of $\approx$0.5. The superstructure at 270K is clearly visible above the background but remains broadly spread along the c-axis. In addition at 270K the DW has deviated away from the q_c=0.5 wave-vector and is at this temperature better described with $q_c\approx$0. This shift may be a result of two energetically favourable distortions of the crystal lattice competing over the temperature range from 320K to 250K. Further measurements cycling over this temperature range would be required to confirm this hypothesis or to ascertain if the 270K data is an anomalous result which should be disregarded. Cooling to 250K results in a drastic difference in the observed superstructure. The superstructure at 250K is sharper and of a higher intensity when compared to the superstructure seen at higher temperatures. At 250K the superstructure has a definite q_c component of 0.5. The superstructure present at 230K is similar in both sharpness and intensity to that seen at 250K, indicating that the DW transition is' locked' into a $\mathbf{q}_{As1}$=(0.5,0,0.5) and $\mathbf{q}_{As2}$=(0,0.5,0.5) type modulation at temperatures below 250K.

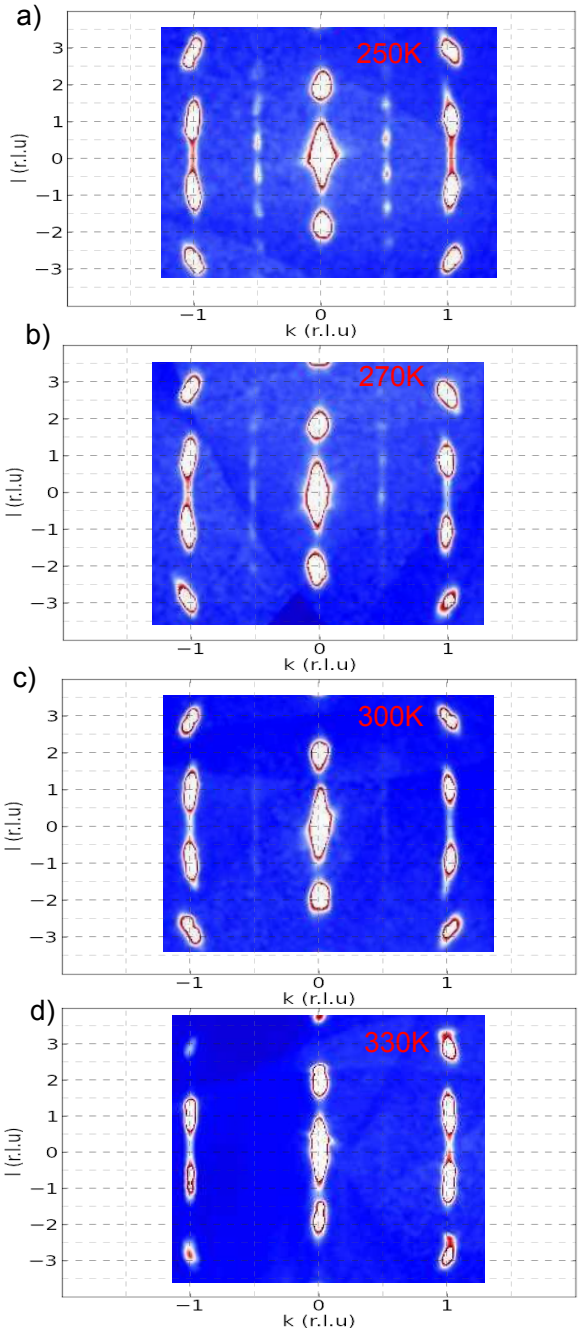

Figure 3.10: Temperature dependent diffraction data of the (-2,k,l) planes of single crystal $Na_2Ti_2As_2O$. Below T_{DW} at a) 250K, b) 270K,and c) 300K and above the density-wave transition at d)330K. Superstructure intensity can be seen in a), b) and c) along the k=0.5 type directions.

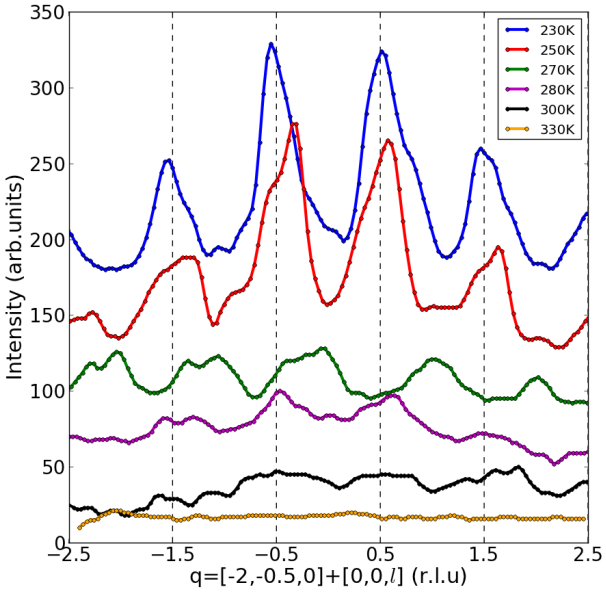

Figure 3.11: Temperature-dependent intensity line-cuts from $Na_2Ti_2As_2O$ diffraction patterns along the (-2,0.5,l) direction. An artificial offset has been applied to each line-cut to improve the clarity of the plot. Superstructure intensity is observed in the diffraction images taken below T_{DW} emerging between 330K and 300K.

3.6 Supporting data from collaborators

In this section I present supporting data performed by collaborators on $Na_2Ti_2Sb_2O$ and $Na_2Ti_2As_2O$ single crystals. This supporting data provides further details on the origins of the charge-density-wave state observed in the X-ray data and provides further evidence for a charge rather than spin-density type modulation.

3.6.1 μSR measurements

μSR measurements were performed on powder samples of single crystal $Na_2Ti_2As_2O$ and $Na_2Ti_2Sb_2O$ at the HiFi spectrometer at the ISIS Pulsed Muon facility. For both samples μSR measurements above and below

T_{DW} showed no static or fluctuating magnetism within the experimental sensitivity; suggesting that the DW in $Na_2Ti_2As_2O$ and $Na_2Ti_2Sb_2O$ is a CDW rather than a SDW. The measurements and data analysis associated with these conclusions was performed by collaborators at the University of Oxford.

3.6.2 ARPES measurements

ARPES measurements on single crystal $Na_2Ti_2Sb_2O$ samples were performed at the Syncrhotron Radiation Center (Wisconsin) and at the Swiss Light Source. Both measurements used a ScientaR4000 electron spectrometer with an energy resolution of 15-30meV and an angular resolution of 0.2^o. Horizontally polarized light with an energy of 54meV was used for both these experiments. These measurements and the data analysis associated with them was performed by collaborators at the Beijing National Laboratory for Condensed Matter Physics and Institute of Physics.

The Fermi surface of a freshly cleaved $Na_2Ti_2Sb_2O$ sample was measured above and below T_{DW}=115K Fig.(3.12a) and Fig.(3.12b). The features of the Fermi surface above the DW transition agree well with the non-magnetic band structure predicted by LDA theory Fig.(3.13d) and also with previous ARPES measurements on this system [86].

The in-plane k_x-k_y Fermi surface plotted in Fig.(3.13b) shows the expected square like electron and hole-bands about the Γ and X-points respectively. Above and below the transition a dramatic change in the spectral weight of the hole bands associated with the X-point is observed, indicative of the formation of a CDW.

Possible nesting vectors with q_1'=(0.5 ,0,0) and q_2'=(0,0.5 ,0) between the electron and hole-like bands are highlighted by green arrows in Fig.(3.13c). These nesting vectors connect parallel sections of the electron-like and hole-like

bands centered on the Γ and X-points respectively. Both the electron-like and hole-like bands cross the Fermi level above T_{DW}, Fig.(3.12e) and Fig.(3.12f), making them ideal candidates to be involved in Fermi-surface nesting. These proposed nesting vectors are in agreement with the superstructure observed in the X-ray diffraction experiments on these samples.

Paying closer attention to the temperature-dependent behaviour of the bands about the Γ and X-points Fig.(3.12) highlights that band-backfolding is observed at both points below T_{DW}. This band-backfolding can be attributed to the symmetry imposed by the doubling of of the Brillouin zone created by the formation of a CDW.

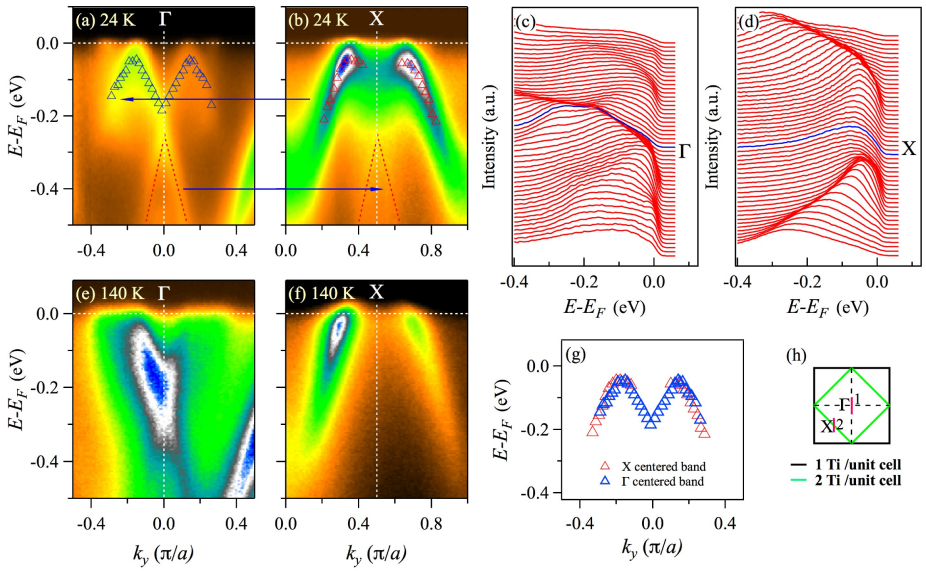

Figure 3.12: $Na_2Ti_2Sb_2O$ ARPES analysis. Momentum plots of the hole-band at the Γ-point and electron-band at the X-point below a) and b) and above e) and f) the DW transition temperature. A guide for the eye is provided in a) and b) highlighting the band-backfolding that occurs on going through the DW transition and the arrows between figures indicate the nesting vector between these two bands. Momentum distribution curves (MDCs) c) and d) provide a quantitative assessment of the band back-folding seen in a) and b) these MDCs were taken through the lines highlighted in h). The bands shown in c) and d) are fitted and plotted together in g). These figures were provided by collaborators at the Beijing National Laboratory for Condensed Matter Physics and Institute of Physics.

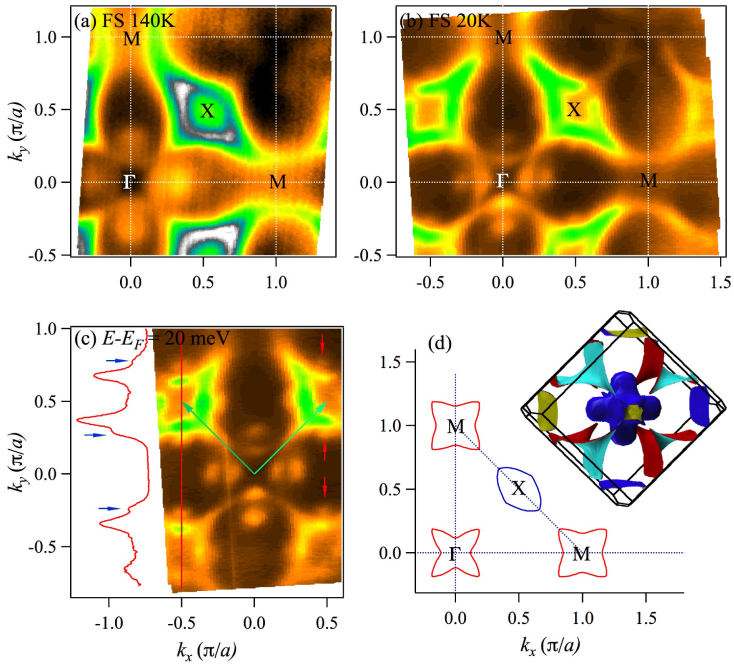

Figure 3.13: ARPES data collected from single crystal $Na_2Ti_2Sb_2O$. The Fermi-surface of $Na_2Ti_2Sb_2O$ is shown above the DW transition temperature at 140K in a) and below the DW transition at 20K in b). Both maps are integrated over an energy window of ±10meV. To highlight the nesting vector the integration window was adjusted to 20meV above E_f c). Green arrows show the fitted nesting vectors and the line cut through the center of the X-point show shoulder like features to the electron band. There is good agreement between the fitted Fermi-surface d) and that predicted local-density approximation (LDA) calculations on $Na_2Ti_2Sb_2O$ shown as an inset in d). Horizontally polarised light with an incident energy of 54eV was used for these measurements.These figures were provided by collaborators at the Beijing National Laboratory for Condensed Matter Physics and Institute of Physics

3.7 Discussion

The X-ray diffraction results presented in this chapter strongly support the existence of a charge-density-wave in the layered Ti-based oxy-pnictides $Na_2Ti_2Sb_2O$ and $Na_2Ti_2As_2O$. The $\mathbf{q}_{Sb1}$ and $\mathbf{q}_{Sb2}$ found in $Na_2Ti_2Sb_2O$ are compatible with nesting vectors observed in ARPES measurements made on these materials. These ARPES measurements Fig.(3.13) and Fig.(3.12) per-

formed by collaborators, Junzhang Ma and Tian Qian, suggest a nesting between the hole-like bands centered at Γ and electron-like bands centered about the X-point, with a q_{CDW}=(0.5,0.5,0). Recent ARPES measurements on $Na_2Ti_2Sb_2O$ have been successful in measuring the opening of a gap at E_f at the X-point lending more support to this CDW hypothesis [86].

The observation of a similar superstructure in $Na_2Ti_2As_2O$ and the closely related nature of its crystal structure to $Na_2Ti_2Sb_2O$ suggests that this material undergoes a similar CDW transition. Unfortunately $Na_2Ti_2As_2O$ samples are more sensitive to air than $Na_2Ti_2Sb_2O$ making ARPES measurements on these samples more difficult and as such no ARPES data has been obtained or found in the literature on $Na_2Ti_2As_2O$. However theoretical calculations indicate that the band structure is very similar between the two materials.

To understand the origin of the additional c-axis component of $\mathbf{q}_{As1}$ and $\mathbf{q}_{As2}$ in $Na_2Ti_2As_2O$ an ARPES k_z study on the material would be required.

Of particular interest is the possibility that the CDW in $Na_2Ti_2As_2O$ sample results in a fully gapped Fermi-surface, evidenced by the MIT transition seen in the resistivity data. Whilst common to one-dimensional materials where the Fermi surface is perfectly nested such nesting is rare in CDW system with a higher dimensionality.

The two q-vectors seen in both samples could be the result of one of two scenarios, either there exists two one-dimensional modulations that have formed separate spacial domains within the material or the measured q-vectors coexist in space. Given that X-ray diffraction is a bulk sensitive technique the diffraction data alone cannot be used to resolve this. A comparison of the relative intensities of the two sets of superstructure modulations could have been used to hint at which scenario is more likely. For example had the intensities of the sets of superstructure reflections been equal a two-q scenario

would have been more likely rather than the alternative of two equally sized domains. Unfortunately the quality of the diffraction data meant that such an analysis was not possible.

On the other hand the ARPES measurements are surface rather than bulk sensitive measurements. The proposed nesting vectors obtained from these measurements support the idea that the CDW is two-q rather than two domains of one-q modulations for several reasons. Firstly the ARPES data observed a four-fold symmetry below T_{DW}in the hole-like and electron-like Fermi sheets that surround the Γ-point. If it were the case that the DW transition was a result of a single q-vector one would expect energy gaps to open only at the two corners of the Γ centered band.

Alternatively one could envisage a scernario where the ARPES data was the measurement of two superimposed single-q domains, if this were the case the four-corners of the Γ centered band would remain ungapped due to a superposition at these points of a gapped Fermi-surface and an ungapped Fermi-surface.

Both of the scenarios suggested above are inconsistent with the ARPES data on $Na_2Ti_2Sb_2O$. Hence in the $Na_2Ti_2Sb_2O$sample it is suggested that the CDW is two-q with nesting vectors of the type $\mathbf{q}_{Sb1}$=(0.5,0,0) and $\mathbf{q}_{Sb2}$=(0,0.5,0).

Without ARPES data or higher quality diffraction data the two scenarios were indistinguishable in the $Na_2Ti_2As_2O$compound. However given the differences in both the nesting vectors of $Na_2Ti_2Sb_2O$ and $Na_2Ti_2As_2O$ and the difference in the resistivity the CDW nesting in $Na_2Ti_2As_2O$ may be different to that seen in $Na_2Ti_2Sb_2O$.

The intensity modulation of approximately $8c^*$ seen in the superstructure of both $Na_2Ti_2As_2O$ and $Na_2Ti_2Sb_2O$ corresponds to the height of the pnictide ion above or below the Ti-O layer (c/8). The correspondence between the superstructure intensity modulation and the position of the pnictide ions

demonstrates that the CDW involves the periodic distortion of the Ti-pnictide bonds. The involvement of the pnicitde in CDW formaiton is perhaps unsurprising given the dependence of T_{DW} on the size of the pnictide ion.

The two-q CDW system shown here for $Na_2Ti_2Sb_2O$ is very different to the proposed model for the closely related compound $BaTi_2Pn_2O$ materials (Pn=As or Sb) [87]. In these structurally analogous materials similar anomalies have been observed resistivity measurements and are thought to be due to charge-ordering. However no lattice superstructures have been found in electron diffraction measurements on $BaTi_2Pn_2O$ to support the a conventional charge-density wave type model. Instead it has been suggested that the resistivity anomalies and also the change in symmetry (P4/mmm - P/mmm) seen as the $BaTi_2Pn_2O$ materials go through T_{DW} can be explained by intra-unit-cell charge-order. This involves the redistribution of charge on the Ti two distinct Ti sites and results in the breaking of local rotational symmetry but does not result in translational symmetry breaking. Such a redistribution of charge is reported to reproduce well the experimentally observed change in space group symmetry and the resistivity anomalies [87].

Future X-ray diffraction measurements on $Na_2Ti_2As_2O$ and $Na_2Ti_2Sb_2O$ should focus on establishing a thorough temperature dependence of the superstructure reflections above and below the transition temperature. Such measurements would allow the order parameter for both materials to be established and provide an estimate for T_{DW}. Recent STM studies on the related $Ba_{1-x}Na_xTi_2Sb_2O$ compound [91] have been used to observe a CDW modulation in these materials, an STM measurement of $Na_2Ti_2As_2O$ and $Na_2Ti_2Sb_2O$ would allow the CDW in these materials to be further characterised and provide complementary data for the X-ray diffraction experiments presented here.

3.8 Conclusion

Superstructure reflections have been observed in the $Na_2Ti_2Sb_2O$ and $Na_2Ti_2As_2O$ members of the Ti-based oxy-pnictides. These are the first superstructure modulations to have been observed in the oxy-pnictides. The appearance of the superstructure reflections coincided with anomalies seen in both materials at T_{DW} in resistivity, heat capacity and magnetic susceptibility. In $Na_2Ti_2Sb_2O$ the superlattice peaks had wave-vectors of the type $\mathbf{q}_{Sb1}$=(0.5,0,0) and $\mathbf{q}_{Sb2}$=(0,0,0.5) which are in agreement with a nesting vectors suggested in both theoretical calculations and ARPES data.

For $Na_2Ti_2As_2O$ reflections of the type $\mathbf{q}_{As1}$=(0.5,0,0.5) and $\mathbf{q}_{As2}$=(0,0.5,0) were observed and μSR measurements ruled out any magnetism.

Diffraction data in conjunction with ARPES and μSR measurements have been used to determine the DW transition in $Na_2Ti_2As_2O$ and $Na_2Ti_2Sb_2O$ to be due to the formation of a commensurate charge-density wave.

Given the ease with which the DW transition can be tuned this family of materials provides an ideal testing ground developing an understanding two-dimensional CDWs and their competition with conventional superconductivity.

A manuscript is currently in preparation for the submission of this work to a peer-reviewed journal.

Chapter 4

Density-Wave formation in Ni_xZrTe_3.

4.1 Introduction

Crystalline materials with structures which exhibit quasi-one-dimensional or quasi-two-dimensional electronic bandstructures are susceptible to density-wave transitions. Such materials often also exhibit superconducting phases [66, 92–96]. These materials raise interesting questions about the crystalline structure and associated bandstructure required for these phases to exist. To answer these questions well understood model materials which exhibit both DW states and superconducting phases must be fully characterized.

Understanding the interplay between the density-wave transition and superconductivity is possible through observation of changes in the associated bandstructure when either or both of these phases are suppressed or promoted. The suppression or modification of CDW states is often achieved through the application of hydrostatic pressure [97–100], but such a technique restricts the types of characterization measurements that can be performed. For example, angle resolved photoemiession (ARPES) measurements are not compatible with the application of hydrostatic pressure. As bandstructure measurements have the potential to provide a wealth of information on the formation of CDW and superconducting phases alternative methods of applying pressure to samples are desirable.

One alternative which is compatible with ARPES measurements is the application of chemical pressure. Through the substitution or intercalation of suitable iso-valent chemical species it is possible to apply pressure within the crystal unit-cell. This method is distinct from doping of the crystal lattice in that the intercalated atom does not donate to or accept electrons from the parent compound.

Intercalation as a means of inducing chemical pressure, however, brings

with it additional problems. Unlike the parent compounds, intercalated crystals often rely on guest ions taking up positions on non-crystallographic sites sitting in van-der Waals gaps between crystal layers or chains. As such the distribution of the intercalated ion can often be inhomogenoues within the material. This inhomogeneity, as well as causing defects in the compound, can lead to areas within the same intercalated crystals which have an abundance or absence of the intercalated species.

The inhomogeneities introduced by the intercalate mean that bulk measurements, such as X-ray diffraction, on large samples of intercalated crystals often encounter problems. Crystal quality often suffers as a result of the intercalation. Several domains of differing intercalate concentration can form in a single crystal and all will contribute to the diffraction pattern. Distinguishing between these different regions can be challenging.

On the other hand surface-sensitive techniques such as ARPES often probe just a single domain. Surface sensitive techniques do not therefore suffer from the inhomogeneities within the bulk of the crystal to the same extent. However, a disadvantage is that surface measurements may probe a region which is not representative of the bulk crystal.

X-ray diffraction and ARPES are both techniques that can provide vital information on the effect of intercalation on both the superstructure associated with CDW formation and the bandstructure of the intercalated compound. However, intercalated compounds present many difficulties to these experimental techniques.

In this chapter, I present preliminary X-ray diffraction and ARPES data on a series of Ni_xZrTe_3 crystals. $ZrTe_3$ is a quasi-two-dimensional material in which a CDW state and superconductivity have been observed. Hydrostatic pressure has been shown to suppress the CDW state and promote the supercon-

ductivity in resistivity measurements on $ZrTe_3$ [101]. More recent resistivity work has shown that chemical pressure in the form of intercalated Ni [102] or Cu ions [103] is also capable of manipulating the CDW state.

Ultimately the aim of X-ray diffraction and ARPES measurements on Ni_xZrTe_3 would be to establish the effects of chemical pressure on the CDW state in $ZrTe_3$. The measurements reported here were performed with this aim in mind, but as I shall show, the results raise questions about the distribution and composition of the Ni-intercalates. As a result, the main value of the study has been to help to characterize the nature of the Ni-intercalation as well as highlighting and suggesting methods to overcome the difficulties involved in performing ARPES and diffuse X-ray diffraction on intercalated layered compounds. Although this work does not reach any quantitative conclusions about the effect of Ni intercalation on the CDW in $ZrTe_3$, it is an important stepping stone in understanding the considerations that must be made when measuring these compounds and other intercalated materials using X-ray diffraction and ARPES.

4.2 Electronic and structural properties of $ZrTe_3$

4.2.1 Crystal Structure

$ZrTe_3$ is a layered quasi-two-dimensional material consisting of chains of $ZrTe_3$ tetrahedra extending along the crystal b-axis. The prismatic chains fit together in an alternating 180^o rotation arrangement to form a single layer Fig.(4.1). These layers are stacked along the crystallographic c-axis direction and weakly bound together by van der Waals forces. The layered nature of the material leads to anisotropies in its physical properties and also creates an axis about which the crystals preferentially cleave. $ZrTe_3$ is monoclinic crystallizing into

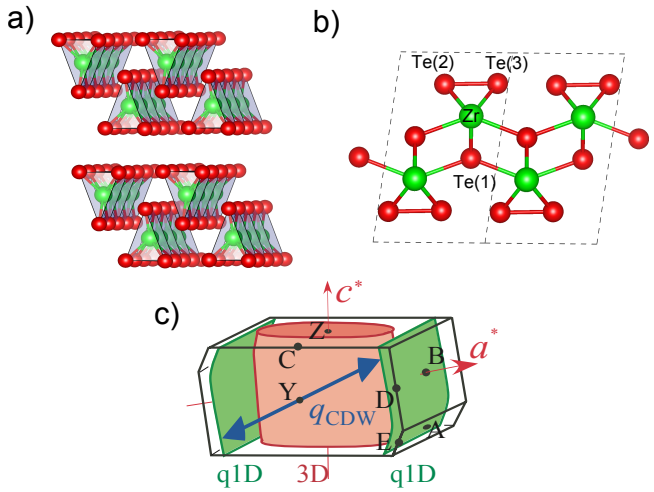

Figure 4.1: $ZrTe_3$ crystal structure and band-structure. Crystal structure from an offset perspective a) showing two of the weakly bonded layers separated by a gap each with prismatic $ZrTe_3$ chains extending along the crystallographic b-axis. The same crystal structure is shown in b) viewed along the b-axis with the three different Te sites labeled and the bond between Te(2) and Te(3) highlighted. The conventional unit-cell is depicted by dashed lines. The Brillouin Zone and predicted Fermi-surface c) reveal two quasi-one-dimensional Fermi-surface sheets with a nesting vector suitable for the formation of a CDW. Figure adapted from Ref. [104].Reprinted figure with permission from [104]. Copyright 2009 by the American Physical Society. `http://link.aps.org/doi/10.1103/PhysRevB.80.075423`

the $P2_1/m$ space group with lattice parameters a=5.89Å b=3.92Å c=10.10Å β= 97.81^o [105].

Cu and Ni have both been successfully intercalated into $ZrTe_3$. Concentrations of x=0.05 have been reported in Ni_xZrTe_3 [102] and Cu_xZrTe_3 [103].

In terms of the crystal structure, this intercalation results in both cases in the expansion of the c-axis lattice parameters. For Ni_xZrTe_3 (x=0.05 c=10.16Å) [102] and for Cu_xZrTe_3 (x=0.05 c=10.11Å) [103].

The Ni and Cu atoms are thought, because of the difference in their size compared to Zr, to reside between $ZrTe_3$ layers as opposed to substituting directly into the $ZrTe_3$ layer [102].

4.2.2 Electronic Properties

Resistivity measurements on pure $ZrTe_3$ have shown significant anisotropies in its electronic response. Along the in-plane crystallographic a and b-axes, the resistivity of $ZrTe_3$ is approximately ten times smaller than the resistivity along the c-axis i.e a (1:1:10) along the (a:b:c) axes [10]. This large anisotropy is unsurprising in such a quasi-two-dimensional layered structure where the conduction along the c-axis is between weakly van der Waals bounded layers.

Of greater significance are the temperature-dependent resistivity anomalies [10] which have been observed along the a and c crystallographic directions Fig.(4.2). These anomalies appear at 63K and are indicative of the formation of a CDW. An anomaly in the specific heat has also been observed at T_{CDW}=67K [106] close to that seen in the resistivity data. Below the CDW transition $ZrTe_3$ retains its metallic nature. At 2K, $ZrTe_3$ becomes superconducting. This superconductivity has been shown to be filamentary in nature and parallel to the a-axis [107].

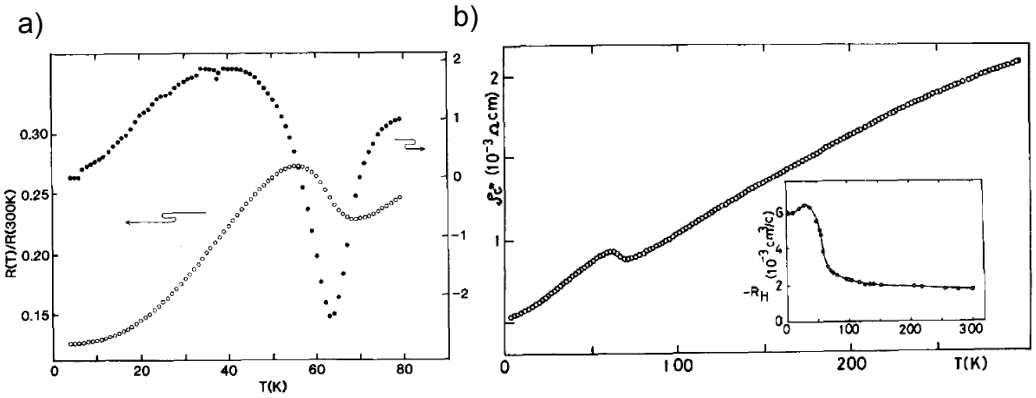

Figure 4.2: Resistivity measurements from $ZrTe_3$. Taken along the a) crystallographic a-axis and b) along the c-axis. The inset in b) shows results from measurements of the hall coefficient. Graphs reproduced from Ref. [10].Reprinted from Ref. [10]. Copyright (1984), with permission from Elsevier

4.2.3 CDW formation in $ZrTe_3$

The anomalies seen in the resistivity and heat capacity data on $ZrTe_3$ have, via a number of experimental techniques including IXS, ARPES and electron microscopy, been confirmed to be due to the formation of a charge-density wave.

Electron microscopy measurements on pure $ZrTe_3$ revealed a CDW superstructure [108]. The superstructure appearing at a T_{CDW}=63K was found to be incommensurate with the lattice with a q_{CDW}=($0.93a^*$,$0.33c^*$).

Given that the ab-plane is parallel to the $ZrTe_3$ layers and the similar anisotropies observed in the a and b-axis resistivity, it is interesting that there is no b-axis component in the q_{CDW}. This lack of a b-axis component in the q_{CDW} has been explained by ARPES measurements on $ZrTe_3$ the details of which are covered later in this section.

IXS measurements on $ZrTe_3$ confirmed the lattice modulation seen in the electron microscopy via the observation of a giant Kohn anomaly in the phonon spectrum at q_{CDW} [57]. A giant Kohn anomaly is the suppression of a phonon

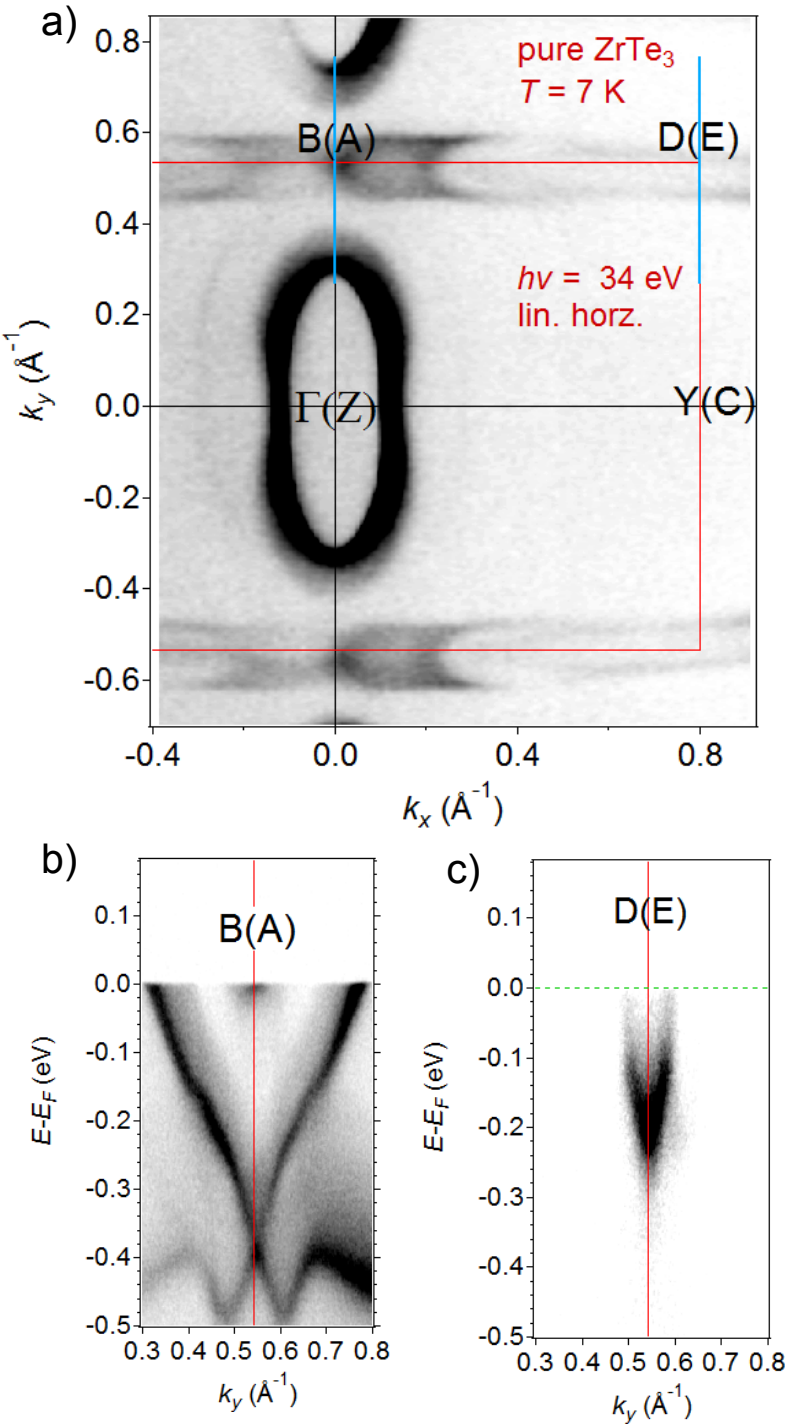

Figure 4.3: $ZrTe_3$ bandstructure features.a) Fermi surface map of $ZrTe_3$ obtained during this work highlighting the 1^{st} Brillioun Zone (red line) with the high-symmetry points labeled. Cuts through (blue lines) the B(A) and D(E) points are shown in b) and c) respectively.

mode resulting in the static distortion of crystal lattice due to the periodic modulation of charge. The presence of the Kohn anomaly also highlights the strong electron-phonon coupling seen in these materials and identifies one of the key characteristics of the formation of a charge-density wave.

ARPES measurements Fig.(4.3a) and bandstructure calculations [105] Fig.(4.1c) provide a detailed picture of the Fermi surface in $ZrTe_3$.

The Fermi-surface of $ZrTe_3$ is quite simple, it is comprised of a three-dimensional hole-like band about the Γ-point and a quasi-one-dimensional sheet extending from B(A)-D(E) in the Brillioun zone. The quasi-one-dimensional bands extending from the B(A) to D(E)-points in the Brillouin zone are a result of the overlapping $5p_x$ orbitals of the neighboring Te(2) and Te(3) atoms Fig.(4.1b) [17] . These sheets provide the perfect condition for the Fermi-surface nesting which drives the formation of the CDW in this material. The q_{CDW} obtained from the IXS and electron diffraction measurements can be be satisfied between these parallel Fermi-surfaces [17]. Confirmation of the involvement of B(A)-D(E) band in the formation of the CDW state has been provided by the observation of a depletion in spectra at the Fermi-surface most clearly observed at the D(E)-point below T_{CDW} [17]. The shift in spectral weight away from the Fermi-surface has been seen in temperature-dependent energy distribution curves taken through the D(E)-point [17]. Band-backfolding, a signature of CDW formation, has not been reported in this material. The 3D band about the Γ-point, which is due to Te p orbitals hybridized with Zr d states [26], has been shown to have very little dependence on temperature down to 6K [17], indicating it is not involved in the DW transition seen at 63K. Below T_{CDW} a sharp increase in spectral weight is observed at the B(A)-point.

4.2.4 Hydrostatic and Chemical Pressure

Hydrostatic pressure, Ni-intercalation and Cu-intercalation have all been shown to influence the CDW and superconductivity found in pure $ZrTe_3$.

Measurements of the resistivity of $ZrTe_3$ under hydrostatic pressurization have revealed an interesting phase diagram as pressure is applied [101]. Initially as pressure is increased T_{CDW} is seen to increase and T_{SC} decrease up to pressures of ≈3GPa at which point the low temperature superconductivity is fully suppressed Fig.(4.4). Increasing pressure further beyond 3GPa was shown to decrease the T_{CDW}. At ≈ 5GPa of hydrostatic pressure the CDW was completely suppressed and the superconductivity reemerged. Further increases in pressure resulted in an increase in the T_{SC} up to ≈5K at pressures of 11GPa [101].

Chemical pressure through the intercalation of Ni ions between $ZrTe_3$ layers has been shown to suppress the CDW state. Resistivity measurements on Ni_xZrTe_3 where x=0.05 have shown a decrease in T_{CDW} from 63K in the pure sample to 41K in the intercalated species [102].This intercalation of Ni also had the effect of inducing bulk superconductivity at a T_{SC}=3.59K [102] rather than the filamentary superconductivity seen in the pure compound at T_{SC}=2K.

Cu-intercalation has a more pronounced effect on the CDW anomaly seen in the resistivity data. For Cu-intercalation the anomaly is much weaker than that seen in $ZrTe_3$ and occurs at a lower T_{CDW}≈50K [103]. Cu_xZrTe_3 also exhibits a similar bulk superconductivity to that observed in Ni_xZrTe_3 with a T_{SC}=3.8K.

From these results it is clear that intercalation of both Ni and Cu can be used to influence the formation of the CDW state seen in $ZrTe_3$.

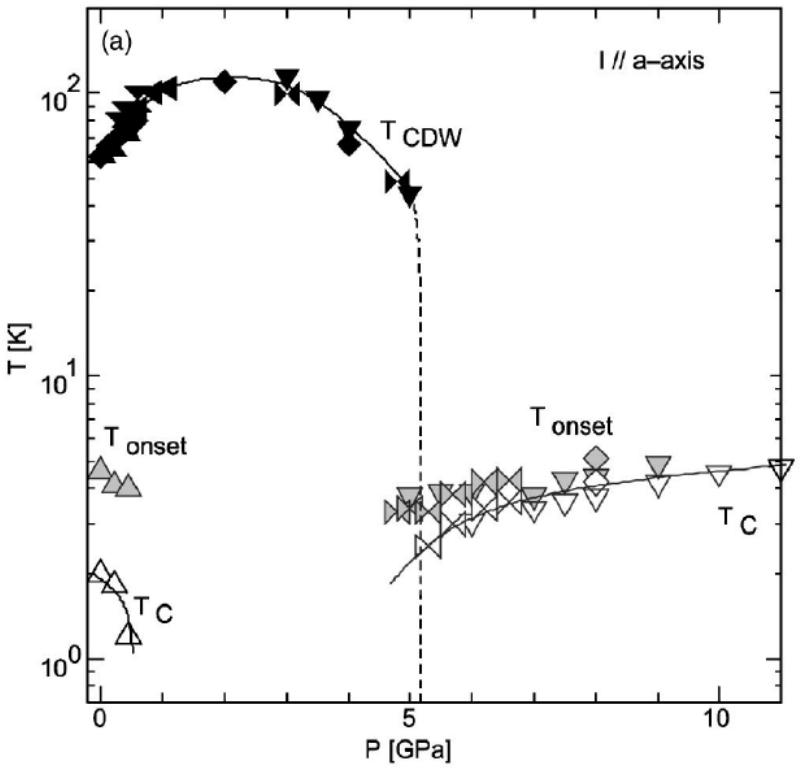

Figure 4.4: Effects of hydrostatic pressure on the DW and superconductivity seen in $ZrTe_3$. Where T_{onset} marks the appearance of superconductivity. Figure reproduced from Ref. [101].Reprinted figure with permission from Ref. [101]. Copyright (2005) by the American Physical Society. `http://link.aps.org/doi/10.1103/PhysRevB.71.132508`

4.3 Ni-intercalated $ZrTe_3$

Ni_xZrTe_3 compounds provide a possible way of investigating the effects of pressure on the bandstructure and the nesting vector of the CDW without the need for additional experimental apparatus. In the work reported here a series of Ni_xZrTe_3 samples were measured by ARPES. The results show changes to key features of the Fermi surface due to the presence of Ni. Measurements of this type could in future be used to ascertain the effects of chemical pressure on the Fermi surface of $ZrTe_3$. In addition, preliminary X-ray diffraction experiments were also performed on the series of Ni-intercalated $ZrTe_3$, with the aim of observing any change in the intensity or modulation of the superstructure associated with the formation of the CDW. These experiments confirmed the presence of a CDW in all the Ni_xZrTe_3 compounds but no change in q_{CDW} could be detected. The measurements highlighted the difficulties which can arise from the measurement of intercalated samples with a weak CDW superstructure.

4.3.1 Sample Characterization

To investigate the suppression of the CDW state seen in Ni_xZrTe_3 a series of crystals with differing Ni-content were grown by C.Petrovic. These were grown using the chemical vapour transport method described in Ref. [102] and characterized using resistivity measurements by C.Petrovic Fig.(4.5). Initially each Ni-concentration was given a batch number and Ni-concentration based on the growth parameters; X162=$ZrTe_3$, X58=$Ni_{0.05}ZrTe_3$, X62=$Ni_{0.1}ZrTe_3$ and X60=$Ni_{0.15}ZrTe_3$. However, results from X-ray photoemssion and energy dispersive X-ray experiments and the resistivity data presented by C.Petrovic suggest lower concentrations of Ni than expected from preparation conditions.

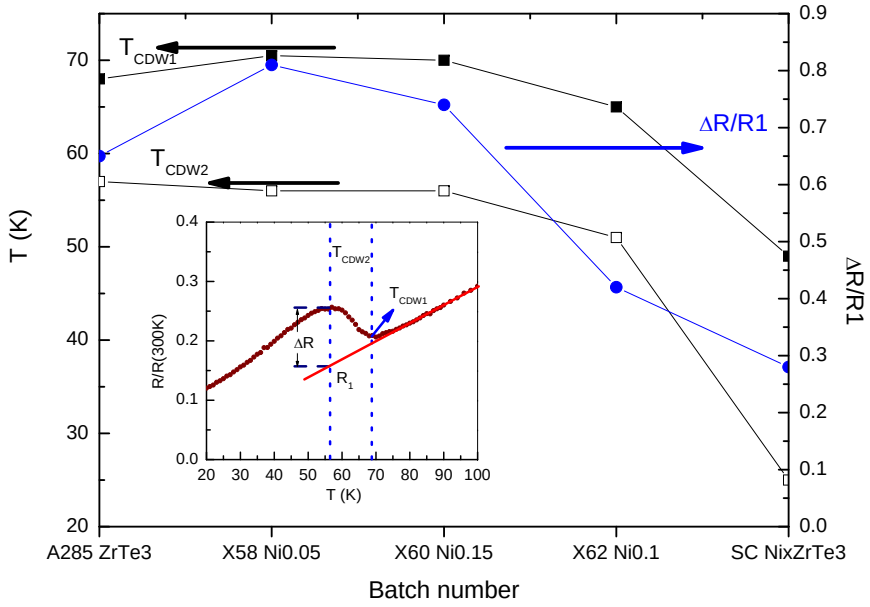

Figure 4.5: a-axis resisitivity data for a series of Ni-intercalated crystals. The inset shows the main features of the resistivity profile. Figure produced by C.Petrovic

The general resistivity curve of $ZrTe_3$ Fig.4.5(inset) shows two distinct temperature dependent features common to all of the $ZrTe_3$ compounds, an upturn in resistivity occurring at $T_{CDW}1$ and a return to the metallic curve occurring at $T_{CDW}2$ a few kelvins below $T_{CDW}1$. These two points can be characterized together using the parameter $\Delta R/R_1$ shown in Fig.(4.5inset). A small increase in $\Delta R/R_1$ is observed in the X58 and X60 samples, whilst X62 shows a decrease in resistivity more in line with that observed in Ni_xZrTe_3x=0.05 [102]. The Ni-dependent changes in resistivity provide some evidence for the presence of Ni in the $ZrTe_3$ and indicate that it has an effect on the CDW formation in this material.

Additional characterization of the chemical composition of the samples was performed via an X-ray photoelectron spectroscopy (XPS) study on the I05 beamline at the Diamond Light Source. XPS enables the identification of

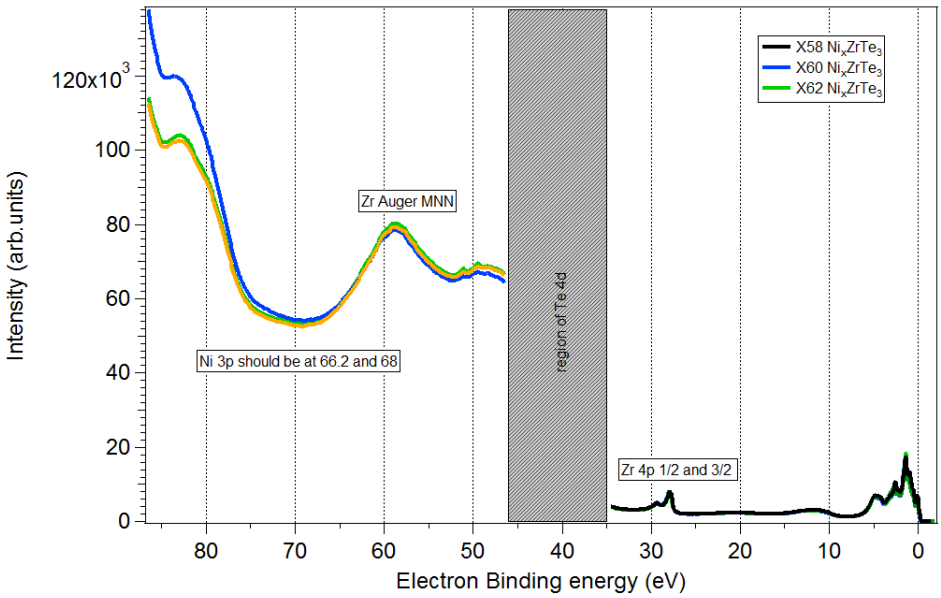

Figure 4.6: XPS analysis of the intercalated Ni_xZrTe_3 samples. Data taken using the I05 ARPES beamline operating at high incident photon energies 80-120eV. The data suggests strongly that the doping in the samples in nominal rather than the composition suggested by the growth parameters.

the chemical elements present in the materials through photoemission of their core electrons. In the case of the intercalated series the Zr 4p states are clearly visible in the XPS spectrum Fig.(4.6). The region of energy where the Te valance band states are present was unable to be measured due to the risk of damaging the detector through overexposure. In the energy range where the Ni valance band states were expected to be visible no features where observed, this is most likely due to either low levels of Ni present in these materials or as a result of the cleaved surface being an Ni-poor region of the crystal.

In addition to the XPS analysis, an energy dispersive X-ray analysis of the chemical composition was also performed. This analysis also failed to detect Nickel in the Ni_xZrTe_3 series above a constant background of x=0.015. However, the resistivity measurements and growth parameters indicate that there is Ni-content, albeit at an unknown low-concentration, within the series.

Future measurements on Ni_xZrTe_3 where the destruction of the sample is

not problematic could employ powder X-ray diffraction refinement or mass spectrometry to determine the exact Ni-content of the samples, although at the low levels expected to be present in the series the Ni-content may still be difficult to detect.

As a result of these measurements, samples will be labeled exclusively by sample code rather than Ni-content with X162 being the pure compound and the others X58,X60 and X62 containing unknown but interesting levels of Ni-intercalation.

Samples of the Ni_xZrTe_3 are black, shiny, brittle and do not react with the atmosphere. No visual differences between the Ni_xZrTe_3 series was observed. Over the course of these experiments no changes were observed in the visual appearance or the structural integrity of the crystals suggesting that the samples were not degrading over time or leeching Ni to the atmosphere.

4.4 I19 Diffraction Data

Associated with the charge-density-wave phase is the formation of a superstructure in the X-ray diffraction patterns produced by the material. The series of Ni-intercalated samples were measured on the I19 beamline at the Diamond Light Source in experimental hutch 2 (EH2) to observe possible changes in q_{CDW} and superstructure intensity due to the chemical pressure exerted by the Ni-intercalation.

The main lattice reflections of the Ni-compounds were greatly overexposed using a monochromatic X-ray beam (18keV) in an attempt to see the weak superstructure reflections associated with the formation of the CDW.

The I19 EH2 diffractometer is a four-circle diffractometer with an Oxford Atlas CCD detector. Cooling below T_{CDW}=63K was achieved by using an

open flow helium device mounted onto the beamline and all measurements were performed at 20K.

Single crystal samples of $ZrTe_3$ and Ni_xZrTe_3 were coated in vacuum grease and mounted onto a goniometer using a microloop. The goniometer was then attached to the diffractometer and the sample positioned in the centre of rotation sitting directly in the path of both the X-ray beam and the Helium gas flow provided by the cryostat. Through the rotation of the sample and the CCD detector it was possible to map out large regions of reciprocal space of the Ni-intercalated series.

CrysalisPro was used to analyse the diffraction patterns and determine the space group and lattice parameters of the different member of the Ni-series. All Ni_xZrTe_3 indexed to the $P2_1/m$ space group, slight changes in the lattice parameters across the series were observed Fig.(4.7. Both the X58 and X60 samples showed a slight increase in their c-axis lattice parameter more in line with the published value for Ni_xZrTe_3 (x=0.05). The X62 sample was indexed with a c-axis lattice parameter close to that of the published value for pure $ZrTe_3$. These lattice parameters must also be put into the context of the poor crystalline quality of these samples with samples often formed of several crystallites making determination of the c-axis parameter difficult.

Pure $ZrTe_3$ develops a superstructure below T_{CDW} with a nesting vector q_{CDW}=(0.93a^*,0,0.33c^*). Given that this nesting vector is likely to be very similar in the Ni_xZrTe_3 series the data collection and analysis focused primarily on the ac-plane Fig.(4.8).

Due to the nesting vector and the close proximity of the superstructure to the main lattice peaks a balance between overexposure of the main lattice peaks required to observe the superstructure and preventing the intensity of the main lattice peaks from obscuring the superstructure intensity had to be

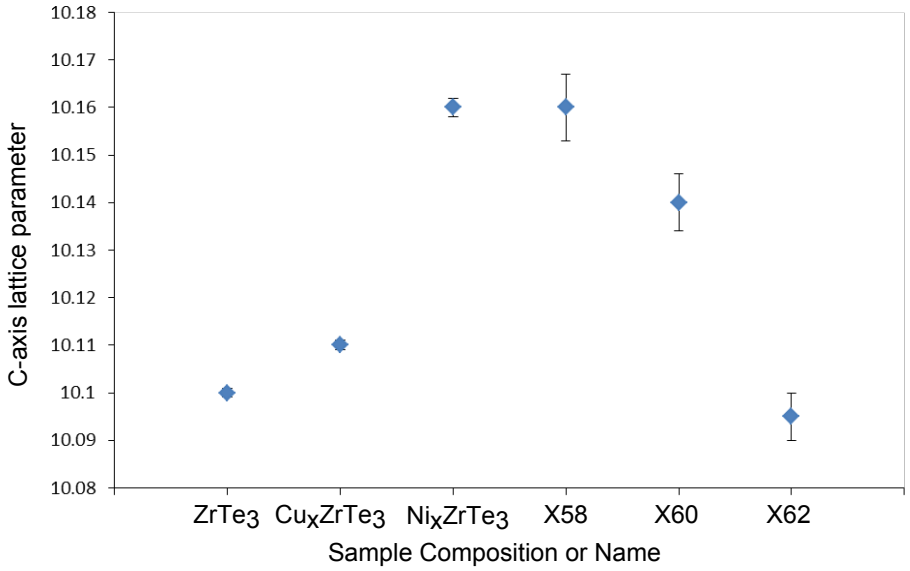

Figure 4.7: C-axis lattice parameters for the Ni_xZrTe_3series. Additional published values for $ZrTe_3$ [105], Ni_xZrTe_3 (x=0.05) [102] and Cu_xZrTe_3 (x=0.05) [103] have been included for comparison.

found.

In general across the whole series the superstructure reflections were weak in comparison to the main lattice reflections and were only visible adjacent to dominant Bragg reflections. The weak nature of the superstructure necessitated the overexposure of the main lattice reflections. As a result of this overexposure stray intensity from the main lattice reflections was present in the diffraction patterns in all of the samples measured. The stray intensity from the main lattice peaks often leaked into the superstructure reflections making the determination of the relative intensities of the superstructures between Ni_xZrTe_3 compounds unreliable.

Unfortunately due to this and the poor bulk crystalline properties of the Ni-series in general, possibly due to inhomogeneous distribution of the Ni between the ZrTe layers, only a limited analysis of the series was possible. An uneven distribution of Ni may have led to stacking faults between the ZrTe layers which is evident in the mosaicity observed in the diffraction patterns of the

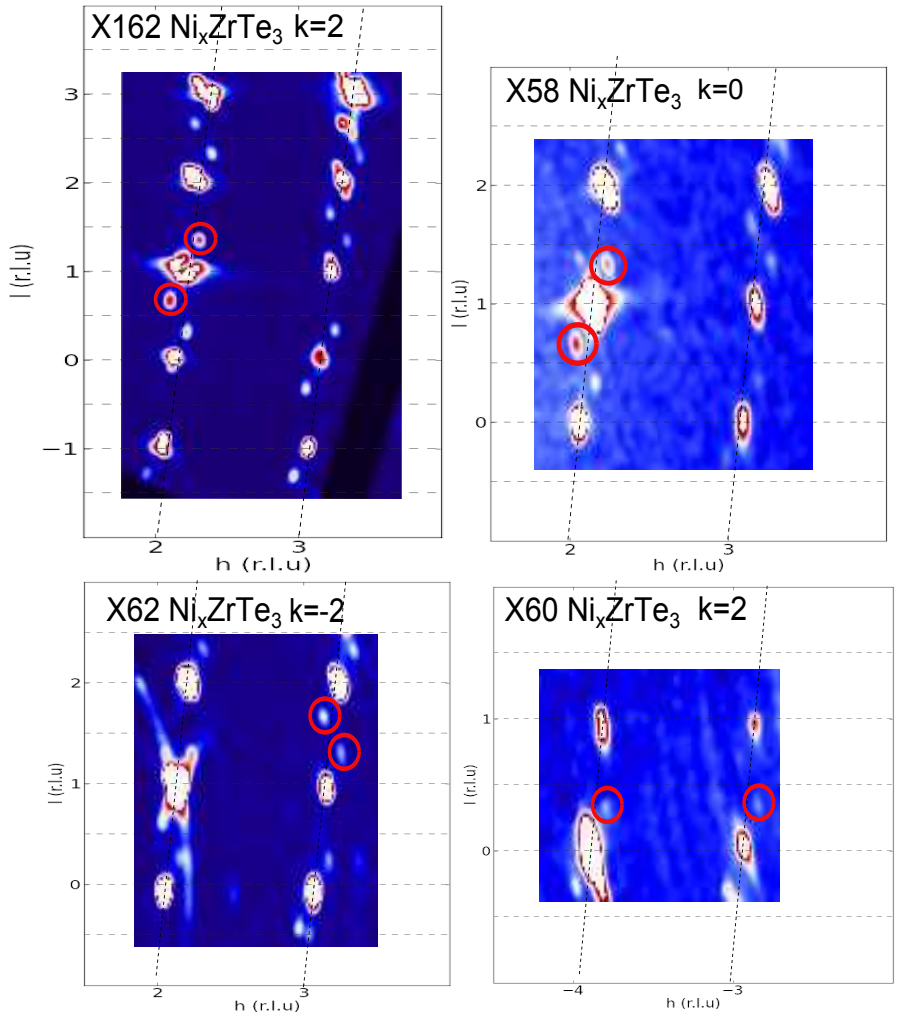

Figure 4.8: Diffraction for the Ni_xZrTe_3 series showing the superstructure in the hnl plane, where n is a constant, associated with the CDW formation

Ni_xZrTe_3 series Fig.(4.8).

Results from the ac-plane for the various Ni-intercalated compounds Fig.(4.8) all show the presence of a superstructure near dominant and overexposed main lattice peaks. In all cases the q_{CDW} was found to be approximately equal to that reported to be present in the pure compound i.e q_{CDW}=(0.93a^*,0,0.33c^*) Fig.(4.8). This superstructure is highlighted further in cuts at a constant m, where m=h+q_a and q_a is the a* component of q_{CDW} Fig.(4.9). In these mkl planes the superstructure is clearly visible at $\frac{1}{3}$ type positions along the c-axis.

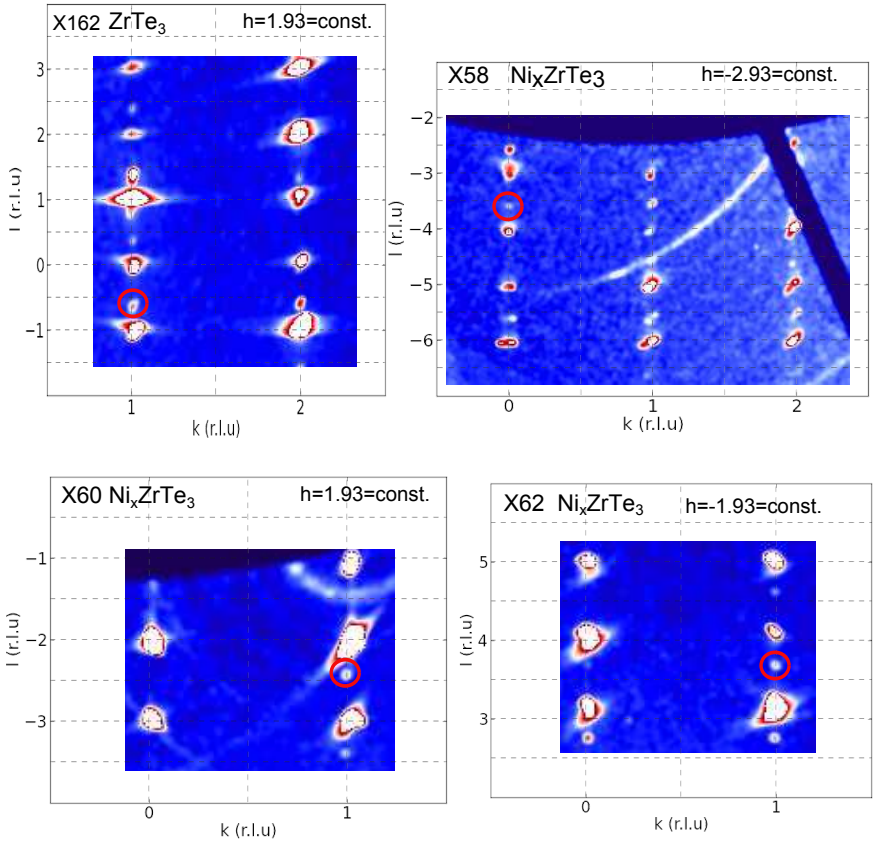

Figure 4.9: Diffraction for the Ni_xZrTe_3 series showing the superstructure in the mkl reciprocal lattice plane associated with the CDW formation.

The constant q_{CDW} across the series may be an indication that the shape of the quasi-one-dimensional sheet at the Fermi-surface remains unperturbed to within error across the Ni-intercalated series. However, despite possible changes to Fermi-surface, the (1/3) modulation may remain energetically favorable especially for small changes to $2k_f$. ARPES measurements presented later where no changes in the Fermi-surface shape were observed between samples support the idea that $2k_f$ remain unchanged. These conclusions however must be contextualized in terms of the quality of Ni_xZrTe_3 samples, as it was difficult to ascertain accurate values for q_{CDW}. It is possible that large regions of pure $ZrTe_3$ dominated the diffraction pattern and that the q_{CDW} observed in the diffraction patterns of the Ni_xZrTe_3 series was a result of this structure.

Future X-ray diffraction work

In general this diffraction study highlights the difficulties associated with measuring intercalated layered materials. It is highly likely that these materials will show some kind of disorder, due to stacking faults or inhomogeneity of Ni-content, making analysis of the resulting diffraction patterns difficult.

An alternative approach to data collection could also be used, whereby many smaller crystals were measured, reducing the likelihood of twining or lattice mismatches appearing in the diffraction pattern. Given that the superstructure has not been seen in lab-based measurements, such an experiment would have to be performed at a synchrotron source where experimental time is limited. In the case of such an experiment, focusing on a single Ni-concentration to produce a comparison to pure $ZrTe_3$ would perhaps be the best approach, rather than the measurement of a series of different Ni-concentrations.

Powder X-ray diffraction would eliminate the difficulties arising from twin-

ing etc and through refinement of the diffraction pattern could also provide information on q_{CDW}, however the weak nature of the superstructure means that measurements on smaller crystals and especially on powders may fail to observe the superstructure reflection.

Further temperature-dependent diffraction studies on higher crystalline quality Ni_xZrTe_3 would enable a comparison between the intensities of the superstructure reflections seen in the Ni_xZrTe_3 series. It would also be able to reliably determine any difference in the q_{CDW}.

4.5 Angle resolved photoemission spectroscopy

Photoemission is an extremely sensitive probe able to measure small changes in bandstructure and electron binding energy. It is a technique which is not sensitive to twinning in the bulk of crystals being measured. It is therefore an excellent technique with which to observe the effects of low-concentrations of Ni in Ni_xZrTe_3. In this work, the same four samples of Ni_xZrTe_3 described earlier were measured by ARPES. Data were taken on the ARPES instrument at the I05 beamline at the Diamond Light source which is described in Chapter 2. Measurements were focused in particular on the quasi-one-dimensional Fermi sheets, extending along the B(A) and D(E) direction, responsible for the Fermi-surface nesting in $ZrTe_3$ [17].

4.5.1 Samples preparation and measurement procedure

Samples of single crystal Ni_xZrTe_3 were prepared for ARPES using the top post method described in Chapter 2. These were orientated with the ab-plane, which is easily identifiable due their layered nature, normal to the surface Fig.(4.10).

Once in the ultra-high-vacuum of the upper-chamber of the ARPES instrument the top-post was removed using a wobble stick.

$ZrTe_3$ typically cleaves well due to the weak van der Waals force between layers and preferentially exposes the top of a single $ZrTe_3$ layer in the ab-plane. Knowledge of the orientation of the surface normal was useful when aligning the sample for ARPES measurements.

After moving the sample into the lower-chamber the sample surface was inspected visually to asses the quality of the cleave. To do this the sample was rotated in Θ under the illumination of lamp light whilst observing it using a camera focused on its position. Flat shiny areas of the surface suitable for ARPES measurements were identified. It was also possible at this point to identify any stray fibres as a result of the cleaving process.

During ARPES measurements fibres can interfere with measurements typically present as shadows on the the detector image. If fibres Fig.(4.10d) were seen and deemed to be problematic the sample was taken back into the upper-chamber and the fibres were removed/moved using the wobble-stick or if the sample was irredeemable it was transferred out and exchanged for a fresh sample.

The X-ray beam, with a typical spot size of 50x50μm, was focused onto the cleaved region of the sample surface. Previous measurements on $ZrTe_3$ have optimized the polarization and incident photon energy best used for mapping their Fermi-surface. As such linear horizontally polarised incident light with an energy of 70eV was used for the majority of measurements presented here and all data was taken at 7K well below T_{CDW}.

Scanning the sample across the incident X-ray beam and changing the photoemission conditions by rotating it in Θ, allowed the bandstructure i.e E vs K at different points on the sample surface to be observed on the detector.

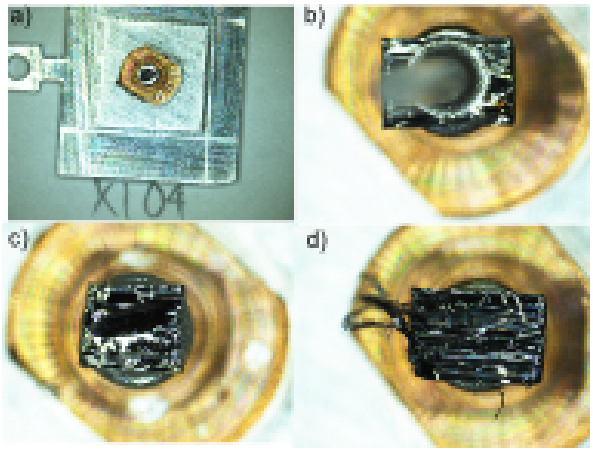

Figure 4.10: ARPES sample preparation. a) Sample mounted on the specially designed sample mount and in b) with the top-post attached. c) and d) show examples of cleaved samples. It is possible to identify a large flat surface suitable for ARPES measurements in c) whilst the surface in d) is more irregular and there are several fibres protruding from its surface.

It was then possible using the electronic bandstructure data to select the best area on the sample from which to take photoemission data.

Once a suitable sample surface had been selected, measurement of the bandstrucrture allowed the orientation of the sample to be determined. Using this information the sample was then correctly aligned with respect to the incident X-rays. After alignment of the sample, the Θ positions of the high-symmetry points (i.e the Γ,D(E) and B(A)-points) were established. Knowledge of the positions of the high-symmetry points and the Brillouin zone boundaries provided the information required for Fermi-surface maps over the 1^{st} Brillioun zone to be collected and the bandstructure at the high symmetry points to be measured.

The Fermi-surface of the material was mapped by varying the retardation potential on the analyser, to image photoelectrons with a range of kinetic energies, and rotating through Θ to access different parallel momentum states in the crystal.

Determination of the Fermi energy, E_f, was derived from the Fermi cut-off

of a gold block positioned above the sample on the manipulator arm.

Samples were checked for charging, where the emitted photoelectrons are not replenished, by observing any changes in the bandstrucure specifically any movement of E_f as the flux of incident photons was increased by increasing the size of the beam spot.

4.5.2 ARPES results

Initial measurements were made on the pure $ZrTe_3$ sample X162. The Fermi-surface map (FSM) of $ZrTe_3$ is shown in Fig.(4.3a). The Fermi-surface for $ZrTe_3$ agrees well with both the theoretical calculations and ARPES data found in the literature. The main features of the Fermi-surface described previously are visible. One can see the Fermi sheet surrounding the Γ-point and the increase in intensity expected at the B(A)-point. The quasi-one-dimensional Fermi sheet extending along the B(A)-D(E) direction is faint but can still be seen over an integration window of 25meV at the Fermi-surface. The lack of intensity at the Fermi-surface of the quasi-one-dimensional band is due to the depletion in spectral weight below T_{CDW}. An energy distribution cut (EDC) through the D(E)-point (indicated by the solid blue line on the FSM) clearly shows the electron-like band and the reduction of spectral-weight at the Fermi-surface. A temperature-dependent study of the D(E)-point spectra Fig.(4.11) shows the evolution of the spectral weight associated with this band as the sample transitions through T_{CDW}.

It can be seen that as temperature is lowered the spectral-weight is depleted at the Fermi-surface and shifts to a lower binding energy. Below T_{CDW} the line-shape of the EDC changes. The temperature dependence of the spectral weight at the D(E)-point is in agreement with published work [17].

An EDC (indicated by the solid blue line Fig.(4.3a))through the B(A)-

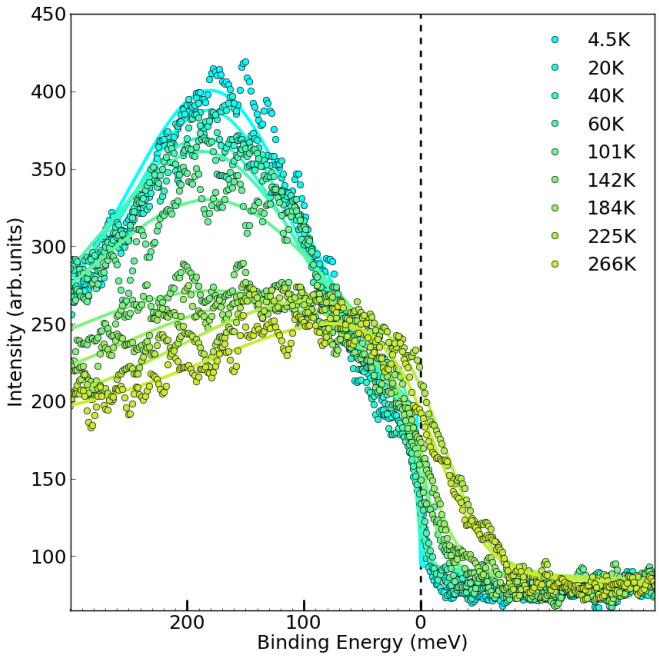

Figure 4.11: Temperature-dependent EDC integrated over several momenta about the D(E)-point of pure $ZrTe_3$. A change in line-shape is observed as temperature decreases below the T_{CDW} and spectral shifts away from the Fermi surface.

point shows the expected spectral weight at the Fermi-surface. Adjacent to the B(A)-point are the bands responsible for the feature surrounding the Γ-point seen in the Fermi surface map.

Fermi-surface maps of the Ni-series are shown in Fig.(4.12). The quasi-one dimensional sheets extending from the B(A) and the D(E) point are identifiable in all samples, although these are once again weak due to depletion of the spectral weight at the Fermi-surface. Also visible in all samples is the three-dimensional band surrounding the Γ-point and a strong spectral weight at the B(A) point which is absent at room temperature [17].

There are no immediately obvious differences between the shapes of the Fermi-surfaces of these compounds. There is however a significant difference in the quality of the cleaved surface being measured from. A poorer quality surface results in the blurring of the features observed in the bandstructure spectrum. In this set of data it is most notable when comparing the data from the pure $ZrTe_3$ Fig.(4.3) to that of the Ni-intercalated samples Fig.(4.12).

A charging effect was observed in X60, whereby there was a constant shift in the Fermi-level when normalized to the Fermi energy of crystalline gold. For the X60 Fermi-surface plot the charging observed in this sample required a larger energy window ΔE_f to be integrated over. Whilst the charging in the X60 sample is worth noting it appears as a constant offset across the data set which can be taken into account when performing the analysis of the key points at the Fermi surface.

The formation of the charge-density-wave in $ZrTe_3$ is known to involve nesting between the parallel sheets along between B(A)-D(E)-points. Suppression of the CDW through chemical pressure is expected to influence the one-dimensional Fermi sheet. As such EDCs integrated over a small k-range at both the D-point ($k_x = 0.8$) and a point along the Fermi sheet at $k_x = 0.2$

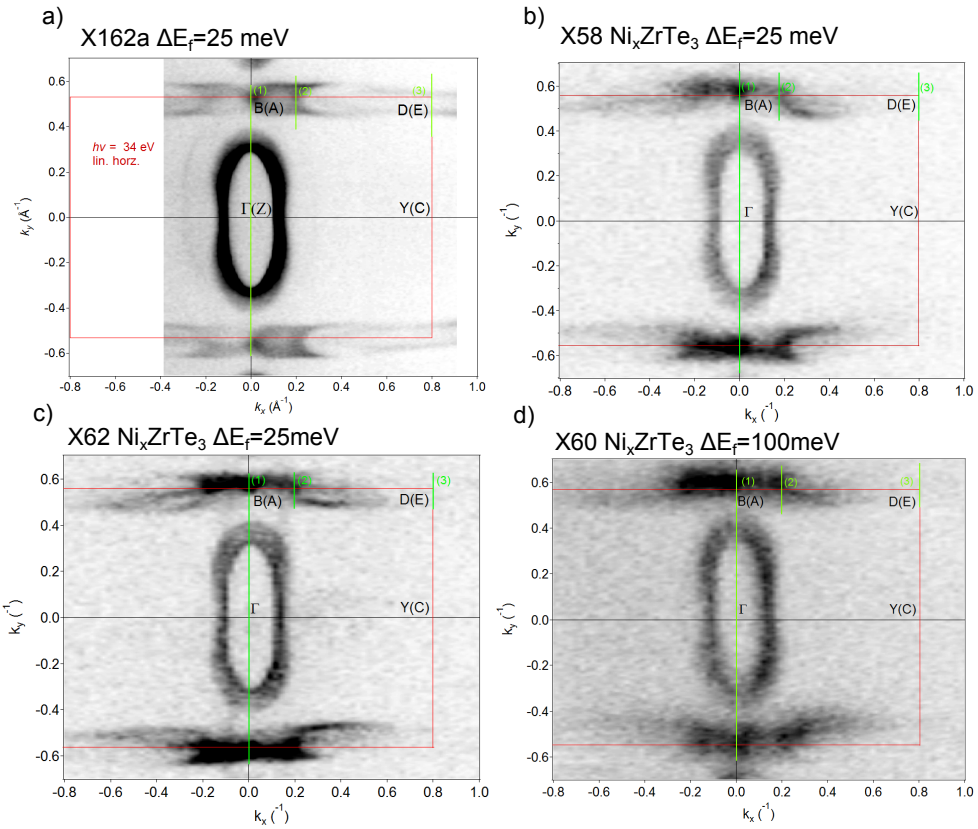

Figure 4.12: Fermi-surface maps of the Ni_xZrTe_3 series. a) pure $ZrTe_3$ taken with a photon energy of 34eV and b)-d) the Ni-intercalated series taken with a photon energy of 70ev. The Brillouin zone is indicated by a solid red line and the main symmetry points are labeled whilst the green lines indicate directions through which EDCs were taken.

Fig.(4.13e) and Fig.(4.13f) were produced.

The EDC at the D(E)-point was fitted using the product of a Lorentzian function and a Fermi-Dirac function. The value of the peak position was extracted from the Lorentzian fit and plotted as a function of sample number to probe the relationship of the chemical pressure with the formation of the CDW within the samples Fig.(4.14). The error bars were derived from the error in the least squares fitting of the convoluted Lorentzian and the Fermi-Dirac function at k_x=0.8 and k_x=0.2.

Due to the different line-shape of the EDCs taken at k_x=0.2 a different method of analysis was required; in this case the position of the left-edge of the spectral-weight near the Fermi-surface was used as a measure of the influence of the Ni-intercalation on the binding energy of the band. A similar shift to that seen at the D(E) was also observed in the EDC at $k_x = 0.2$ Fig.(4.14).

Other points of interest on the Fermi-surface of $ZrTe_3$ are the B(A) and Γ-point.

The spectra in Fig.(4.15) show a momentum cut across the Brilloioun zone from one B(A) point to the other indicated by cut(1) in the FSM Fig.(4.12). It is possible in this cut to identify the area of strong spectral weight sitting at the B(A) and the three-dimensional sheet that surrounds the Γ-point.

At the Γ-point an electron-like band is observed. No significant changes where observed to this band as a result of Ni-intercalation Fig.(4.15e). Similarly, no changes due to Ni-intercalation are observed in the binding energy of the feature at the B(A)-point Fig.(4.15e). The data shown for all samples in e) and f) were measured using a photon energy of 70eV and linearly polarised light .

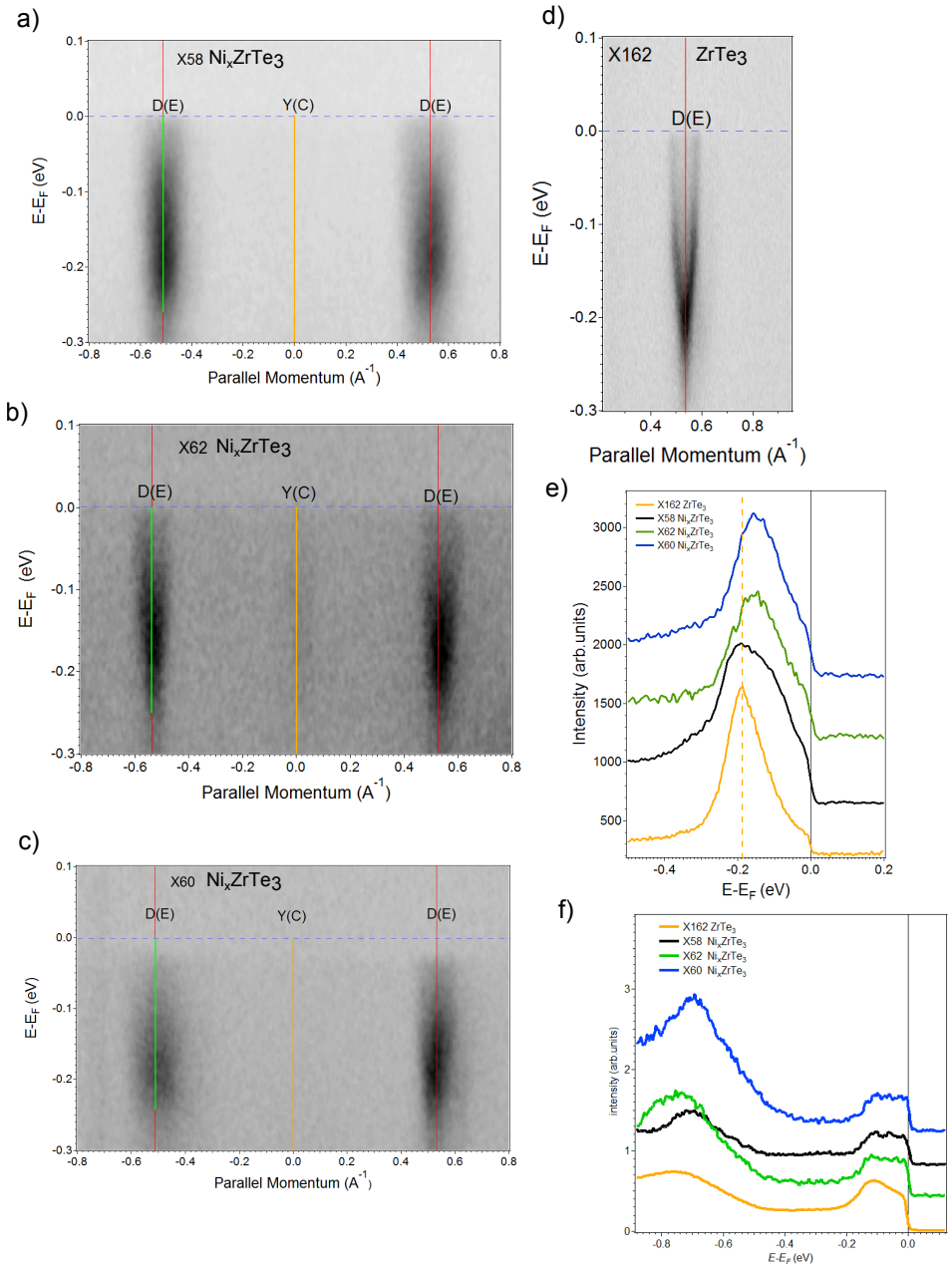

Figure 4.13: D(E)-point analysis of the Ni_xZrTe_3 series. a) to d) show cuts about the Brillioun zone boundary (red line) through the D(E) point (k_x=0.8) for the series of Ni-intercalated samples.e) EDCs through the D(E) showing the spectral weight shifted away from the Fermi surface (solid black line) forming an energy gap. f) EDCs for Ni_xZrTe_3 series taken at through the one-dimensional band at the k_x=0.2 momentum.The data shown for all samples in e) and f) was measured using a photon energy of 70eV and linearly polarised light.

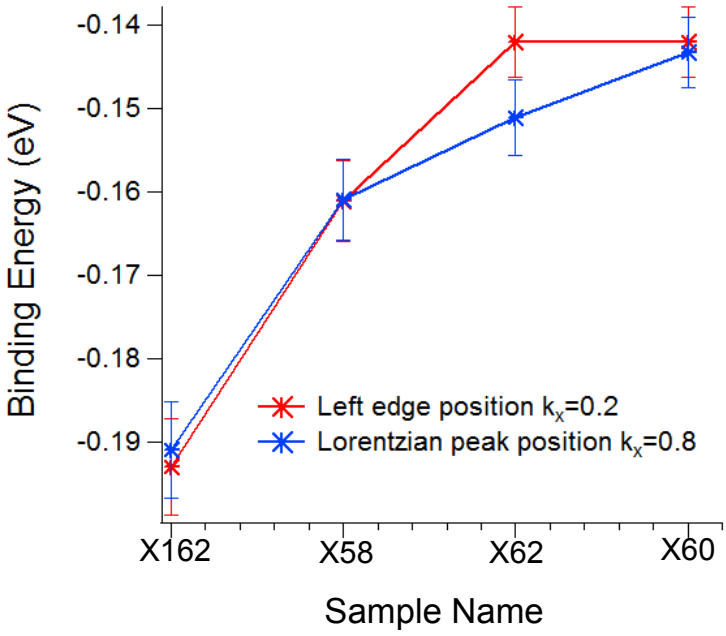

Figure 4.14: D(E)-point sample dependence. Peak positions of the spectral weight observed in the EDCs at (k_x=0.8) and (k_x=0.2) as a function sample name. All samples were measured using a photon energy of 70eV and linearly polarised light.

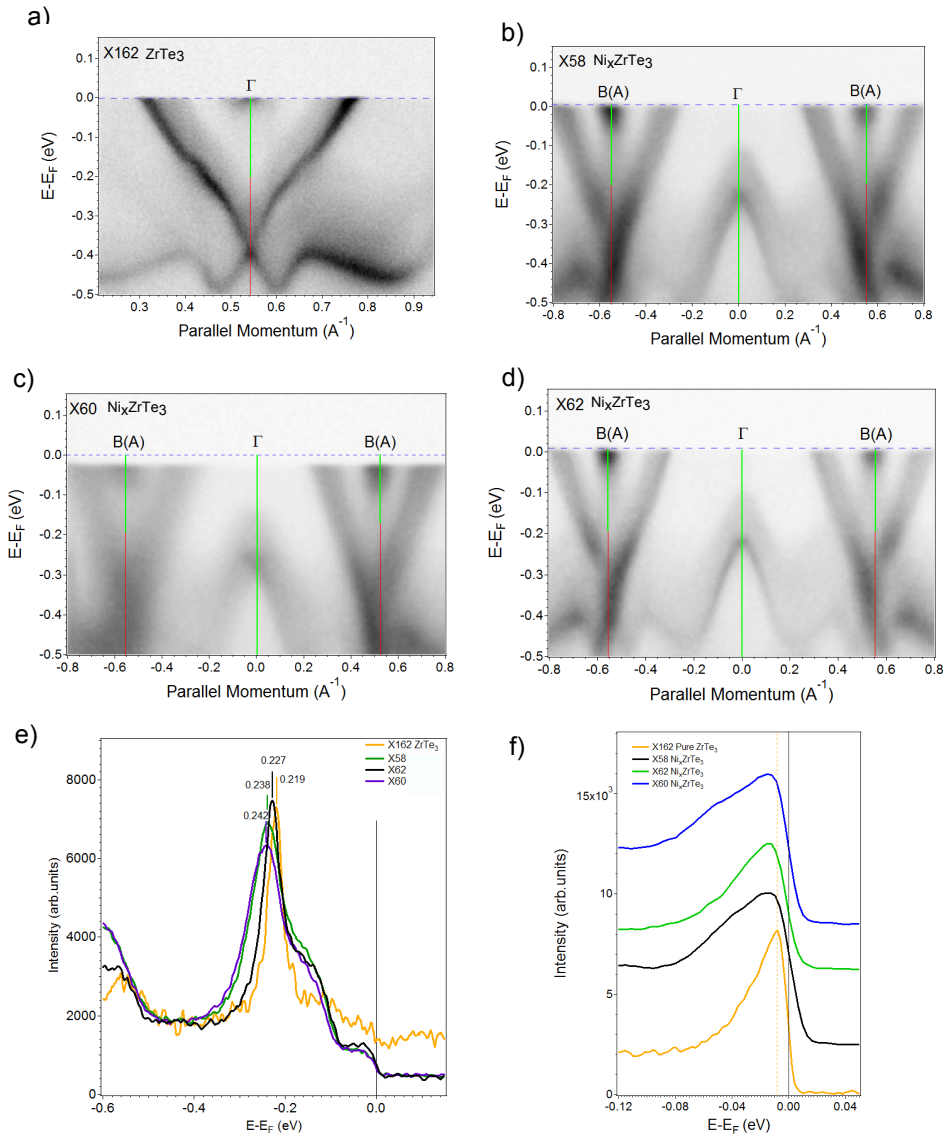

Figure 4.15: Γ and B(A)-point sample dependence. a)-d) Cuts along the B(A)-Γ-B(A) direction of the Ni-intercalated series of $ZrTe_3$.The Brillouin zones are shown as solid red lines, the dashed blue line is a guide for the eye and the solid green lines indicate directions along which EDC's were taken . e) An EDC integrated over a momenta window about the Γ-point, with the binding energy of the electron-like band labeled for each compound. f) EDCs for the Ni_xZrTe_3 series taken through the B(A)-point.

Conclusions and Future ARPES Work

Ni-intercalated $ZrTe_3$ was measured using ARPES and X-ray diffraction for several samples of unknown Ni concentrations.

Excellent quality high-resolution data was gathered from the pure $ZrTe_3$ sample. The Fermi-surface plot of $ZrTe_3$ highlights well the main features that dominate the electronic properties of these compounds. EDCs from pure $ZrTe_3$ at the D(E), B(A) and Γ-point show the unperturbed bandstructure.

Analysis of the bandstructure at the high-symmetry points along the quasi-one-dimensional Fermi sheet was performed. EDCs through k_x=0.2 and k_x=0.8 (the D(E)-point) across the quasi-one-dimensional Fermi sheet revealed a depletion in the spectral weight at the Fermi-surface for different members of the Ni-series consistent with CDW formation. A shift in the binding energy of the band at the D(E)-point is seen between the Ni_xZrTe_3 samples and the pure $ZrTe_3$. From work on pure $ZrTe_3$ it is known that the electron-like band at the D(E)-point is associated with the formation of a CDW. This association can be seen clearly in the bands temperature-dependent behavior through T_{CDW} Fig.(4.11). Decreases in the binding energy of this band Fig.(4.14) are an indication of a reduction of the occupation of this band as a result of Ni-intercalation. The largest effects are seen in the X62 and X60 samples whilst a smaller shift is seen in the X58 sample. Comparatively small increases in the binding energy of the hole-like band at Γ were observed and no shifts were seen at B(A)-point.

There are limitations to how far this analysis can be taken. The photoemission data from the three-Ni intercalated samples was of a lower quality with less well defined features than the data from $ZrTe_3$. In addition ARPES is a surface measurement technique and as such when cleaving an intercalated layered material it is entirely feasible that the exposed area is a Ni-poor re-

gion or Ni-rich area and the chemical pressure produced by the Ni in the bulk material is reduced or even absent in the surface layer.

Further work is required to determine the effects of chemical pressure on $ZrTe_3$. Theoretical calculations of the influence of different concentrations of Ni-intercalation would be helpful in interpreting and evaluating the changes seen at the D(E)-point in the ARPES measurements. ARPES measurements on higher Ni-concentrations would also be helpful evaluating the nature of the trend observed in Fig.(4.14).

The discrepancies between the bulk data and the data collected with ARPES highlight the need, when dealing with intercalated layered materials, to be mindful of exposing a surface which is unrepresentative of the bulk crystal. Future measurements on this series would benefit from focusing on a single known Ni concentration and performing multiple measurements from different surfaces from the same crystal or crystals in the same growth batch. This would allow a picture of an average surface to be constructed one which is not dependent on the cleaved region and is more representative of the crystal bulk. The Ni-concentrations could, in future, be determined using a number of more sensitive techniques such as powder X-ray diffraction refinement or cross-section scanning electron microscopy which would also allow the distribution of Ni across the crystal to be analysed.

Additionally, measurements on Cu-intercalated $ZrTe_3$ where the effects of the intercalated species have also be found to fully suppress the CDW would offer a useful comparison to the Ni_xZrTe_3 series and provide further information on the specific effects of chemical pressure on the bandstructure of $ZrTe_3$.

4.6 Outlook

ARPES and resistivity measurements on Ni_xZrTe_3 have both shown some effect of Ni-intercalation on $ZrTe_3$. These materials clearly offer great potential in studying the effects of chemical pressure on both the band-structure of pure $ZrTe_3$ and the interplay between CDW and superconductivity.

However, both the X-ray diffraction data and the ARPES data presented here highlight the difficulties associated with studying Ni_xZrTe_3 and in a wider context all intercalated layered materials. These measurements and the suggestions provided should inform and provide a reference for future studies on the Ni_xZrTe_3 compounds.

Chapter 5

Design and construction of a uni-axial straining device.

5.1 Introduction and Motivation

A vast amount of research in condensed matter physics is dedicated to the manipulation of novel physical phases (charge-ordered states, magnetic states, superconducting states, structural transitions) using a variety of control parameters such as electric or magnetic fields, temperature, pressure, strain and many more. Through the perturbations created by these control parameters one can alter the nature of, destroy or create phases within crystalline materials.

Amongst these different control parameters, there are those which directly change the lattice parameters of the material such as temperature, pressure and strain. Applying pressure or strain to a crystalline material allows for the continuous change of its lattice parameters without the convolution of the other thermal effects associated with temperature.

There exists many examples in the literature where tuning the lattice parameters of certain crystalline materials has revealed novel emergent phases [109, 110].

In the case of materials which exhibit a charge-density-wave state, strain and pressure have been shown to, in some cases, induce a phase transition resulting in the emergence of a superconducting state which would otherwise be absent under atmospheric conditions [101, 111].

X-ray synchrotron techniques provide an ideal probe with which to observe these emergent phenomena, be this through the observation of structural transitions, changes in electronic bandstructure, charge-ordered reflections or differences in lattice dynamics associated with certain electronic phases.

Currently the main techniques, hydrostatic pressurization, epitaxial growth onto a mismatched substrate or mechanical strain i.e bending, stretching,

shearing etc, used to perturb lattice parameters often preclude the use of a number of synchrotron based X-ray techniques.

Hydrostatic pressurization, whereby pressure is applied to a sample via a transmitting medium (argon or helium), is due to this medium unsuitable for use with certain X-ray techniques where the sample is housed in a vacuum chamber.

For example both ARPES and soft X-ray diffraction require ultra-high-vacuum, UHV, chambers to prevent atmospheric scattering of the experimental probes. The UHV in the case of ARPES prevents scattering of the emitted low-energy electrons and in the case of soft-X-ray scattering allows low energy photons to reach the sample and detector unattenuated.

Hydrostatic pressure is restricted to applying uniform pressure to a given sample and is unable to apply directional strain. Uni-axial strain is in some circumstances desirable as it can be used to perturb highly anisotropic crystals along specific crystallographic axes offering the possibility of increasing or decreasing the dimensionality of the crystal structure. Uni-axial strain could be particularly interesting in the context of the formation of density-waves which are known to rely on highly anisotropic Fermi-surfaces, the manipulation of which could lead to the suppression or promotion of the density-wave state.

Epitaxial growth is the other common method of applying strain to crystalline materials. Epitaxial growth can be used to induce a strain in a sample by growing the sample on a crystalline substrate with slightly different lattice parameters. The mismatch in lattice parameters between the substrate and sample results in a strain field in the grown compound. One of the major drawbacks of epitaxial growth is that lattice expansion or contraction achieved using epitaxial growth, whilst widely compatible with synchrotron techniques, does not provide dynamic strain. A series of samples each on slightly different

substrates would have to be grown to produce a strain phase diagram for a specific material. Epitaxial growth also relies on closely matching the films lattice parameters with that of a suitable substrate restricting the materials that can be strained using this method.

Mechanical methods have previously been successful in inducing dynamic strain in a wide variety of materials using many different measurement techniques. The devices used to apply the strain are extremely varied in their design ranging in complexity from those that apply strain by simply bending a beam with a sample soldered to its surface [112] to those that stretch or compress a sample using an arrangement of peiezoelectric elements [113]. Engineering beamlines such as the I12 beamline at the Diamond Light Sousrce or ID15 at the ESRF have used several different techniques to apply strain to materials on a larger scale where samples are typically of the mm^3 length scale. Whilst these beamlines have used a similar mechanical technique [114, 115] to that presented in this chapter i.e pulling on the sample to achieve a strain field the difference in sample size means that the devices employed by these beamlines are unsuitable for work with the smaller sized samples typically used in condensed matter physics. Mechanical methods perhaps offer the most versatile approach to the application of strain, in that apparatus can be custom designed to specific experimental techniques. However due to the mechanical approach other factors such as sample size, shape and stiffness play an important role in the strain experiments.

The majority of the mechanical devices reported in the literature have either been designed with the idea of performing resistance measurements on the strained sample or with a particular X-ray technique in mind. A straining device specifically designed for use with a range of X-ray synchrotron measurement techniques would be of great value.

In this chapter I present the design, construction and testing of a straining device designed to apply dynamic uni-axial strain to single crystal samples.

5.2 Design Goals and Restrictions

The main function of the straining device presented here is to induce controllable dynamic uni-axial strain in single crystal materials whilst remaining compatible with synchrotron measurement techniques.

X-ray measurements at synchrotron facilities place several restrictions on the design of the device. First and foremost it was important to consider the general geometries of synchrotron experiments, the most important consideration being to ensure that both the incident and scattered X-rays have unimpeded access to and from the sample under strain. In addition the size of the straining device was an important factor to consider. Certain X-ray beamlines, especially those involving UHV chambers, have tight constraints on the space allocated for additional experimental equipment. Given the limited space available it was vital that the straining device be as compact as possible. This provided the additional benefit of mobility, allowing the straining device to be transported and installed on synchrotron beamlines with relative ease.

In all synchrotron measurements access to the sample during X-ray measurements is prohibited and often even when not measuring the user has to go through an interlocking procedure to gain access to the sample environment. To improve the ease of use, the device was designed such that the magnitude of dynamic strain could be controlled remotely from the control cabin of the beamline. This remote control is of considerable benefit when the sample is placed in a UHV chamber as it prevents the need to break vacuum every time there is a need to change the magnitude of the uni-axial strain.

5.3 Design

To meet the criteria outlined above, a straining device based around two shear piezoelectric actuators was constructed. Piezoelectric actuators offer several advantages over other straining methods; they can be compact, there is no requirement for a pressure transmitting medium, samples can be exposed allowing access to the scattering probe and the strain can be controlled remotely.

The basic principle behind the device is that a sample is freely suspended between two shear piezoelectric actuators Fig.(5.1). These piezoelectric actuators are orientated in such a manner that, under a common voltage bias, they displace outwardly pulling on the ends of the attached sample and inducing a uni-axial strain within it. Suspension of the sample between the two actuators allows unimpeded access for the incident and scattered X-rays for a wide range of scattering geometries.

For the device presented here two Physik Instrumente P-141.10 shear piezoactuators were used [116]. These actuators are composed of stacks of 18 separate PZT piezoelectric ceramic elements (Lead Zirconate Titanate, PZT) sandwiched between two metal electrodes. The orientation of the PZT is such that on the application of a common voltage bias all of the elements in the stack displace in the same direction causing an overall shear displacement at the top of the actuator. The piezoelectric actuators provide shear displacements of up to $\pm 10 \mu m$ under a common voltage bias ranging from -250V to 250V. A suitable bias voltage was produced by a voltage amplifier (PI E413.00) used in conjunction with a $\pm$5V d.c voltage source.

On a 1mm size sample the displacements produced by the two actuators correspond to a strain on the order of approximately 1%. Given that strains of less than 1% have previously been sufficient to produce significant changes

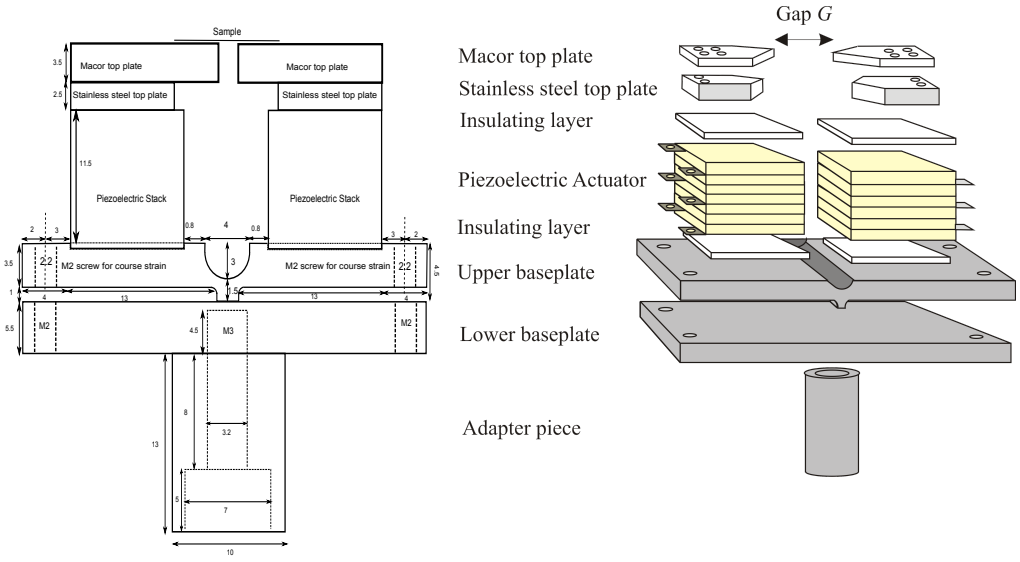

Figure 5.1: Straining device schematic. *Left*) Side on view of the straining device with the dimensions and components labeled. *Right*) 3D Visualization of the straining device with the components separated for clarity. Reprinted from Ref. [120] with the permission of AIP Publishing.`http://dx.doi.org/10.1063/1.4933383`

to various phases observed within crystalline samples [117–119] this geometry was considered reasonable.

Several adjustments and additions were made to the two piezoelectric actuators to incorporate them into the straining device Fig.(5.1).

Firstly, a suitable sample environment had to be created on the top of each of the stock PI shear piezoelectric actuators. The sample environment was designed with the purpose of providing a place where a single crystal could be easily secured to the piezoelectric stacks and remain viable with the constraints imposed by X-ray techniques.

The sample environment consisted of two top-plates, one stainless steel, and the other made from macor which is a ceramic material. The stainless steel top-plate acts as a permanent fixture for the macor top-plate, which is secured to the piezoelectric stack using an insulating epoxy glue (EPO-TEK H70E) and has two M1.6 threaded holes for the ceramic top-plate to bolt to.

On top of the stainless steel plate sits the macor top-plate which acts as the mounting point for the sample; which is fixed to the stainless steel top plate using M1.6 bolts via two M1.6 holes. Both the stainless steel and ceramic top-plate are tapered at the ends to allow for a large range of possible scattering geometries.

Samples are suspended between the two actuators by embedding the ends of the crystal in blobs of silver epoxy located at the tips of the ceramic top-plates Fig.(5.2). Silver epoxy and macor were both chosen so that if required resistance measurement could be performed concurrently with synchrotron experiments. If resistance measurements are not required other epoxies or clamping methods could be used to secure the sample to the ceramic top-plates.

The gap, G, Fig.(5.1) between the tips of the two ceramic top-plates is $\approx$1mm, samples should therefore ideally be needle shaped and 1-3mm in length and due to the uni-axial nature of the strain a few hundred microns thick. Larger single crystals can be cleaved or cut down to a suitable size. As previously mentioned G=1mm was selected so that strains of 1% could be generated in the mounted sample. However the dimensions of the macro top-plates can, if greater magnitudes of strain are required, be changed easily to reduce the gap-size.

Two additional M1.6 threaded holes in the ceramic top plate allow for a transfer piece to clamp to both the ceramic top-plates simultaneously Fig.(5.2). The transfer piece, a machined thin plate of stainless steel, is designed to enable the two top-plates to be removed from the straining device whilst keeping the distance between them fixed. Using a transfer piece, pre-glued samples can be quickly attached to the straining device and measured samples can be removed and preserved for additional experiments. This prevents the need to glue samples to the macor top-plates during synchrotron beamtime a process

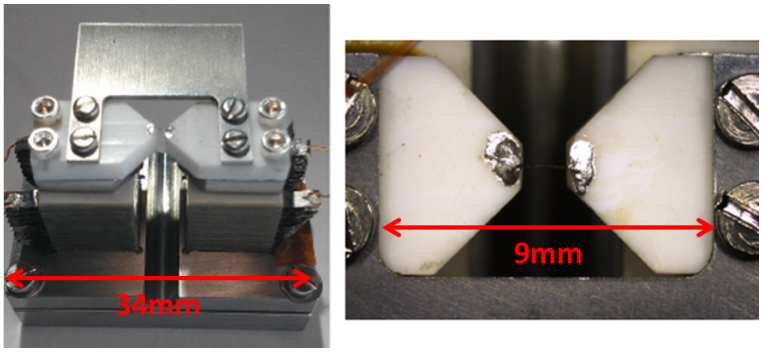

Figure 5.2: Straining device sample mounting. *Left*) Photograph of the complete straining device with the specially designed transfer piece attached to the macor top-plates. *Right*) A magnified view of the sample mounting technique shown here is a single crystal $Cs_2Mo_6Se_6$ sample, the ends of which are embedded firmly into silver epoxy located at the tips of the macor top-plates. Reprinted from Ref. [120] with the permission of AIP Publishing.`http://dx.doi.org/10.1063/1.4933383`

which takes ≈2 hours due to the curing time.

The two piezoelectric actuators were secured to a machined stainless steel baseplate using the insulating epoxy (EPO-TEK H70E). These actuators were orientated in such a manner that when a common voltage bias was applied to them they displace outwardly away from each other pulling on the sample suspended between them. Compressive strains can also be applied by reversing the polarity of the voltage source causing the tops of the piezoelectric actuators to displace towards each other reducing G.

The baseplate itself is split into two sections the upper and lower baseplates. The upper baseplate bolts to the lower baseplate using four M2 screws located at its corners, it also has a central fulcrum about which it is able to flex. As well as holding the two baseplates together, the four corner screws also provide an additional method of inducing strain in the sample. Tightening the corner bolts causes the upper baseplate to bend about the central pivot, increasing the distance between the two ceramic top plates and therefore straining any sample secured between them.

To mount onto a beamline an adapter piece can be attached to the lower baseplate using an M3 bolt. For the experiments presented in the upcoming sections the adapter piece was designed to fit onto a Huber 1005 goniometer. Different adapter pieces can be easily machined with the only constraint being an M3 through hole required to bolt it to the lower baseplate. The ability to easily change adapter pieces allows the straining device to be easily customized to meet the requirements of specific beamlines.

5.4 Initial testing and calibration

Prior to use on a synchrotron beamline the straining device was tested with the aim of calibrating the piezoelectric displacement to the applied bias voltage and also to ensure that the mounting in the silver epoxy was sufficient to produce a strain in given sample. To do this two experiments were performed, one looking at the change in resistance of a strain gauge under dynamic uniaxial strain and another using vibrometry measurements to assess the response of the actuators under different bias voltages.

5.4.1 Resistance measurements

Initially the straining device was tested by performing room temperature resistance measurements on a length of strain gauge wire. The material chosen for the strain gauge was a length of 70μm thick Constatan wire. Constatan is a nickel-copper alloy with a gauge factor, resistivity and high elongation factor that make it favorable for such an application. The strain gauge was secured between the piezoelectric actuators using a combination of insulating epoxy, acting as a mechanical hold, and silver epoxy for the electrical contacts. Once mounted the sample was mechanically pre-strained by tightening the screws

securing the plastic top plates to the actuators, pre-straining acted to remove kinks or bends in the wire that would otherwise reduce or eliminate the effect of piezoelectric displacement on the resistance of the sample

A four-probe method was used to measure the resistance of the sample and to eliminate contact resistances. Preliminary resistance measurements were performed using a Kiethley 2000 multimeter. These preliminary measurements established that strain was indeed being applied to the strain gauge wire. However, differences in the reaction to strain between constatan wire and single crystals made more detailed resistivity measurements unhelpful. Unlike the strain gauge wire, single crystals will contain defects and dislocations which may lead to inhomogenous strain fields in the sample. A superior method of establishing strain is through the use of X-ray diffraction. X-ray diffraction provides the local microscopic strain experienced by a crystalline sample by measuring directly the expansion of the lattice parameters along the strain axis. As such further efforts were not made to characterize the strain using the strain gauge wire and instead X-ray diffraction was used.

5.4.2 Displacement Calibration

Before assembling the straining device, the PI actuators were tested to measure and calibrate the displacement produced under an applied voltage using a laser interferometry technique. Such a technique allows the measurement of sub-micron sized displacements making it ideal for measuring the small displacements expected of the piezoelectric actuators.

The interferometry measurement used a Polytec Vibrometer, which recorded the Doppler shift of a back-scattered measurement laser with respect to a reference beam to determine the velocity or displacement of a reflective target. The reflective target for the measurement beam in the experiments presented here

was an $8mm^3$ aluminum cube, which was secured to the top of the piezoelectric actuator using quick drying varnish.

To reduce noise from background vibrations the actuator was mounted to an experimental stage bolted to an air-cushioned optics bench. This resolution was sufficient to measure the displacement produced by the PI actuators and to establish if the specification of a 10μm displacement over a voltage range of $\pm$250V was accurate. PI actuators 1(red) and 2(blue) were measured, using the Polytec Vibrometer, producing displacements of 9.8μm$\pm$100nm and 6μm$\pm$100nm over a voltage range of 250V respectively Fig.(5.3). The reduced displacement of PI actuator 2 is due to the exclusion of a pair of electrodes because of a short-circuit between them caused by an over-flow of solder. The calibration of the PI actuators Fig.(5.3) provided a conversion between displacement and applied voltage of 1μm$\pm$100nm per 50V for PI actuator 1, and in the case of PI actuator 2 (where a reduced displacement was observed) 1μm$\pm$100nm per 70V.

5.5 Test Material

The straining device was designed to apply dynamic uni-axial strain to single crystal samples. As such it was logical to select samples for testing which primarily display interesting anisotropic or low dimensional behaviors that can be perturbed through the application of strain. Additionally consideration must also be given to the materials stiffness, crystal quality and to the shape/size of the sample to ensure that the compound is a suitable candidate for straining.

One group of interesting anisotropic compounds are the molybdenum selenides $M_2Mo_6Se_6$ where M is an alkali metal (Cs, Rb, K, Na) or either In or Tl. These materials exhibit a quasi-one crystal dimensional structure

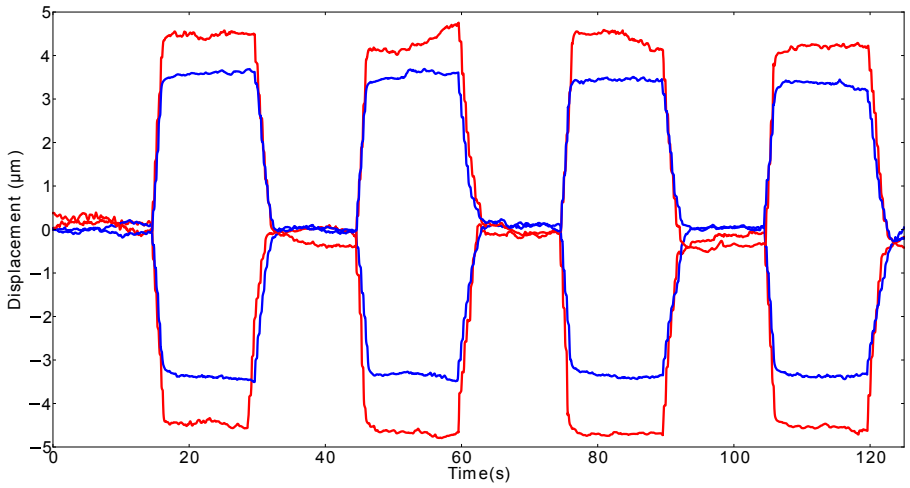

Figure 5.3: Displacement measurement of the PI piezoelectric actuators. PI piezoelectric actuators 1(red) and 2(blue) as the bias voltage applied to the stacks was periodically changed from 0 to +250V and a second trace showing the displacement as the bias voltage was periodically changed from 0 to -250V.

($P6_3/m$) [121] Fig.(5.4) consisting of hexagonally coordinated chains extending along the crystal c-axis of alternately stacked Mo_3Se_3 triangles rotated by 180^o with respect to each other. These chains exhibit strong intra-chain coupling but weak inter-chain coupling highlighted by large anisotropic behaviour [122] in both their magnetic [123] and electronic properties [124]. Sitting between the chains are the guest ions M. The choice of guest ion dictates the extent of the inter-chain coupling of the compound [125] and therefore strongly influences its electronic properties.

In the case where $M=$ In or Tl, $M_2\mathrm{Mo_6Se_6}$ remains metallic down to a superconducting transition temperature of 2-6.5K for Tl and 2.9K for In [126].

Interestingly uni-axial strain has previously [111] been reported to suppress the superconductivity found in samples with a Tl guest ion resulting in a metal to non-metal transition.

With an alkali metal as the guest ion the compound exhibits drastically

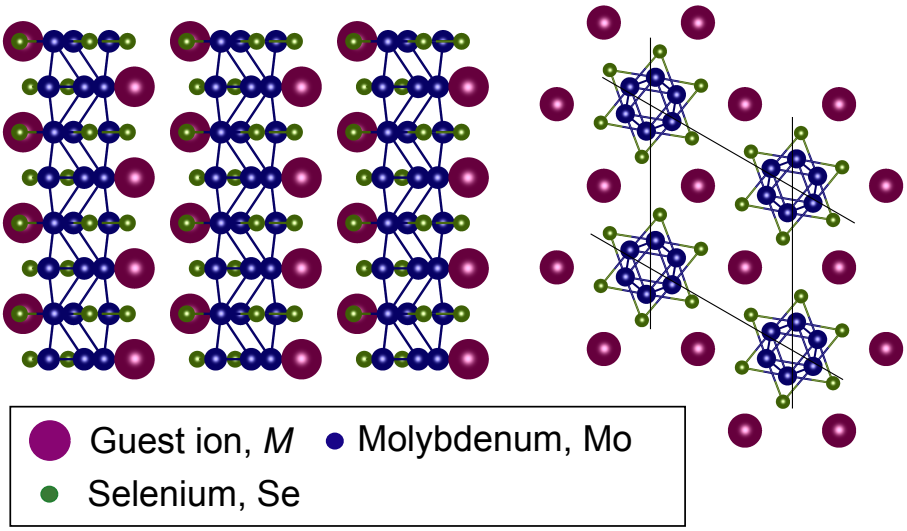

Figure 5.4: $M_2Mo_6Se_6$ crystal structure. Viewed along a) the crystal a-axis with chains perpendicular and b) along the chain-axis. Reprinted from Ref. [120] with the permission of AIP Publishing.`http://dx.doi.org/10.1063/1.4933383`

different properties. On cooling, between 200K-100K, a broad metal-insulator crossover is observed in the resistivity data that persists down to low temperature with no superconductivity observed [126].

Applying hydrostatic pressure to powder samples of $Rb_2Mo_6Se_6$ and $Cs_2Mo_6Se_6$ has been demonstrated to decrease the transition temperature of the broad metal-to-insulator cross-over [127]. Despite these highly anisotropic features and an extraordinarily one-dimensional sheet at the Fermi-surface no conclusive evidence has been found for formation of density-waves in these compounds.

In addition to the interesting anisotropy and pressure related behaviours the structural properties of $M_2Mo_6Se_6$ family also make them excellent candidates as a test material for the straining device presented here.

$M_2Mo_6Se_6$ forms into needle shaped crystals during growth reflecting its underlying chain structure, these needles are typically $\approx$ 1-2mm in length

with a diameter of $\approx 200\mu$m. The shape of the crystal is well suited to the application of uni-axial strain with a clearly identifiable c-axis and the needles are of a sufficient length that they can be firmly embedded in the epoxy glue whilst allowing for the distance between the macor top plates.

For the straining device to function efficiently the components of the device must be stiffer than the sample. This ensures that the displacement of the piezoelectric actuators is transmitted to the sample without loss. A detailed analysis of the stiffness of the straining device is performed in a later section.

Crystal inhomogeneity and defects can lead to structurally weak points in the crystal which when strained could lead to either an inhomogeneous strain across the crystal or reduce the breaking strain of the crystal. The samples presented here were pre-screened using lab X-ray diffraction to assess their crystal quality and checked during straining experiments for any inhomogeneity in the applied strain.

Mo_6Se_6 nanowires have been predicted to exhibit high breaking strains of greater than 8.2 % [128, 129]. However, experience straining these samples has shown that even the highest quality single crystals $M_2Mo_6Se_6$ break well before this limit along pre-existing cracks or defects. Despite these reservations about crystal quality and breaking strains significant levels of strain were able to be applied to the samples before their breaking strains were reached.

5.6 I16 X-ray diffraction

As highlighted previously, resistance measurements did not provide a quantitative measure of the efficiency of the straining device. To probe the magnitude of microscopic strains that the device was capable of an X-ray diffraction experiment was performed on the I16 beamline at the Diamond Light

source Fig.(5.5). Using the high resolution provided by this beamline the sub-Angstrom changes in lattice parameters associated with strains <1% were measured. An X-ray beam energy of 12keV and energy resolution of 1.7eV was used for all measurements. A PILATUS area detector was used for the measurements presented here, however, after discussions with colleagues the use of a point detector in conjunction with a graphite analyser crystal would be preferable in the future as this set-up would provide a superior Q-resolution.

5.6.1 Experimental method

To mount onto the diffractometer the straining device was attached to a Huber 1005 goniometer via a specifically machined adapter piece. The adapter piece was designed such that the sample position was at the correct height for the incident X-ray beam. With the X-ray beam incident on the sample it was rotated and aligned with the (004) Bragg peak on the detector. Once aligned the two piezoelectric actuators were then connected to a common voltage supply which was controlled from the beamline control cabin.

By measuring the position of the (004) Bragg peak as a function of applied voltage the efficiency of the straining device, defined as the transmission of piezoelectric displacement into sample strain, could be assessed.

For a given sample, the diffracted beam profile of the (004) peak was measured in incremental 10V steps from a zero voltage bias to an applied voltage of +250V. Each step corresponding to a displacement of the piezoelectric actuators of $\approx 400nm$.

Once the maximum range of the piezoelectric actuators had been reached, at a bias voltage of 250V, and the beam-profile measured the applied voltage was reduced back to zero. At this point the coarse strain screws were tightened slightly thereby changing the strain at 0V, the zero-point strain, and extending

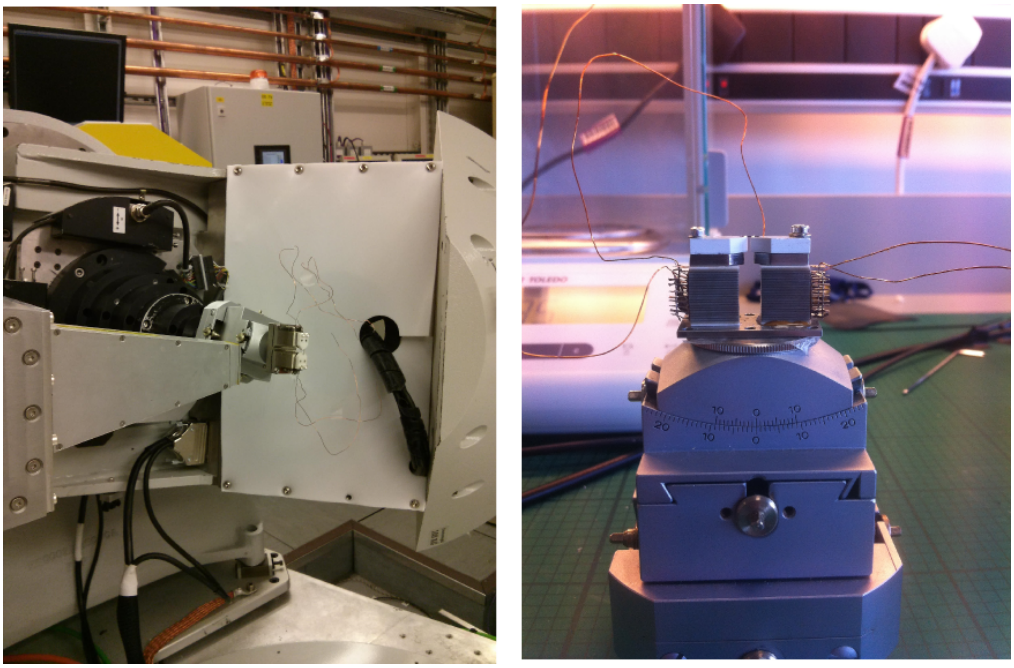

Figure 5.5: The I16 X-ray diffraction beamline at the Diamond Light Source. *Left*) The straining device mounted on the I16 diffractometer with the sample positioned in the path of the incident X-ray beam. *Right*) Photograph the straining device attached to a Huber 1005 goniometer.

the displacement range of the straining device. Once the zero-point strain had been adjusted the procedure of incrementally increasing the bias voltage and then tightening the coarse strain screws was repeated until the breaking point of the sample was reached.

In addition to measuring the peak profile at each discrete strain, the relative positions of the piezoelectric actuators was also measured. This measurement was performed by scanning the incident X-ray beam across the gap between the ceramic top plates Fig.(5.1) and observing the shadow produced by the ceramic top plates on a diode detector. As the beam was moved across the straining device the detector registered full intensity when passing through the gap and showed zero intensity when blocked by the top plates. By fitting to the intensity profile produced by this scan the positions of the ceramic top-plates relative to each other were recorded, providing a a value for the change

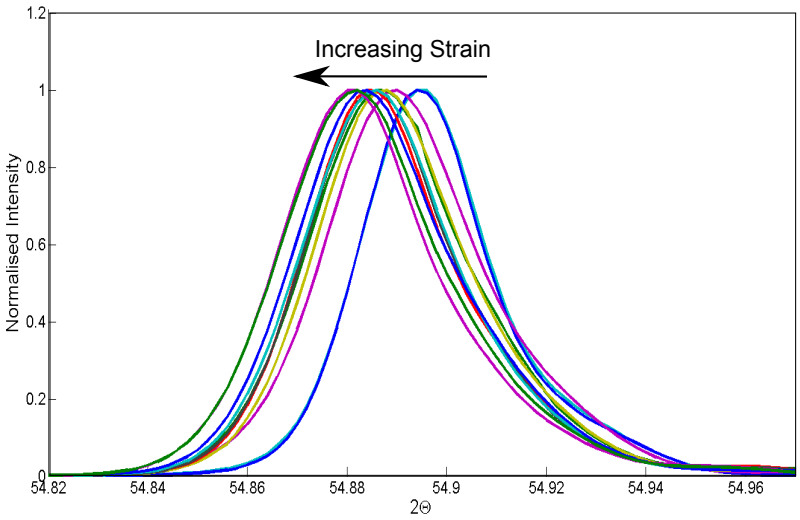

Figure 5.6: Strain measurements from $Cs_2Mo_6Se_6$.. Increasing the gap-size between the piezoelectric actuators induced a strain in the sample evidenced by a shift in the position of the (004) Bragg peak. For this sample no significant changes in the profile width were observed with increasing strain

in gap-size for each applied voltage bias.

5.6.2 Data Analysis

Fitting a Gaussian profile to the beam profile recorded at each bias voltage step allowed the position of the (004) Bragg peak to be determined and, via Braggs law, the lattice parameter associated with the straining direction to be calculated. A value for the microscopic strain ϵ,

$$\epsilon = (\frac{\Delta c}{c}) \cdot 100 \tag{5.1}$$

could then be calculated from the changes in the lattice parameter, Δc, and the known unstrained lattice parameter, c.

Strains of up 0.046%± 0.01% and 0.12%± 0.01% were achieved in samples of $K_2Mo_6Se_6$ and $Cs_2Mo_6Se_6$ respectively Fig.(5.7) [120]. Both samples show a linear response between the increasing gap-size and uni-axial strain. Variations

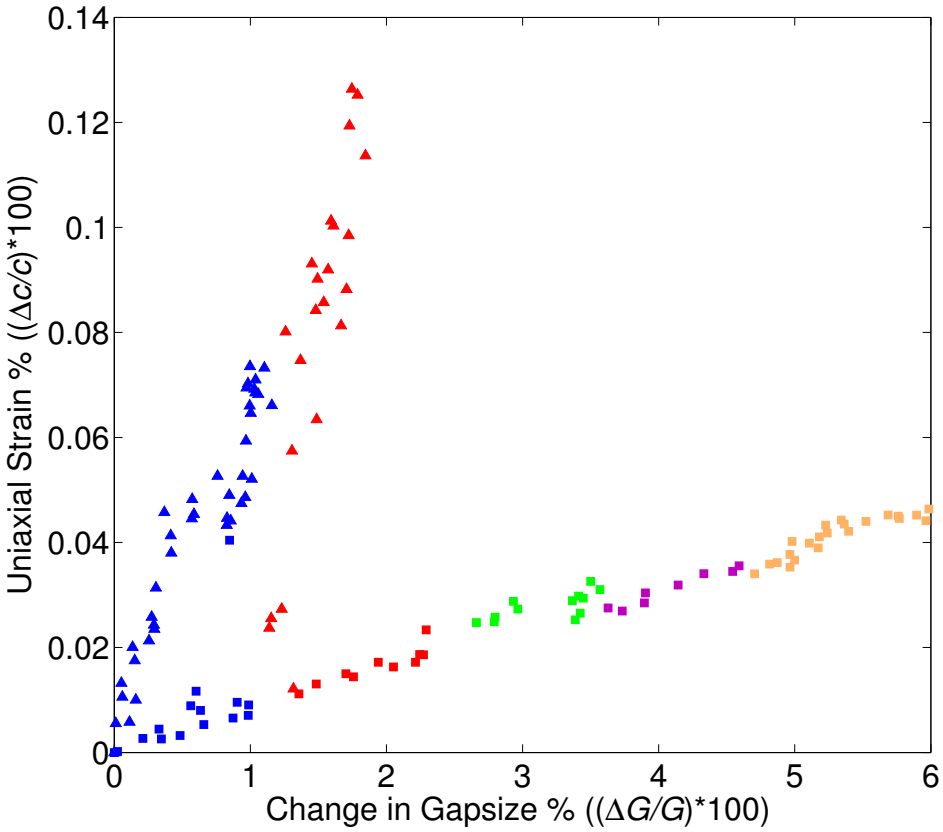

Figure 5.7: Strain measurements from $M_2Mo_6Se_6$. The two samples measured, $K_2Mo_6Se_6$ and $Cs_2Mo_6Se_6$, are represented by squares and triangles respectively whilst different colours are used to represent separate straining runs which are differentiated by the magnitude of zero-point strain. Reprinted from Ref. [120] with the permission of AIP Publishing.`http://dx.doi.org/10.1063/1.4933383`

in the gradient of this response can be attributed to the differences in both the geometries of the samples and the application of the epoxy glue between the two different measurements. The adjustment of the course strain screws can be seen to have functioned as expected Fig.(5.7) altering the zero-point strain each time the piezoelectric maximum displacement was reached and extending the straining range of the device [120].

Fig.(5.7) highlights the efficiency of the transmitted strain. Increasing the gap by 1% results in an increase in sample strain of ≈0.05% giving an efficiency of less than 10% [120]. There are a number of possible explanations for this inefficiency; i) either the stiffness of the sample exceeds that of the straining device and as strain is being applied to the crystal the device is flexing; ii) the stiffness of the epoxy glue is weaker than the crystals used in our experiment and is deforming as strain is applied or iii) the strain within the crystals is not uniform due to inhomogeneities in the sample.

Data from Fig.(5.7) rules out the possibility of the straining device flexing as it shows that the gap size is reaches its expected maximum displacement of ≈10μm given an initial gap size of 1.17mm. The macor top plates are therefore moving apart as intended. Had the sample stiffness been greater than that of the straining device a decrease from the expected value for G would have been observed. Also tightening the course strain screws resulted in an increase of strain in the mounted samples, if the sample stiffness did not exceed that of the straining device this would have instead resulted in flexing of the base plate. Both of these results indicate that the straining device is indeed stiffer than the sample and that the loss of transmission of strain is due to either the deformation of the epoxy glue or inhomogeneity in the measured crystal. To explore further the low-efficiency observed from the device a stiffness analysis of the straining device was performed.

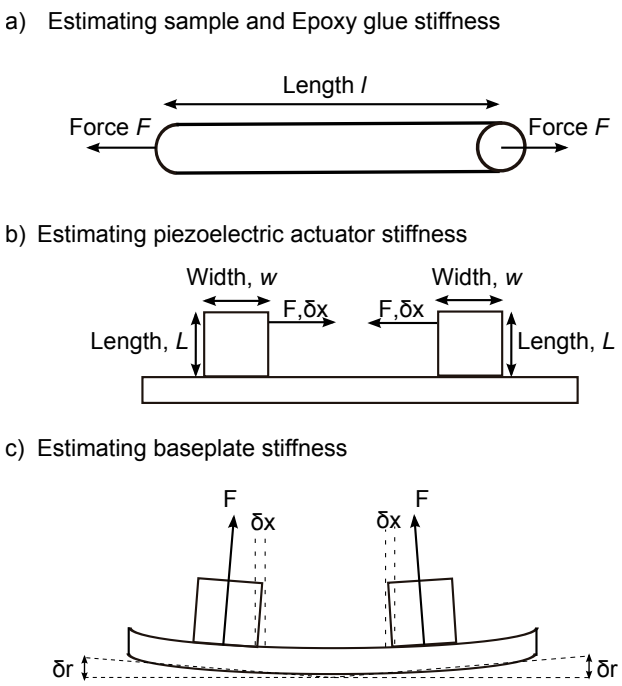

Figure 5.8: Geometrical models of the straining device components used to estimate their stiffness. a) the Epoxy glue and the sample, b) the piezoelectric actuators and c) the baseplate

5.7 Stiffness estimates

To evaluate the stiffness of the straining device it was separated into four components, the sample, the piezoelectric actuators, the baseplate, and the epoxy glue.

To estimate the stiffness of the sample, k_{sample}, and the epoxy glue, k_{epoxy}, they were both modeled as a rod of length l with cross-sectional area A and Young's modulus E allowing

$$k = \frac{F}{\delta x} = \frac{AE}{l}, \tag{5.2}$$

to be used Fig.(5.8a).

In the case of the sample the estimate of the the stiffness was k_{sample}=13$\pm$8.2Nμm^{-1} [120] using a value of 400GPa for the Young's modu-

lus [111]. Higher values of the Young's modulus have been predicted elsewhere 570GPa [128] but do not change the magnitude of the stiffness significantly. This is most likely to be an overestimation of k_{sample} as it assumes a perfect crystal. In reality even with pre-screening the crystal is likely to contain defects and dislocations resulting in several separate homogeneous crystalline regions within the sample. The effect of such a structure would be an inhomogeneous strain field across the sample and a reduction in the effective k_{sample}. X-ray diffraction measurements of the strain-axis lattice parameter at different points along the sample confirmed this hypothesis. Differences in the lattice parameter between these regions provided evidence for an inhomogeneous strain field [120].

For the epoxy glue the geometry of the problem was less well defined due to the fact the sample is embedded into blobs of epoxy glue making it more difficult to estimate the dimensions of the problem. The Young's modulus for a glue is also less well defined so as an estimate for E the storage modulus [130] was used. As such there is a larger uncertainty associated with the estimated value of k_{Epoxy}. Using these a value of k_{Epoxy}=4$\pm$3Nμm^{-1} was estimated using eq.(5.2) [120].

The piezoelectric stacks were known to have a high shear stiffness of [131] $k_{piezoshear}$= 100$N\mu$m^{-1} [120] which is much larger than that of the test sample. However consideration must also be given to their bending stiffness, as the actuators are expected to flex in response to the load placed on them by the sample. This situation can be modeled as a cantilever with stiffness

$$k_{cantilever} = \frac{Ewt^3}{4L^3}, \tag{5.3}$$

where the L is the length, w is the width,t is the thickness and E_{canti}

is the Young's modulus of the cantilever Fig.(5.8b). This produces a value of $k_{bendpiezo}$=22μm^{-1} for a single piezoelectric stack. In the geometry of the straining device where two stacks have been used in conjunction, the stiffness for the pair in total is half this value, k_{piezo}=11μm^{-1} [120].

Evaluating the stiffness of the twin baseplate was, due to their geometry, more difficult. To simplify the problem the baseplate was to be taken a single beam and any effects due to the central fulcrum were neglected [120]. When strain is applied to the crystal a force is exerted onto the baseplate by the two piezoelectric stacks, these forces cause the beam to flex about its central point resulting in a lateral displacement, δx, of the tops of the piezoelectric actuators and a reduction in G Fig.(5.8c). The flex of the baseplate can be calculated using the equation for beam deflection,

$$R = \frac{IE}{M}, \tag{5.4}$$

where the curvature of the beam R is dependent on the bending moment M it experiences from the load (in this case the piezoelectric stacks), the Young's modulus of the material, E, and the moment of inertia of the baseplate, I, which is solely dependent on the beams geometry. From the resulting change in curvature it is possible to calculate, through simple trigonometry, the displacement δx at the top of the actuator from the displacement δr at the ends of the beam. This displacement δx can be converted into a stiffness using eq.5.2 to get $k_{baseplate}$ 16$\pm$6Nμm^{-1} [120]. Due to the simplifications made about the baseplate this is most likely an underestimate of the actual value of the baseplate stiffness.

In conclusion the estimates of the straining device stiffness reveal that k_{piezo}, $k_{baseplate}$, and k_{sample} are all similar in magnitude whilst k_{Epoxy} is smaller. These

estimates suggest that the straining device is not stiffer than the crystal. However the estimates for $k_{baseplate}$ is an underestimation whilst k_{sample} is thought to be an overestimate. Experimentally it has been demonstrated that the gap-size reaches its expected value at the maximum applied voltage and that tightening the course-strain screws at the corners of the baseplate induces a strain in the sample. Given this experimental evidence it must be the case that the straining device is indeed stiffer than the sample. The lack of transmission of displacement to strain Fig.(5.7) can therefore be linked to the stiffness of the epoxy glue or to inhomogeneities in the crystal structure of the samples or a combination of the two.

5.8 ID28 Inelastic X-ray scattering

Having established that the device was capable of producing uni-axial strain in a material it was important to determine if the induced strains were capable of perturbing the physical properties of a given sample. As such an IXS investigation into the effect of strain on the phonon modes in $K_2Mo_6Se_6$ was performed. Specifically looking at the change of the speed of sound along the strain-axis direction as a function of the applied strain.

Although electronic measurements under strain seem to be the obvious choice for testing purposes, it is important to consider the additional testing benefits provided by an IXS experiment; i) the straining device is primarily designed for synchrotron based techniques and an IXS experiment allows the device to be tested in an additional beamline environment, ii) IXS directly probes atomic position directly related to the strain-axis expansion but has differing experimental criteria to that of diffraction and, iii) IXS measurements involve long counting times allowing the stability of the device to be tested.

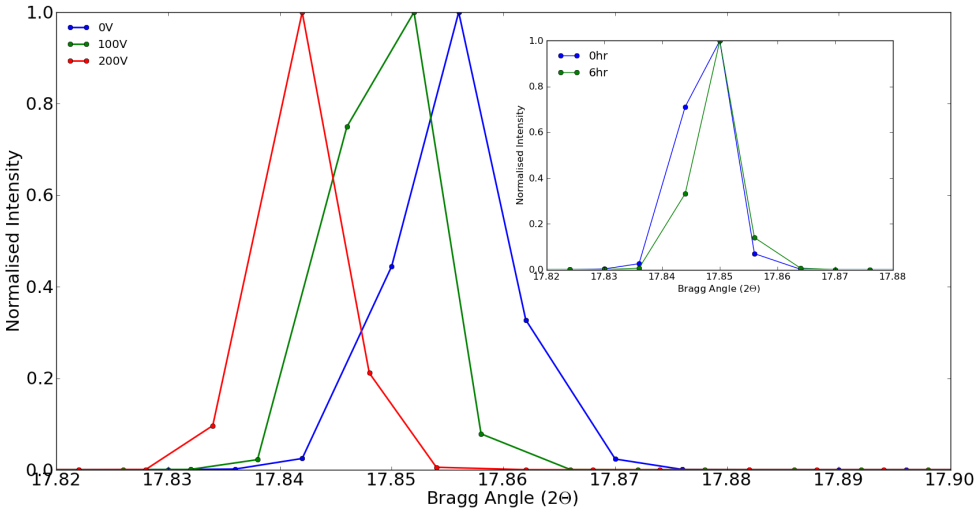

Figure 5.9: Strain measurements from $Cs_2Mo_6Se_6$. Increasing the gap-size between the piezoelectric actuators induced a strain in the sample evidenced by a shift in the position of the (002) Bragg peak. The inset shows the Bragg peak position with a 100V bias voltage applied to the straining device at the start of the IXS experiment (0hrs) and at the end of the experiment ($\approx$ 6hrs)

5.8.1 Experimental procedure

IXS measurements were performed at the ID28 beamline at the ESRF on a sample of $K_2Mo_6Se_6$. An incident X-ray beam with energy of 17.79keV, energy resolution of 3.2meV and spot size of $\approx$(250x80)μm was used for the measurements presented here.

The straining device with sample attached were secured to a Huber1005 goniometer using an adapter piece and the goniometer was mounted onto the beamline diffractometer. Once mounted, the sample was positioned in the centre of the incident beam with the straining axis (the c-axis) in the scattering plane. Alignment of the sample to the (002) Bragg peak was performed by using the beamline as a diffractometer and measuring the beam profile of the elastically scattered peak. A process which was repeated for each increase in bias voltage. Remeasuring the beam-profile and therefore the 2Θ position

of the (002) reflection in this manner allowed the c-axis lattice parameter to be calculated as a function of bias voltage. The beam profile of the (002) main diffraction peak was also measured at periodic intervals at the beginning and the end of a measurement to ensure that the strain had remained stable throughout the experiment Fig.(5.9).

For each bias voltage energy spectra at specific momentum transfers along the $\mathbf{Q}$=(002)+(00l) longitudinal direction were collected. To calculate the longitudinal speed of sound through the material only measurement of the low-$\mathbf{q}$ acoustic phonon modes was required, as such l was limited to 0.05,0.075 and 0.1 Fig.(5.10). In terms of the crystal structure this direction corresponds to the direction along the Mo_3Se_3 chains hence it is referred to as the longitudinal direction.

5.8.2 Data analysis

To determine the energy of the excitations at each momentum point, the energy-spectra were fitted using N Lorentzians, where N is the number of observed phonon modes functions Fig.(5.10). The Lorentzian functions were convoluted with a Pseudo-Voigt function defined by the instrumental resolution and the N fits were constrained by controlling the initial peak width and peak position parameters for the fitted Lorentzian functions. Using the fitted data dispersion curves could then be mapped out by using the extracted energy of the phonon modes.

The longitudinal speed of sound, ν, through the material was obtained from the gradient of a linear fit through the low-momentum low-energy phonon modes of the dispersion. Repeating these measurements for a number of different strains, allowed the relationship between applied strain and longitudinal speed of sound for $K_2Mo_6Se_6$ to be obtained 5.12.

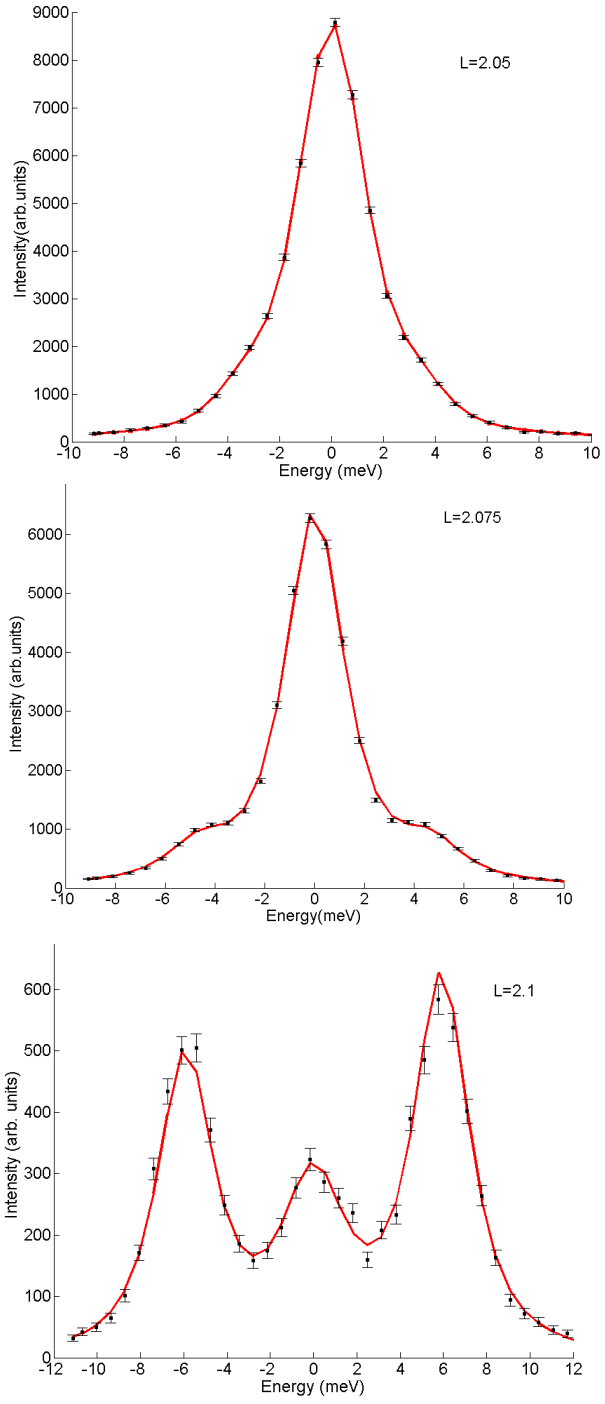

Figure 5.10: IXS phonon spectra for $K_2Mo_6Se_6$. a)-c) Fitted Phonon spectra for $\mathbf{Q} = (\mathbf{00l})$ from which the energy of the acoustic phonon mode was extracted for use in determining the longitudinal speed of sound with an offset correction applied to account for the non-zero value of the central elastic peak.

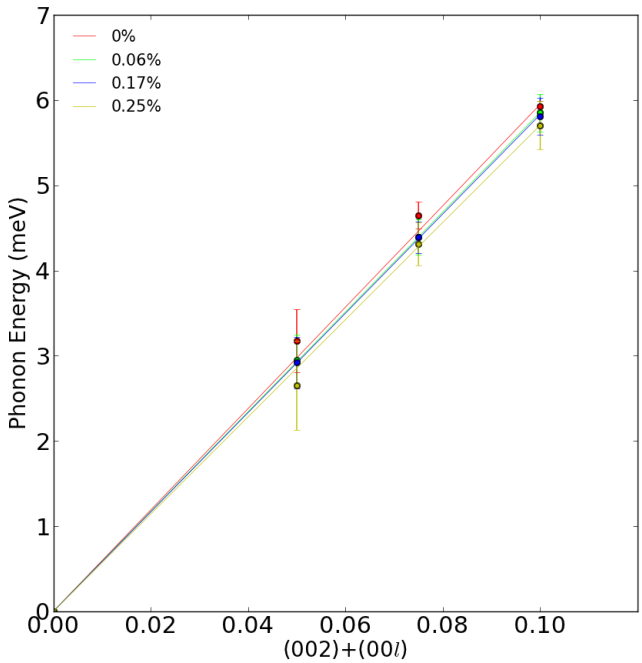

Figure 5.11: Linear fits of the low-q phonon measurements of $K_2Mo_6Se_6$ at different magnitudes of strain. The gradient of the fits gives the the longitudinal speed of sound through the crystal. Reprinted from Ref. [120] with the permission of AIP Publishing.`http://dx.doi.org/10.1063/1.4933383`

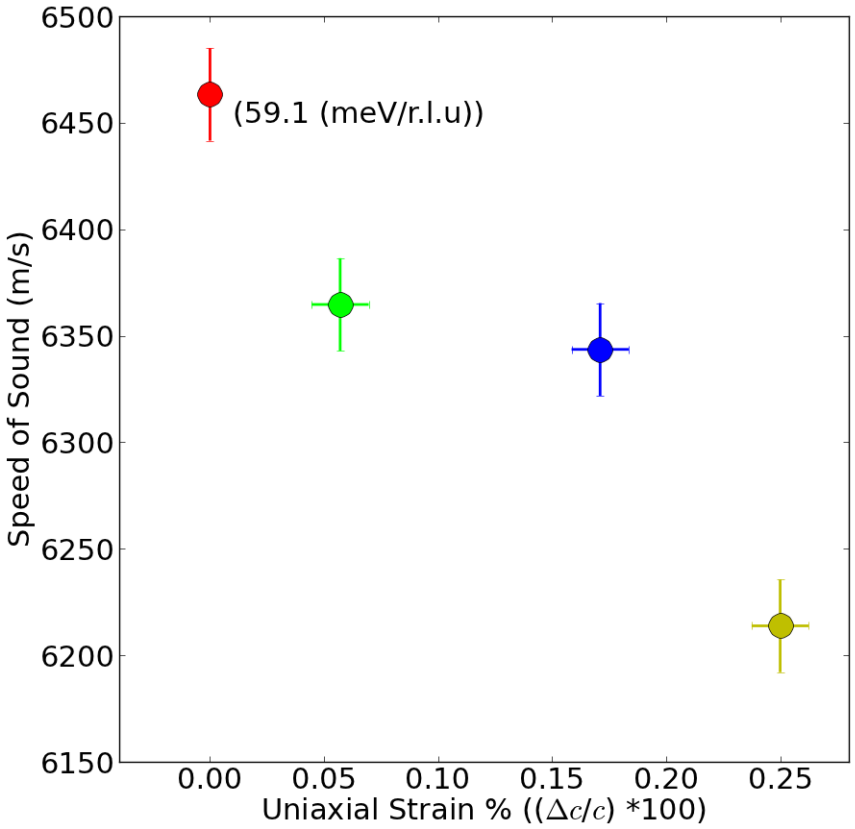

Figure 5.12: Longitudinal speed of sound in $K_2Mo_6Se_6$ as a function of strain. The speed of sound was derived from the low-**q** phonon measurements of $K_2Mo_6Se_6$ at different magnitudes of stain. Reprinted from Ref. [120] with the permission of AIP Publishing..`http://dx.doi.org/10.1063/1.4933383`

A decrease of $\frac{\Delta\nu}{\nu} = -3.8\% \pm 0.7\%$ in the longitudinal speed of sound was observed at a uni-axial strain of $\frac{\Delta c}{c} = 0.25\%$ [120] demonstrating that the strain produced by the device has a quantifiable effect on the dynamic properties of the crystal lattice.

5.9 Conclusions and Outlook

A uni-axial straining device for use in X-ray synchrotron experiments has been successfully constructed and tested. It has produced microscopic strains of up to $\frac{\Delta c}{c} = 0.25\%$ in the test material $M_2Mo_6Se_6$ [120]. The straining device was shown to be compatible with two different X-ray techniques (diffraction and IXS) and two different synchrotron beamlines (I16 and ID28). IXS measurements showed the strain produced by the device sufficient to influence the physical properties of $K_2Mo_6Se_6$, in this case the lattice dynamics in the form of a reduction in the longitudinal speed of sound.

Both the IXS and diffraction experiments showed the device to be reliable with the produced strains being reproducible and stable for a given sample over the course of these experiments.

During the X-ray experiments only pulling strain was applied to the sample. By applying compressive strain also, the strain range of the device could be effectively doubled. Compressive strains can be achieved simply by changing the polarity of the voltage bias to the piezoelectric actuators, causing them to displace towards each other. This was avoided for the experiments presented here for fear of samples buckling under the compressive strains, following discussion with colleagues who have designed similar piezoelectric devices, this was a misconception and compressive strains should not present any difficulties for these sample geometries.

All of the data presented here were performed at room temperature, however the straining device has been designed with the expectations of low temperature measurements. These measurements could be achieved by using a flow cryostat or by thermally coupling to the sample. A decrease of the piezoelectric performance is expected as temperature is decreased. Similar piezoactuators have shown a decrease of $\approx$ a factor of 4 at a temperature of 20K [132]. However, improvements to the sample mounting, baseplate design and the addition of compressive strain should be more than sufficient to counter-act this. Higher temperatures are also possible with the straining device provided that they do not exceed the Curie temperature (400K) of the piezoelectric ceramics used in the actuators.

Whilst the X-ray diffraction experiment showed that the straining device was stiffer than the test sample several improvements could be made to increase the stiffness of the straining device. Increasing the thickness of the baseplate and reducing the height or increasing the width of the piezoelectric actuators would increase $k_{baseplate}$ and k_{piezo} respectively. Improvements too could be made to the method used to mount the single crystal onto the straining device. This could be in the form of a stiffer epoxy or using a clamp to mechanically secure the sample to the macor top plate [113, 133]. As the stiffness analysis revealed the epoxy glue to be weaker than the sample this may lead to an increase in the efficiency of the straining device.

Additional ease of use improvements could be made to the baseplate design. The four course strain screw method although easy to manufacture may not be the easiest or best method for introducing a uniform uni-axial strain. An alternative baseplate design whereby the uni-axial strain is manipulated by a single screw which causes the piezoelectric actuators to separate increasing G may be preferable. Difficulties arise from this method in ensuring that the

screw has a high enough pitch to ensure only small movements of the piezo stacks and is strong enough to hold the device together.

Although the straining device is currently capable of operating in UHV further miniaturization would allow it to be used in smaller vacuum chambers. This miniaturization can be easily envisaged through the use of smaller piezoactuators. Although this would lead to a reduction in the maximum displacement of the device the improvements suggested to sample mounting could counter-act this. In addition a smaller device could be designed with shorter samples in mind, reducing the number of dislocations and defects present in the crystal and improving the homogeneity of the strain field through the sample. However it is important to keep in mind, when reducing the size of the device, the scattering geometries and beam sizes of X-ray techniques. One must make make sure that any reduction in size does not cause the straining device to violate these constraints.

In summary the straining device presented in this chapter enables a range of X-ray measurements on strained samples to be performed. This work opens up the possibility of dynamically exploring pressure-induced phases which until now were unable to be probed using certain X-ray techniques. It is of particular interest to those materials such as the $M_2Mo_6Se_6$ which have quasi-one-dimensional and quasi-two-dimensional crystals structures. In future the device may be used as a means of the manipulating DW materials into superconducting states with a specific focus on the effects of the directionality of the applied strain compared to the uniform strains achieved with hydrostatic pressure.

This work has been accepted for publication in Review of Scientific Instruments Ref. [120].

Chapter 6

Conclusions and Outlook.

In this thesis I have investigated quasi-one and two-dimensional crystalline metals which exhibit density-wave instabilities due to strong electronic correlations. I have used several X-ray synchrotron techniques to reveal and characterize the charge-density-waves found in these materials. I have also investigated two potential methods for perturbing the formation of charge-density-waves in low-dimensional crystal systems. The first of these methods was the use of Ni-intercalation in $ZrTe_3$ to exert chemical pressure within the crystal structure. The second was application of strain, and I have presented the results from the construction and characterization of a novel straining device. The straining device was designed to be compatible with a number of X-ray techniques and to deliver dynamic uni-axial strain to single crystal samples. Here I give a summary of these results, place them into the wider context of their field and provide suggestions for future work that this thesis has made possible.

6.0.1 $Na_2Ti_2As_2O$ and $Na_2Ti_2Sb_2O$

In Chapter 3 I presented X-ray diffraction data on two members of the quasi-two-dimensional Ti-based-oxy-pnictides, $Na_2Ti_2As_2O$ and $Na_2Ti_2Sb_2O$. The density-wave found in these materials and across the entire ATi_2Pn_2O range of compounds has been the source of much debate. The uncertainty of the type of density-wave, coupled with the superconductivity seen in the $BaTi_2Sb_2O$ and $Ba_{1-x}Na_xTi_2Sb_2O$ and the structural similarities with the cuprates and Fe-based superconductors makes these materials very interesting to the field of superconductivity and layered materials. Prior to the investigations presented here no density-wave superstructure had been observed in these compounds in electron or X-ray diffraction measurements. The X-ray synchrotron diffraction measurements presented here revealed a superstructure in $Na_2Ti_2Sb_2O$ with

wave-vector $\mathbf{q}_{Sb1}$=(0.5,0,0) and $\mathbf{q}_{Sb2}$=(0,0.5,0). Further temperature-dependent X-ray diffraction experiments showed the superstructure in $Na_2Ti_2Sb_2O$ to appear between 110K and 115K in good agreement with the anomalies seen in resistivity, magnetic susceptibility and heat-capacity data from this material. This superstructure along with ARPES and μSR measurements performed by collaborators confirmed the density-wave in $Na_2Ti_2Sb_2O$ to be a charge-density-wave. Temperature-dependent X-ray diffraction measurements on the closely related $Na_2Ti_2As_2O$ compound revealed a similar charge-density-wave superstructure with wave-vectors of $\mathbf{q}_{As1}$=(0.5,0,0.5) and $\mathbf{q}_{As2}$=(0,0.5,0.5). Once again the temperature at which the superstructure appeared was in close agreement with transitions seen in resistivity, magnetic susceptibility and heat capacity from the compound.

The discovery of the charge-density-wave superstructure raises the possibilities of similar structures having been missed in the related compounds such as $Ba_{1-x}Na_xTi_2Sb_2O$ and $BaTi_2Sb_2O$ and the relevance of the CDW to superconductivity in this system needs to be examined. As such a re-examination of $Ba_{1-x}Na_xTi_2Sb_2O$ and $BaTi_2Sb_2O$ using X-ray diffraction would be a worthwhile endeavor. Further work into $Na_2Ti_2As_2O$ and $Na_2Ti_2Sb_2O$ should primarily focus on improving the crystal growth to eliminate the disorder reported in the measurements taken here. X-ray diffraction on higher quality crystals of $Na_2Ti_2Sb_2O$ and $Na_2Ti_2As_2O$ would allow refinement of the crystal superstructure to be performed and a model for the charge-ordering to be deduced. Such a model could be informed or confirmed by soft X-ray resonant diffraction on the superstructure of $Na_2Ti_2Sb_2O$ and $Na_2Ti_2As_2O$. This would allow the charge-distribution in the Ti-O plane to be determined, an experiment which would not have been possible without the knowledge of the superstructure wavevectors presented here.

Pressure has previously been shown to suppress the density-wave seen in $Ba_{1-x}Na_xTi_2Sb_2O$ and promote the superconducting phase in these materials. At ambient pressure the density-wave in $BaTi_2Sb_2O$ appears at 50K where as at hydrostatic pressures of 16kbar this transition is suppressed to ≈40K. Pressure-dependent resistivity measurements on $Na_2Ti_2Sb_2O$ could reveal a similar behavior and promote a hidden superconducting state. The discovery of the charge-density-wave superstructure enables the use of pressure-dependent X-ray diffraction to observe any changes in q_{CDW} as hydrostatic pressure is applied to $Na_2Ti_2Sb_2O$ and $Na_2Ti_2As_2O$.

Further work on $Na_2Ti_2As_2O$ to enable measurement of the associated bandstructure using ARPES would allow for the nesting vector deduced from X-ray diffraction experiments to be related to Fermi-surface features and the density-wave transition in this material to be fully characterized.

6.0.2 $ZrTe_3$

X-ray diffraction and ARPES measurements were used to characterize the effect of Ni-intercaltion on the charge-density-wave phase found in $ZrTe_3$. Several different Ni containing samples were measured using X-ray diffraction and compared to pure $ZrTe_3$. All samples showed the presence of a charge-density-wave superstructure. However no changes to the wavevector of the density-wave superstructure between $ZrTe_3$ and Ni_xZrTe_3 were observed. ARPES measurements of the Fermi-surface of Ni_xZrTe_3 revealed a small shift in the binding energy of the Ni_xZrTe_3 samples when compared to the pure $ZrTe_3$ compound, indicating that the Ni-intercalation had an effect on the quasi-one-dimensional sheet responsible for the charge-density-wave in these materials. ARPES, XPS and the EDX measurements suggested that the Ni-content is far lower than expected from the crystal growth parameters. The finding that the true Ni con-

tent is below the nominal composition will help inform future crystal growth efforts. The ARPES and X-ray diffraction measurements have also highlighted the difficulties associated with measuring these compounds and in a broader context intercalated layered materials in general. I have made several suggestions to reduce the problems arising from inhomogeneities in the crystal which can be used to inform future measurements on these interesting materials. The ARPES measurements taken on the Ni_xZrTe_3 samples provide a detailed account of the Fermi-surface of the material, which can also be used as a reference for future measurements, with changes expected to the binding energy of the quasi-one-dimensional band as a result of the Ni intercalation. Future work on these materials needs to focus on the growth of Ni_xZrTe_3 with higher Ni concentrations. In addition theoretical bandstructure calculations on the effects of chemical pressure on $ZrTe_3$ could be used to complement the observations made using ARPES.Closely related materials such as Cu_xZrTe_3 which have also shown CDW suppression could also be studied using the procedures presented in this thesis.

6.0.3 Uni-axial straining device

In Chapter 5 I presented results on a novel straining device designed specifically for use in X-ray synchrotron experiments. The straining device offers several advantages over other existing methods for applying strain. It allows the application of dynamic uni-axial strain to single crystal samples and is compatible with a number of X-ray synchrotron techniques. It was tested at two synchrotron beamlines using two techniques (IXS and X-ray diffraction). In both of these experiments the device produced significant uni-axial strains in test samples of $M_2Mo_6Se_6$. Based on the measurements presented here and a stiffness analysis of the straining device I have also, in Chapter 5, made a

number of suggestions of ways to improve the straining device and adapt it further to the needs of specific experimental conditions.

The straining device enables a number of interesting experiments to be performed. For example it could be used to dynamically explore pressure-induced phases in a large number of existing crystalline materials using X-ray techniques which are prohibitive to hydrostatic pressure. It offers the ability to perturb crystal anisotropies via uni-axial strain making it an ideal tool for manipulating phases such as DW states and superconductivity. Pressure induced structural transitions can also be accessed, easily measured and manipulated using the device in conjunction with an X-ray diffraction experiment. Future work, now that characterization of the straining device has been performed, should focus on performing the experiments detailed above and exploring using X-ray synchrotron techniques the emergent phases that dynamic uni-axial strain can provide access to.

Bibliography

[1] Frohlich, H. *Proc. R. Soc. London A* **223**(1154), 509–529 (1954).

[2] Kohn, W. *Phys. Rev. Lett.* **2**(9), 393–394 (1959).

[3] Bednorz, J. G. & Müller, K. A. *Phys.* **64**, 289–293 (1986).

[4] Yi, M., Zhang, Y., Liu, Z.-K., Ding, X., Chu, J.-H., Kemper, a. F., Plonka, N., Moritz, B., Hashimoto, M., Mo, S.-K., Hussain, Z., Devereaux, T. P., Fisher, I. R., Wen, H. H., Shen, Z.-X., and Lu, D. H. *Nat. Commun.* **5**, 3711 (2014).

[5] Sipos, B., Kusmartseva, a. F., Akrap, a., Berger, H., Forró, L., and Tutis, E. *Nat. Mater.* **7**(December), 960–965 (2008).

[6] Ang, R., Wang, Z. C., Chen, C. L., Tang, J., Liu, N., Liu, Y., Lu, W. J., Sun, Y. P., Mori, T., and Ikuhara, Y. *Nat. Commun.* **6**, 6091 (2015).

[7] Grüner, G. *Rev. Mod. Phys.* **60**, 1129–1181 (1988).

[8] Monceau, P. *Adv. Phys.* **61**(July), 325–581 (2012).

[9] Rossnagel, K. *J. Phys. Condens. Matter* **23**, 213001 (2011).

[10] Takahashi, S., Sambongi, T., Brill, J., and Roark, W. *Solid State Commun.* **49**, 1031–1034 (1984).

[11] Levy, F. *Physica* **143B**, 174–176 (1986).

[12] Hodeau, J. L., Marezio, M., Roucau, C., Ayroles, R., Meerschaut, a., Rouxel, J., and Monceau, P. *J. Phys. C Solid State Phys.* **11**, 4117–4130 (1978).

[13] Wang, Z. and Monceau, P. *Phys.Rev.B* **40**(17) (1989).

[14] Inagaki, K., Tsubota, M., Higashiyama, K., Ichimura, K., Tanda, S., Yamamoto, K., Hanasaki, N., Ikeda, N., Nogami, Y., Ito, T., and Toyokawa, H. *J. Phys. Soc. Japan* **77**(9), 093708 (2008).

[15] Prodan, a., van Midden, H., Žitko, R., Zupanič, E., Bennett, J., and Böhm, H. *Solid State Commun.* **150**(43-44), 2134–2137 (2010).

[16] Schäfer, J., Rotenberg, E., Kevan, S. D., Blaha, P., Claessen, R., and Thorne, R. E. *Phys. Rev. Lett.* **87**, 196403 (2001).

[17] Yokoya, T., Kiss, T., Chainani, A., Shin, S., and Yamaya, K. *Phys. Rev. B* **71**(14), 4–7 (2005).

[18] Schlenkerc, C., Filippini, C., Marcus, J., Dumas, J., Pouget, J., and Kagoshima, S. *J. Phys. Coll. IV* **44 C3**, 1757 (1983).

[19] Ghedira, M., Chenavas, J., and Marezio, M. *J.Solid State* **57**, 300–313 (1985).

[20] Ando, H., Yokoya, T., Ishizaka, K., Tsuda, S., Kiss, T., Shin, S., Eguchi, T., Nohara, M., and Takagi, H. *J. Phys. Condens. Matter* **17**, 4935–4940 (2005).

[21] Girault, S., Moudden, a. H., and Pouget, J. P. *Phys. Rev. B* **39**(7), 4430–4434 (1989).

[22] Girault, S., Moudden, A., Collin, G., Pouget, J., and Comes, R. *Solid State Comms.* **63**(1), 17–20 (1987).

[23] Gabovich, a. M., Voitenko, a. I., and Ausloos, M. **367**, 583–709 (2002).

[24] Kiss, T., Yokoya, T., Chainani, a., Shin, S., Hanaguri, T., Nohara, M., and Takagi, H. *Nat. Phys.* **3**(October), 720–725 (2007).

[25] Yasuzuka, S., Murata, K., Fujimoto, T., Shimotori, M., and Yamaya, K. *J. Phys. Soc. Japan* **74**(6), 1782–1786 (2005).

[26] Felser, C., Finckh, E. W., Kleinke, H., Tremel, W., and Gutenberg-universita, J. *J. Mater. Chem.* **8**(8), 1787–1798 (1998).

[27] Ritschel, T., Trinckauf, J., Garbarino, G., Hanfland, M., V. Zimmermann, M., Berger, H., Büchner, B., and Geck, J. *Phys. Rev. B - Condens. Matter Mater. Phys.* **87**, 1–5 (2013).

[28] Moodenbaugh, A. R. *Phys. Rev. B* **38**(7), 4596 (1988).

[29] Ravy, S., Laulhé, C., Itié, J.-P., Fertey, P., Corraze, B., Salmon, S., and Cario, L. *Phys. B Condens. Matter* **407**, 1704–1706 (2012).

[30] Röntgen, W. C. *Nature* **53**, 274–276 (1896).

[31] Innes, P. *Proc. A.* **79**(532) (1907).

[32] Nordling, C., Sokolowski, E., and Siegbahn, K. *Phys. Rev.* **105**, 1676–1677 (1957).

[33] Smith, N. V., Traum, M. M., and Disalvo, F. J. *Solid State Commun.* **15**, 211 (1974).

[34] Bragg, W. *Nature* **90**, 410 (1912).

[35] Iwanenko, D. and Pomeranchuk, I. *Phys. Rev.* **65**, 343 (1944).

[36] Elder, F. R., Gurewitsch, a. M., Langmuir, R. V., and Pollock, H. C. *Phys. Rev.* **71**, 829–830 (1947).

[37] Kittel, C. *Introduction to Solid State Physics*. Wiley, New York, 8th edition, (2004).

[38] Simon, S. *The Oxford Solid State Basics*. OUP Oxford, Oxford, (2013).

[39] Dirac, P. *Proc. Royal Society A* **114**, 243–265 (1927).

[40] Hodeau, J. L., Marezio, M., Roucau, C., Ayroles, R., Meerschaut, a., Rouxel, J., and Monceau, P. *J. Phys. C Solid State Phys.* **11**, 4117–4130 (1978).

[41] Zimmermann, M., Schneider, J., Frello, T., Andersen, N., Madsen, J., Käll, M., Poulsen, H., Liang, R., Dosanjh, P., and Hardy, W. *Phys. Rev. B* **68**, 1–13 (2003).

[42] Ashcroft, N Mermin, N. *Solid State Physics*. Orlando: Harcourt, (1976).

[43] Singleton.J. *Band Theory and Electronic Properties of Solids*. Oxford Master Series in Condensed Matter Physics, (2001).

[44] Doiron-Leyraud, N., Proust, C., LeBoeuf, D., Levallois, J., Bonnemaison, J.-B., Liang, R., Bonn, D. a., Hardy, W. N., and Taillefer, L. *Nature* **447**(May), 565–568 (2007).

[45] Pines, D., Kallin, C., Varma, C. M., Flambaum, V. V., Tugushev, V. V., Varma, C. M., Balcar, E., Knight, K. S., Waskowska, A., Brown, P. J., Wanklyn, B. M., Thurston, T. R., Tranquada, J. M., Shirane, G., Chattopadhyay, T., Forsyth, J. B., Nunez, V., Sekio, Y., Nakamura, H., Siegrist, T., and Ramirez, A. P. *Science* **332**, 698–702 (2011).

[46] Liu, D., Zhang, W., Mou, D., He, J., Ou, Y.-B., Wang, Q.-Y., Li, Z., Wang, L., Zhao, L., He, S., Peng, Y., Liu, X., Chen, C., Yu, L., Liu, G., Dong, X., Zhang, J., Chen, C., Xu, Z., Hu, J., Chen, X., Ma, X., Xue, Q., and Zhou, X. *Nat. Commun.* **3**(May), 931 (2012).

[47] Liu, Z. K., Jiang, J., Zhou, B., Wang, Z. J., Zhang, Y., Weng, H. M., Prabhakaran, D., Mo, S.-K., Peng, H., Dudin, P., Kim, T., Hoesch, M., Fang, Z., Dai, X., Shen, Z. X., Feng, D. L., Hussain, Z., and Chen, Y. L. *Nat. Mater.* **13**(May), 677–81 (2014).

[48] Lee, E., Kim, D. H., Denlinger, J. D., Kim, J., Kim, K., Min, B. I., Min, B. H., Kwon, Y. S., and Kang, J.-S. *Phys. Rev. B* **91**, 1–7 (2015).

[49] Damascelli, A. *Phys. Scr.* **T109**, 61 (2004).

[50] Hüfner, S. *Very high resolution photoelectron spectroscopy*, volume xiv. Springer, (2007).

[51] Kevan, S. D. *Angle-resolved photoemission : theory and current applications*. Elsevier, (1992).

[52] Dove, M. T. *Structure and dynamics : an atomic view of materials*. Oxford University Press, (2003).

[53] Baron, A. *arXiv Prepr. arXiv0910.5764* **58**, 205–214 (2009).

[54] Burkel, E. *Reports Prog. Phys.* **63**, 171–232 (2000).

[55] Manuel, C. and Merlin, R. *Light scattering in solids. IX, Novel materials and techniques*. (2007).

[56] Burkel, E., Peisl, J., and Dorner, B. *Europhys. Lett.* **3**, 957–961 (1987).

[57] Hoesch, M., Bosak, A., Chernyshov, D., Berger, H., and Krisch, M. *Phys. Rev. Lett.* **102**(8), 086402 (2009).

[58] Wu, M. K., Ashburn, J. R., Torng, C. J., Hor, P. H., Meng, R. L., Gao, L., Huang, Z. J., Wang, Y. Q., and Chu, C. W. *Phys. Rev. Lett.* **58**(9), 908–910 (1987).

[59] Anderson, P. W. *Science (80-.).* **235**, 1196–1198 (1987).

[60] Monthoux, P., Balatsky, A. V., and Pines, D. *Phys. Rev. Lett.* **67**(24), 3448–3451 (1991).

[61] Norman, M. R., Pines, D., and Kallin, C. *Adv. Phys.* **54**, 715–733 (2005).

[62] Norman, M. R. *Science* **332**(April), 196–200 (2011).

[63] Orenstein, J. *Science (80-.).* **288**(April), 468–474 (2000).

[64] Giannetti, C., Cilento, F., Conte, D., Coslovich, G., Ferrini, G., Liang, R., Eisaki, H., and Damascelli, A. *Nat. Commun.* **2**(January), 353–357 (2011).

[65] Ghiringhelli, G., Tacon, M. L., Minola, M., Mazzoli, C., Brookes, N. B., Luca, G. M. D., Frano, A., Hawthorn, D. G., He, F., Loew, T., Sala, M. M., Peets, D. C., Salluzzo, M., Schierle, E., Sutarto, R., Sawatzky, G. a., Weschke, E., Keimer, B., and Braicovich, L. *Science.* **337**(August), 821–825 (2012).

[66] Chang, J., Blackburn, E., Holmes, A. T., Christensen, N. B., Larsen, J., Mesot, J., Liang, R., Bonn, D. a., Hardy, W. N., Watenphul, A., Zimmermann, M. V., Forgan, E. M., and Hayden, S. M. *Nat. Phys.* **8**(12), 871–876 (2012).

[67] Paglione, J. and Greene, R. L. *Nat. Phys.* **6**(9), 645–658 (2010).

[68] Wang, F. and Lee, D.-H. *Science (80-.).* **2**(April), 200–204 (2011).

[69] Jiang, S., Xing, H., Xuan, G., Wang, C., Ren, Z., Feng, C., Dai, J., Xu, Z., and Cao, G. *J. Phys. Condens. Matter* **21**, 382203 (2009).

[70] Garbauskas, M. F., Arendt, R. H., and Kasper, J. S. *Inorg. Chem.* **26**(5), 3191–3193 (1987).

[71] Pitcher, M. J., Parker, D. R., Adamson, P., Herkelrath, S. J. C., Boothroyd, A. T., Ibberson, R. M., Brunelli, M., and Clarke, S. J. *Chem. Commun. (Camb).* , 5918–5920 (2008).

[72] Yajima, T. *J. Phys. Soc. Jpn.* **81**(2), 1–4 (2012).

[73] Doan, P., Gooch, M., Tang, Z., Lorenz, B., Möller, A., Tapp, J., Chu, P. C. W., and Guloy, A. M. *J. Am. Chem. Soc.* **134**, 16520–16523 (2012).

[74] Lorenz, B., Guloy, A. M., and Chu, P. C. W. *Int. J. Mod. Phys. B* **28**, 1430011 (2014).

[75] Pickett, W. E. *Phys. Rev. B* **58**(8), 4335–4340 (1998).

[76] Liu, R., Tan, D., Song, Y., Li, Q., Yan, Y., Ying, J., Xie, Y., Wang, X., and Chen, X. *Phys. Rev. B* **80**, 1–5 (2009).

[77] Ozawa, T. C., Pantoja, R., Axtell, E. a., Kauzlarich, S. M., Greedan, J. E., Bieringer, M., and Richardson, J. W. *J. Solid State Chem.* **153**, 275–281 (2000).

[78] Shi, Y. G., Wang, H. P., Zhang, X., Wang, W. D., Huang, Y., and Wang, N. L. *Phys. Rev. B - Condens. Matter Mater. Phys.* **88**(October), 1–5 (2013).

[79] Axtell, E. and Ozawa, T. *J. Solid State ...* **134**(134), 423–426 (1997).

[80] Yajima, T. *J. Phys. Soc. Jpn.* **82**, 033705 (2013).

[81] Yajima, T., Nakano, K., and Takeiri, F. *J. Phys. ...* **82**, 1–4 (2013).

[82] Pn, B., As, O. P., Ajima, T. Y., Akano, K. N., Akeiri, F. T., Ozaki, Y. N., Obayashi, Y. K., and Ageyama, H. K. *J. Phys. Soc. Japan* **82**, 3–6 (2013).

[83] Subedi, A. *Phys. Rev. B - Condens. Matter Mater. Phys.* **87**, 1–6 (2013).

[84] Kamusella, S., Doan, P., Goltz, T., Luetkens, H., Sarkar, R., Guloy, A., and Klauss, H.-H. *J. Phys. Conf. Ser.* **551**, 012026 (2014).

[85] Yan, X.-W. and Lu, Z.-Y. *J. Phys. Condens. Matter* **25**, 365501 (2013).

[86] Tan, S. Y., Jiang, J., Ye, Z. R., Niu, X. H., Song, Y., Zhang, C. L., Dai, P. C., Xie, B. P., Lai, X. C., and Feng, D. L. *Sci. Rep.* **5**, 9515 (2015).

[87] Frandsen, B. a., Bozin, E. S., Hu, H., Zhu, Y., Nozaki, Y., Kageyama, H., Uemura, Y. J., Yin, W.-G., and Billinge, S. J. L. *Nat. Commun.* **5**, 7 (2014).

[88] Nozaki, Y., Nakano, K., Yajima, T., Kageyama, H., Frandsen, B., Liu, L., Cheung, S., Goko, T., Uemura, Y. J., Munsie, T. S. J., Medina, T., Luke, G. M., Munevar, J., Nishio-Hamane, D., and Brown, C. M. *Phys. Rev. B* **88**, 214506 (2013).

[89] Kitagawa, S., Ishida, K., Nakano, K., Yajima, T., and Kageyama, H. *Phys. Rev. B - Condens. Matter Mater. Phys.* **87**, 1–5 (2013).

[90] Nowell, H., Barnett, S. a., Christensen, K. E., Teat, S. J., and Allan, D. R. *J. Synchrotron Radiat.* **19**, 435–441 (2012).

[91] Song, Q., Yan, Y. J., Ye, Z. R., Ren, M. Q., Xu, D. F., Tan, S. Y., Niu, X. H., Xie, B. P., Zhang, T., Peng, R., Xu, H. C., Jiang, J., and Feng, D. L. *Phys. Rev. B* **93**, 024508 (2016).

[92] Fujita, M., Goka, H., Yamada, K., and Matsuda, M. *Phys. Rev. Lett.* **88**, 167008 (2002).

[93] Chen, G. F., Li, Z., Wu, D., Li, G., Hu, W. Z., Dong, J., Zheng, P., Luo, J. L., and Wang, N. L. *Phys. Rev. Lett.* **100**, 1–4 (2008).

[94] Machida, K. *J. Phys. Soc. Japan* **50**, 2195–2202 (1981).

[95] Rotter, M., Tegel, M., Johrendt, D., Schellenberg, I., Hermes, W., and Pöttgen, R. *Phys. Rev. B - Condens. Matter Mater. Phys.* **78**, 2–5 (2008).

[96] Castro Neto, A. H. *Phys. Rev. Lett.* **86**, 4382–4385 (2001).

[97] Ru, N., Condron, C. L., Margulis, G. Y., Shin, K. Y., Laverock, J., Dugdale, S. B., Toney, M. F., and Fisher, I. R. *Phys. Rev. B - Condens. Matter Mater. Phys.* **77**, 1–9 (2008).

[98] Kuntscher, C. A., Huber, A., and Hücker, M. *Phys. Rev. B* **89**, 134510 (2014).

[99] Zocco, D. A., Hamlin, J. J., Grube, K., Chu, J., Kuo, H., Fisher, I. R., and Maple, M. B. *Phys. Rev. B* **91**, 1–7 (2015).

[100] Joe, Y. I., Chen, X. M., Ghaemi, P., Finkelstein, K. D., de la Peña, G. a., Gan, Y., Lee, J. C. T., Yuan, S., Geck, J., MacDougall, G. J., Chiang, T. C., Cooper, S. L., Fradkin, E., and Abbamonte, P. *Nat. Phys.* **10**, 421–425 (2014).

[101] Yomo, R., Yamaya, K., Abliz, M., Hedo, M., and Uwatoko, Y. *Phys. Rev. B* **71**(13), 132508 (2005).

[102] Lei, H., Zhu, X., and Petrovic, C. *EPL* **95**(1), 17011 (2011).

[103] Zhu, X., Lei, H., and Petrovic, C. *Phys. Rev. Lett.* **106**, 5–8 (2011).

[104] Hoesch, M., Cui, X., Shimada, K., Battaglia, C., Fujimori, S.-i., and Berger, H. *Phys. Rev. B* **80**(7), 075423 (2009).

[105] Sto, K. and Wagner, F. R. *J. Solid State Chem.* **168**(138), 160–168 (1998).

[106] Chung, M., Wang, Y., Brill, J. W., Burgin, T., and Montgomery, L. K. *Syn.Meth* **57**, 2755–2760 (1993).

[107] Nakajima, H., Nomura, K., and Sambongi, T. *Phys. B+ C* , 240–242 (1986).

[108] Eaglesham, D. J., Steeds, J. W., and Wilson, J. A. *J.Phys. C* **17**, 697–698 (1984).

[109] Feng, Y., Wang, J., Palmer, a., Aguiar, J. a., Mihaila, B., Yan, J.-Q., Littlewood, P. B., and Rosenbaum, T. F. *Nat. Commun.* **5**(May), 4218 January (2014).

[110] Park, T., Ronning, F., Yuan, H. Q., Salamon, M. B., Movshovich, R., Sarrao, J. L., and Thompson, J. D. *Nature* **440**(7080), 65–8 March (2006).

[111] Potel, M. *Phys. Rev. B* **43**(4), 3434–3437 (1991).

[112] Van Der Laan, D. C. and Ekin, J. W. *Appl. Phys. Lett.* **90**(2007) (2007).

[113] Hicks, C. W., Barber, M. E., Edkins, S. D., Brodsky, D. O., and Mackenzie, A. P. *Rev. Sci. Instrum.* **85** (2014).

[114] Marrow, T. J., Liu, D., Barhli, S. M., Saucedo Mora, L., Vertyagina, Y., Collins, D. M., Reinhard, C., Kabra, S., Flewitt, P. E. J., and Smith, D. J. *Carbon N. Y.* **96**, 285–302 (2016).

[115] Collins, D. M., Mostafavi, M., Todd, R. I., Connolley, T., and Wilkinson, a. J. *Acta Mater.* **90**, 46–58 (2015).

[116] PI Actuator Datasheet http://piceramic.com/product-detail-page/p-111-p-151-102900.html Data Accessed:2015-09-01.

[117] Haeni, J. H., Irvin, P., Chang, W., Uecker, R., Reiche, P., and Li, Y. L. **430**(August), 583–586 (2004).

[118] Hicks, C. W., Brodsky, D. O., Yelland, E. a., Gibbs, A. S., Bruin, J. a. N., Barber, M. E., Edkins, S. D., Nishimura, K., Yonezawa, S., Maeno, Y., and Mackenzie, A. P. *Science* **344**(6181), 283–5 April (2014).

[119] Overcash, D., Skove, M., and Stillwell, E. *Physical Review* **187**(1963), 570–574.

[120] Gannon, L., Bosak, a., Burkovsky, R. G., Nisbet, G., Petrovic, A. P., and Hoesch, M. *Rev. Sci. Instrum.* **86** (2015).

[121] Potel, M. and Chevrel, R. *J. Solid ...* **286290**, 286–290 (1980).

[122] Potel, M., Chevrel, R., and Sergent, M. *Solid State Communications, Vol.33,* **33**(254), 607–611 (1980).

[123] Brusetti, R. and Monceau, P. *Solid State Comms* **66**(2), 181–187 (1988).

[124] Lepetit, R., Monceau, P., Potel, M., Gougeon, P., and Sergent, M. *J. Low Temp. Phys.* **56**, 219–235 (1984).

[125] Chew, B. G. M., Golden, J. H., Huggins, B. A., Disalvo, P. J., Zax, D. B., and York, I. **50**(11) (1994).

[126] Tarascon, J. and Disalvo, F J, W. V. *Solid State Comms* , 227–231.

[127] Hor, P. H., Fan, W. C., Chou, L. S., Mengt, R. L., and Chu, C. W. **55**(3), 231–235 (1985).

[128] Ribeiro, F., Roundy, D., and Cohen, M. *Phys. Rev. B* **65**(15), 153401 March (2002).

[129] Çakr, D., Durgun, E., Gülseren, O., and Ciraci, S. *Phys. Rev. B* **74**, 1–8 (2006).

[130] Epotek Epoxy E4110 Data Sheet. www.epotek.com/SSCDocs/datasheets/E4110.PDF. Data Accessed:01-09-2015.

[131] Private communication with Physik Instrumente.

[132] Private communication with A.Petrovic.

[133] Butkovičová, D., Marti, X., Saidl, V., Schmoranzerová-Rozkotová, E., Wadley, P., Holý, V., and Nmec, P. *Rev. Sci. Instrum.* **84**(10), 103902 October (2013).